NTNU – Trondheim
Norwegian University of
Science and Technology

Analysis of the ZnO/Cu2O Thin Film Heterojunction for Intermediate Band Solar Cell Applications

Ellen Caroline Jacobsen

MSc in Physics
Submission date: June 2015
Supervisor: Turid Worren Reenaas, IFY

Norwegian University of Science and Technology
Department of Physics

Preface

This work marks the end of my Master of Science degree in Physics at the Norwegian University of Science and Technology (NTNU), in Trondheim, Norway.

I would like to thank my supervisor Turid Worren Renaas for including me in her research group, helping me complete my thesis and giving me valuable advice and encouragement along the way. I would like to thank Ursula Gibbson for reading my thesis and giving me feedback. I would also like to thank Mohammadreza Nematollahi and Emil Christiansen for making characterization measurements for me. Mohammedreza for doing XPS measurements and analysis, and Emil for doing TEM measurements. Finally I want to thank Stanislav Polyakov for teaching me how to use the PLD lab, and helping me whenever I needed it, Kristin Høydalsvik for being so helpful in the XRD lab, and Espen Rogstad for helping with the AJA sputter and evaporator in NTNU Nanolab.

Abstract

In an attempt to increase the maximum theoretical efficiency of solar cells, one proposed device is called intermediate band solar cells (IBSC). The candidate material system chosen for this study is nitrogen doped cuprous oxide, which is reported to have an intermediate band, in conjunction with zinc oxide, ZnO/N:Cu2O. This thesis has three main parts, a literature study, an experimental material study of Cu_2O and Aluminium doped ZnO (AZO), and finally an attempt at experimentally producing an AZO/N:Cu_2O IB solar cell was made.

The literature study revealed that the largest challenges are the difficulty of producing monocrystalline Cu_2O without CuO or Cu, the high resistivity of Cu_2O, and charge transport and recombination at the AZO/Cu_2O interface. Cu_2O and AZO need to be deposited with as high crystalline quality and low resistivity as possible.

The purpose of the material study was to optimize deposition parameters for thin films produced by pulsed laser deposition (PLD). X-ray diffraction (XRD) and four point probe were the main characterization techniques, but some X-ray photoelectron spectroscopy (XPS) and transmission electron microscopy (TEM) was also performed on select Cu_2O films. The best AZO film produced was deposited at a substrate temperature of 400 °C and a substrate-target distance of 55 mm. It had a resistivity of 3.69 x $10^{-3}\Omega$ cm and its (002) oriented crystallite size of 84 Å.The optimal Cu_2O film was produced with a substrate temperature of 750 °C and was either produced with a flow rate of 3 sccm of O_2 and no N_2, or with 3 sccm of O_2 and 30 sccm of N_2. The film produced with no nitrogen had a larger (111) oriented crystallite size, 336 Å to 313 Å , whilst the film with 30 sccm of N_2 had a lower resistivity 93 Ω cm to 217 Ω cm.

For the purpose of producing an IB material, nitrogen doping of the Cu_2O films was attempted by adjusting the flow ration of N_2/O_2. For the conditions used in this thesis, XPS results indicate negligible nitrogen inclusion.

The last part of the thesis is design and fabrication of a complete solar cell structure, using the optimal parameters from the materials study. The structure proposed was Glass Substrate/Mo electrode/AZO/ZnO/N:Cu2O/Au electrode. In these preliminary tests, the design exhibited ohmic rather than diode characteristics.This was determined to be due to oxygenation of the Mo electrode.

Sammendrag

Formålet med oppgaven var å forsøke å øke den maksimale teoretiske effektiviteten for solceller. En foreslått løsning for å oppnå dette er å benytte mellombåndsolceller (IBSC). Materialet som er valgt for studiet er nitrogen dopet kobberoksid (N:Cu2O), som er rapportert å ha et mellombånd (IB). pn-overgangen som ble undersøkt er dermed aluminium dopet ZnO(AZO)/N:Cu2O. Oppgaven har tre hoveddeler, en litteraturstudie, en eksperimentell materialstudie av Cu_2O og AZO og til slutt et forsøk på å eksperimentelt produsere en AZO/N:Cu_2O IB solcelle.

Fra litteraturstudiet viste det seg at de største utfordringene er å produsere monokrystallinsk Cu_2O uten CuO eller Cu, høy resistivitet i Cu_2O filmer, samt ladningstransport og rekombinasjon over AZO/Cu_2O-grensesnittet. Cu2O og AZO må deponeres med så høy krystallinsk kvalitet og lav motstand som mulig.

Hensikten med materialstudiet var å optimalisere deponeringsbetingelsene for filmer deponert ved hjelp av pulserende laserdeposisjon (PLD). Røntgendiffraksjon (XRD) og fire punkt probe var hovedkarakteriseringsteknikker, men noe røntgenfotoelektronspektroskopi (XPS) og transmisjonselektronmikroskopi (TEM) ble også utført på enkelte Cu_2O filmer. Den beste AZO filmen ble deponert ved en substrattemperatur på 400°C og 55 mm avstand mellom substrat of utgangsmateriale. Denne filmen hadde en resistivitet på 3.69 x 10^{-3} Ω cm og en (002) orientert krystallittstørrelse på 84 Å. Den optimale Cu_2O filmen ble produsert ved en substrattemperatur på 750°C og to ulike strømningsrater. Den ene ble deponert med med 3 sccm av O_2 og uten N_2, den andre med 3 sccm O_2 og 30 sccm N_2. Filmen produsert uten nitrogen hadde en større (111) orientert krystallittstørrelse enn den med 30 sccm av N_2; 336 Å til 313 Å, mens filmen med 30 sccm av N_2 hadde en lavere resistivitet enn den uten N_2; 93 Ω cm til 217 Ω cm.

For å produsere et IB-materiale, ble nitrogendoping av Cu_2O forsøkt ved en høyere strømning av N_2 i forhold til O_2. XPS resultatene viste seg å ikke vere helt konklusive, men resultatene tyder på at det er meget lite eller ikke noe N_2 tilstede i Cu_2O filmene.

Den siste delen av oppgaven handler om design og produksjon av en komplett solcellestruktur. Under fabrikasjonen ble de optimale parameterne fra material studien benyttet. Strukturen foreslått var glass-substrat/Mo elektrode/AZO/ZnO/N:Cu2O/Au elektrode. Ved elektrisk testing fungerte ingen av solcellene. De oppførte seg ohmsk i stedet for som karakteristiske dioder. Dette er sannsynligvis på grunn av oksidasjon av Mo elektroden.

Contents

Preface i
Abstract ii
Sammendrag iii

1 Introduction **2**

2 Clean Energy From Solar Cells **6**
2.1 Early History 6
2.1.1 Market Growth driving research 7
2.2 Limitations in Solar Cell Technology, Efficiency 7
2.2.1 Understanding Efficiency 8
2.2.2 Losses 9
2.3 Near Future, Where are we going 10
2.3.1 Principles of the Simple Solar Cell 10
2.3.2 Tandem Junctions 11
2.3.3 Intermediate Band Solar Cells (IBSC) 11
2.4 IBSC 12
2.4.1 Basic Physical Principles 12
2.4.2 State of the Art IBSC 14
2.4.3 Nitrogen doped Cu2O as an IBSC material 15

3 Literature Review **16**
3.1 Cu_2O as a Solar Cell Material 16
3.2 ZnO as a Solar Cell Material 17
3.3 Notable Cu_2O/ZnO Heterojunctions 17
3.4 Challenges Associated With Cu_2O/ZnO Heterojunctions 20
3.4.1 Recombination of charge across the Junction 21
3.4.2 Material Properties 21
3.5 Overcoming Challenges 23
3.5.1 Minimizing Interface Problems 23

3.5.2 Improving Material Properties . . . 27
3.5.3 Ohmic Electrode Contacts . . . 31

4 Proposed Design **32**
4.1 Cu_2O . . . 33
4.1.1 Optimizing Cu_2O crystal structure . . . 33
4.1.2 Cu_2O as an IBSC material . . . 34
4.2 AZO . . . 35
4.3 Deposition Sequence . . . 36
4.4 Electrodes . . . 36
4.4.1 Bottom electrode, Molybdenum . . . 36
4.4.2 Top electrode, Gold . . . 38
4.5 ZnO, Buffer Layer . . . 39
4.6 Substrate . . . 39

5 Methodology and Experimental Setups **40**
5.1 Pulsed Laser Deposition (PLD) . . . 41
5.1.1 AZO . . . 42
5.1.2 Cu_2O . . . 43
5.1.3 ZnO . . . 44
5.1.4 Solar Cells . . . 45
5.2 Sputtering, Mo . . . 46
5.3 Electron Beam Evaporation, Au . . . 47
5.4 Substrate Preparation . . . 48
5.5 Solar Cell Testing and Thin Film Characterization . . . 48
5.5.1 Profilometer . . . 48
5.5.2 Xray Diffraction (XRD) . . . 48
5.5.3 Four Point Probe . . . 51
5.5.4 Transmission Electron Microscope (TEM) . . . 52
5.5.5 X-ray Photoelectron Spectroscopy . . . 53

6 Experimental Results and Discussion **54**
6.1 AZO thin films . . . 55
6.1.1 XRD Results . . . 55
6.1.2 Resistivity Results . . . 57
6.1.3 Discussion of AZO results . . . 59
6.2 ZnO films . . . 61
6.2.1 Discussion of ZnO Results . . . 62
6.3 Cu_2O Films . . . 63

6.3.1 Cu_2O XRD . . . 63
6.3.2 TEM . . . 73
6.3.3 Resistivity . . . 74
6.3.4 XPS . . . 77
6.3.5 Discussion of Cu_2O films . . . 79
6.4 Solar Cells . . . 81
6.4.1 I-V measurements . . . 81
6.4.2 XPS . . . 83
6.4.3 Discussion Solar Cell . . . 84

7 Conclusion **86**

A Acronyms **89**

B Additional Graphs **91**

C Images **96**

Bibliography **97**

Chapter 1

Introduction

The global population is currently increasing by about 1.1 % per year, and it is estimated that by the year 2050 there will be anywhere between 9 to 11 billion people in the world. [1] This of course leads to an ever increasing need for energy to fuel the modern lifestyle. In 2012 it was estimated that renewable energy accounted for 19 % of the global energy consumption. This of course means that traditional forms of energies, fossil fuels like coal oil and gas, accounted for slightly less than 80 %. [2] The distribution of the different kinds of renewable energies used world wide is shown in Fig. 1.1. It is generally accepted by the scientific community that fossil fuels release harmful gasses such as Cu_2 into the atmosphere that have both long and short term negative effect on the earth and human society, most notably climate change and all that entails. Taking this into account, as well as the undeniable fact that fossil fuels are finite and will eventually run out, it is clear that humans must work to decrease the percentage of energy achieved from fossil fuels and move towards renewable and nuclear options.

While nuclear fission sources currently make up a sizable percentage of the worlds energy consumption it must also be kept in mind that such manufacturing creates dangerous by-products that are radioactive and have very long half-lives, and will thus remain dangerous for generations. In addition to this, unless scientists are to discover how to recreate fusion on earth, nuclear energy is finite and so the potential energy that can be extracted from nuclear sources is limited. This all indicates that the shift in energy production should go towards renewable sources like wind power, hydropower in all its forms, geothermal power, or solar power.

While currently, as seen in Fig. 1.1, the global share of solar energy is quite small, it is also the type of energy with the largest potential. Figure 1.1 is a good visual indica-

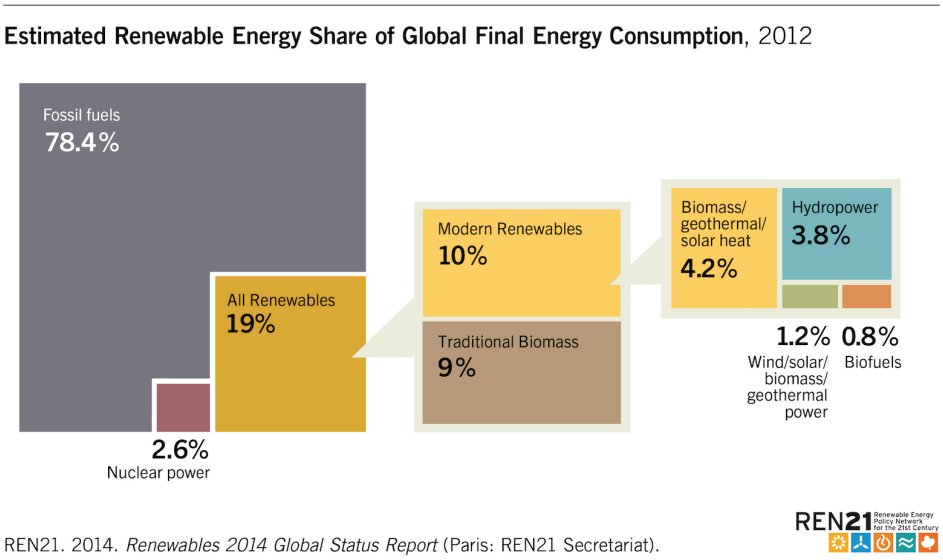

Figure 1.1: The estimated global energy distribution as of 2012. [2]

tion of how much energy could potentially be achieved from individual energy sources comparatively to others. [3] While it is clearly not reasonable to cover every continent from ocean to ocean in solar cells, it is still indicative that the yearly potential of energy coming to the earth via solar radiation, that could be converted to electricity with current technology, far outstrips the entire remaining fossil fuel reserves by many times.

The two commonly used methods for transforming the incoming solar radiation into usable energy are solar cells and solar thermal heaters. The first, solar cells, uses the incoming photons to generate electrons via the photoelectric effect and thus creating electricity. The second method, thermal devices, can do a number of things, focusing solar energy to heat water that can be used for heating houses or for direct use of hot water in showers or cooking. Additionally, thermal devices can be made to use solar energy to heat water to the boiling point and then use the steam to generate electricity through a classic engine.

The most interesting of these two kinds of devices, for commercial purposes, is the solar cell. Solar cells, or photovoltaic (PV) devices have experienced massive market growth in recent years, and since 2010 the world has added more PV capacity than has been in the previous four decades. The cost of manufacturing and installation has decreased whilst the energy extracted per incoming photon, the efficiency, increased. The average efficiency of PV modules increase by a couple of percentage points every year, the most

efficient silicon modules on the market were 19.5 % in 2010. [4]

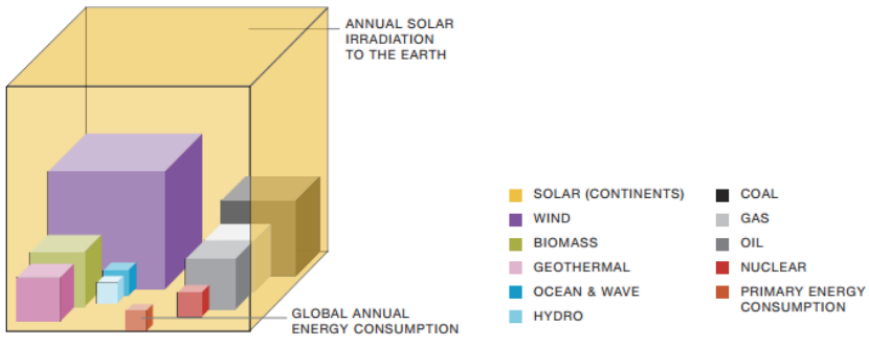

Figure 1.2: EPIA calculated potentials of commonly used energy sources. The fossil fuel calculations are based on remaining reserves, while renewable energies represent their yearly potential. [3]

Motivation

Currently, the vast majority of solar cells on the market are silicon (Si) based. These mass produced Si cells are generally at about 20 % efficiency. The technology involved in producing a Si module has matured to the extent that there is little room for improvement. The majority of the current costs are currently involved in refining the base materials. Thus, to further reduce the cost of the whole PV module, either the materials involved in one cell must be decreased or the efficiency of the cell must be increased.

While many still focus on changing aspects of the Si solar cell, like architecture or crystallinity, many have turned to other materials entirely. Gallium Arsenide (GaAs) is another commonly used material that can produce cells, and it holds the record efficiency for a single junction solar cell with 28.8 %. [5] However, GaAs is both a fairly rare and toxic material, so while it is a popular material for high cost space programs and similar it is not viable for common commercial use.

One material that has always been considered interesting within the field of photovoltaics is cuprous oxide, or Cu_2O, because of its abundancy and non-toxicity. So far, no Cu_2O cells have been made with efficiencies higher than 5 % for a number of reasons that are discussed in this thesis, but the material still shows much promise. Therefore this thesis seeks to investigate methods to increase the efficiency of a Cu_2O cell by finding optimal deposition parameters for all layers in the solar cell.

The purpose of this thesis was to study the materials that could be used in a ZnO/Cu_2O heterojunction solar cell, and it also considers the possibility of creating an IB solar cell by doping the Cu_2O with nitrogen. The end goal was to optimize all layers in the junction and to attempt to use the layers to produce a functioning solar cell. To achieve this, the n-type AZO layer, the undoped ZnO layer and the active p-type Cu_2O layer were deposited using various parameters and then examined individually using XRD to find the parameters that produces optimal crystal structure. In addition the resistivity of the AZO and Cu_2O layers were also tested with a four point probe so that thin films with as high mobilities as possible can be used for the solar cells. To test for successful nitrogen doping, XPS was done on a limited number of the Cu_2O films. In addition to this, lower resistivity may be an indication that the Cu_2O film has been successfully doped with nitrogen.

Chapter 2

Clean Energy From Solar Cells

2.1 Early History

Converting light, or photons, into electrons and electricity is not a new idea. The concept is commonly believed to have been first demonstrated as early as 1839 by a french physicist Edmon Becquerel, by the use of AgCl coated Pt electrodes. However, Becquels observation was more accurately photo-electrochemical. The first practical photovoltaic device was made by Fritts in 1883, and this selenium photocell was described as doing "For the first time, the direct conversion of the energy of light into electrical energy." [6]

115 years later the first silicon (Si) solar cell, or Photovoltaic (PV) cell was demonstrated by Chapin et al. in 1954. Silicone is a naturally n-type material that develops a p-type skin when exposed to boron trichloride, which can then be partially etched away to give access to the n-type layer underneath. [7] This first Si cell only had a power conversion efficiency of 6% which may seem low, but this was six times higher than any previous attempts at creating solar cells had managed. These cells had an estimated production cost of $200 per Watt and were therefore never considered as a legitimate alternative source of energy, but the space and arms race of the cold war certainly ensured that further research went into the intriguing idea of using the sun as a direct source of energy, if only in remote areas or on satellites. [8]

The first commercial applications of the PV device emerged in the 1970s as a direct result of the energy crisis the western world was experiencing due to a drop in the oil markets at the time. [8] Much research was done on the matter of increasing efficiency and reducing production costs. Material science and thin film research became im-

portant and ideas like using polycrystalline or amorphous silicon were first explored. While PV devices did not become commercially common the research done during this period was vital. [7]

It was only in the 1990s that people started to really act on the knowledge that fossil fuels is a polluting and non-renewable resource. Due to the growing awareness that an alternative source of electricity was needed, the interest in photovoltaics also increased once more.

2.1.1 Market Growth driving research

The environmental concerns of the 1990s made people willing to pay higher prices for cleaner types of energy and this opened the market for photovoltaics. This encouraged a growth in research focused on improving the technology, which in turn increased the markets appetite for photovoltaics. This so much so that by the end of the 1990s photovoltaic production increased by 15 % to 20 % each year.

In the period between 2000 and 2012, PV was the fastest globally growing renewable energy source. This is put into context by looking at the numbers, in 2000 the global PV capacity was 1.4GWp, whilst in 2012 this number had moved past 100GWp. [6]

In 2013 the global PV capacity was brought to over 135 GW, and the total new investment in PV capacity was assessed to be worth 96 billion USD. A larger amount of new capacity was installed in Asia than in Europe, for the first time since 2004. China and Japan were the largest driving forces of this development. [4] Whilst future forecasts vary widely, is likely that demand will only grow in places like USA, China and India. This increased demand will in turn create further need for development and research within the field of solar cells in order to create devices with lower cost and higher efficiency.

2.2 Limitations in Solar Cell Technology, Efficiency

All equations and basic knowledge on efficiency presented in this section, unless stated otherwise, were taken from Jenny Nelsons *The Physics of Solar Cells* [7].

The biggest reason why solar cells is not yet the primary source of electricity for mankind is the cost per watt of power extracted. People will avoid investing in new technology when they have a cheaper and easier alternative, despite the evidence that the easier al-

ternative is destroying the planet. To combat this reluctance to invest, researchers have to find ways to increase the efficiency of solar cells.

2.2.1 Understanding Efficiency

The range of bias in which a solar cell can deliver power, from 0 to V_{OC} (the open circuit voltage), is called the operating regime. A cell can also only work within a current range from 0 to I_{SC} (the short circuit current). The power density that can be produced by a solar cell within these ranges are described by equation 2.1.

$$P = IV \tag{2.1}$$

Where P is the power output, I is the current and V is the voltage. The maximum power a cell can deliver therefore occurs at some voltage V_m and current I_m, where V_m is less than V_{OC} and I_m is less than I_{SC}. [7] Graphing the current and voltage that a solar cell can produce under illumination will appear characteristically as a square curve as can be seen in Fig. 2.1. The maximum power that the cell can produce will occur at the turning point of the red IV curve, as is demonstrated by the blue power curve.

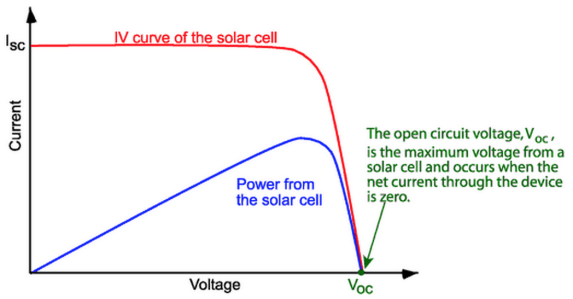

Figure 2.1: Basic characteristic I-V and P-V curves for a solar cell. [9]

The better a cell is, that is the more power it can produce, the more 'square' the IV curve will be. The 'squareness' of the IV curve can be described by its fill factor, which is represented by equation 2.2:

$$FF = \frac{I_m V_m}{I_{SC} V_{OC}}. \tag{2.2}$$

The efficiency η of a cell is the power density delivered at a operating point with voltage V_m and current I_m, with respect to P_S the incoming power density. This is described by

equation 2.3:

$$\eta = \frac{V_m I_m}{P_S}. \tag{2.3}$$

The efficiency can be related to the short circuit current and the open circuit voltage through the fill factor by equation 2.4

$$\eta = \frac{I_{SC} V_{OC} FF}{P_S}. \tag{2.4}$$

2.2.2 Losses

Simply put, the efficiency is a measure of how much electricity can be extracted from a solar cell, and clearly, it would be desirable for a solar cell to have a high efficiency in order to be cost effective. The Shockley Queisser (SQ) detailed balance estimates that the maximum conversion efficiency of a simple one junction device with an energy gap of 1.1 eV, like the commonly used Si, is 30%. The maximum efficiency for any single junction device will be for a material with a band gap of about 1.4 eV, and it is 33%. This value assumes that the sun and the cell are blackbodies at 6000 °K and 300 °K respectively, under AM 1.5 solar radiation, that all photons with energy greater than then bandgap are absorbed, that all recombination is radiative and that the carrier mobility is infinite. [10] At the highest level of concentration of the illumination, the maximum theoretical efficiency of a single junction is 40.7%. [11] The Shockley Queisser detailed balance clearly refers to an idealized cell which would be impossible reproduce in a lab, real efficiencies would be somewhat lower than this.[12]

A number of things will cause real efficiencies to be lower than this maximum 33 % value. Un-absorbed photons and non-radiative recombination are two of the largest causes of this, and any semiconductor material with a bandgap smaller or larger than the ideal 1.4 eV will also have smaller maximum theoretical efficiency. Additionally there are two types of electric resistance that reduce efficiency in a PV device. These resistances are called are parasitic resistance in series (R_s), and shunt resistance (R_{sh}). To produce a cell that is as efficient as possible the series resistance would ideally be as small as possible and the parallel resistances would ideally would be infinitely large. The small series resistance allows current to flow through the device and the large shunt resistance prevents current from flowing around the edges of the device. The series resistances come from resistances of the cell material to the current flow, for examples at the junctions between the p-type and n-type materials and at the connection with the pn-materials and their contacts. The shunt resistances arise from leakages in the device, the lower the shunt resistance is the more the device allows current to flow around

the edges between the contacts, avoiding the pn-junction entirely. [7]

Increase in the series resistance and decrease in the parallel resistance reduce the fill factor in a PV device, which in turn reduces the efficiency. [7] Clearly some loss in efficiency is inevitable during manufacturing, so to combat this the maximum theoretical efficiency of a cell can be increased by deviating from the standard one junction design.

2.3 Near Future, Where are we going

Silicon has dominated the field of photovoltaics since the first 6% device was made in 1954. This is primarily because it is a cheap, readily available material which we have a very good grasp of technologically. However, we have also reached a the edge of the conversion efficiency that is possible for the Si single junction device. In order to make solar energy truly capable of competing against the cheap and easy energy extracted from oil, coal and natural gas, we need to figure out how to produce higher efficiencies per unit area and per cost out of the solar cells marketed commercially.

2.3.1 Principles of the Simple Solar Cell

The basic principle behind a solar cell, or a photovoltaic device, is to convert photons into mobile charge by absorption. An incoming photon with energy equal to or greater than that of the bandgap of the solar cell material will be absorbed by an electron and give it energy to move from the valance band to the conduction band, creating a mobile electron in the conduction band and a mobile hole in the valance band. This mobile charge can then be separated and transported by the pn-junction into an external circuit by the asymmetry resistance in the junction. In a closed circuit, illuminating the solar cell will generate a photocurrent, I_{SC} and in an open circuit the illumination will generate a photo voltage, V_{OC}. If a load resistance is attached to the external circuit, current and voltage capable of doing electrical work will be observed. [7]

The short circuit current generated by the cell depends on the quantum efficiency of the cell, that is, the probability of it generating an electron per incident photon as a function of the photon energy. Thus the spectrum and intensity of the incident light mainly decides how much current will be generated by a cell. [7]

The load introduced in the circuit produces a potential difference that drives a current, called dark current, in the opposite direction to the photocurrent. When the load resis-

tance is increased to the point where it creates a dark current equal to the photocurrent the optimal operating point of the cell has been reached as this is where the maximum power can be extracted. In an ideal cell, the potential difference at this point is the open circuit voltage, V_{OC}, and the current produced is the short circuit current I_{SC}.[7]

2.3.2 Tandem Junctions

The idea behind a tandem junction is to maximize the amount of the solar spectrum absorbed by stacking multiple junctions with different bandgaps in series. A two junction cell has a theoretical maximum efficiency of 44%, a three junction cell has 54% maximum efficiency, and if you stack an infinite number of tandem junctions the theoretical maximum efficiency is 66%. [8] Under concentrated light these values are 40% for one junction, 55 % for two junctions, 63 % for three junctions and 86 % for an infinite number of junctions.[11]

Multi junction devices have a higher maximum theoretical efficiency because the different junctions can absorb a larger range of photons, increasing the probability that an incident photon will excite an electron and produce electricity. This will increase the I_{SC} and the V_{OC}, increase the maximum power density, and in turn increase the efficiency.[8] Multi junction devices have been demonstrated in a laboratory, and the record efficiency reached is 46 % with a four junction concentrator cell or 38.8% with a four junction non-concentrator cell. [5]

The problem with tandem junction solar cells is that often they are very expensive per unit area of solar cell to produce. This is mainly due to substrate costs and because layers have to be grown at low deposition rates to minimize defects. Minimizing defects is especially important with multiple junctions because the number of layers mean that small defects in and between each layer can add up to a large series resistance, which will decrease the efficiency and mitigate the purpose of using multiple junctions.[8]

2.3.3 Intermediate Band Solar Cells (IBSC)

The idea of using electronic states within the band gap of a solar cell as a method for increasing the efficiency was first postulated by Martin Wolf in 1960. It was Wolfs idea that by placing these impurities in the band gap of the bulk material the cell as a whole would be capable of absorbing a wider range of photon energies, thereby decreasing loss by transmission and increasing the efficiency of the cell.[8] In 1997 Luque and Marti came up with a detailed theory of how such an impurity-laced device would work, and

calculated that intermediate band solar cells (IBSCs) could potentially operate at efficiencies as high as 47% under one sun and the same ideal conditions used in the detailed balance calculations of Shockley and Qiesser. If the illumination is concentrated the theoretical limit is 63.2 % [13] However experimentally this 63 % efficiency is still a far off goal. No full IBSC has been demonstrated, but the key operating mechanism of photocurrent due to transition of carriers from the intermediate band to the conduction band was shown by Marti et al in 2006, even if it was at a low rate. [14]

The obvious downside to such impurity states is that they could increase the amount of nonradiative recombination within the cell. [8] The difference between the impurity cell that Wolfe proposed in 1960 and the IB cell that Luque proposed in 1997 was that theoretically the IB should reduce non radiative recombination. However, it remains one of the principle challenges with this kind of device to insert an IB that supports strong optical transitions and low non-radiative transitions in comparison to the rate of photogenerated electrons[12]

2.4 IBSC

In the previous section, Subsection 2.3.3, it has been explained how the idea of IBSC as a possible concept that could increase the maximum theoretical efficiency of solar cells came into being. In this section this concept is described in more detail, including the physical principles behind the idea and the current state of the technology.

2.4.1 Basic Physical Principles

The basic principle of the Intermediate Band Solar Cell is to introduce an impurity into the semiconductor that is able to absorb additional photons, with lower energies, that the original semiconductor bandgap. Commonly when an impurity is found in a semiconductor it works as a non-radiative recombination center, causing losses rather than gains. The IB impurity creates an additional energy level in what would otherwise have been the forbidden bandgap, as seen in Figure 2.2, and if the IB material works as a radiative recombination center, the semiconductor should be able to absorb photons with energies equal to and greater than G_{IV} and G_{IC} in addition to the usual G_{VC}[15]

The power generated in a conventional solar cell are a trade off between voltage and current. A cell with a small bandgap will be able to produce low current but high voltage, while a large bandgap will produce high current but low voltage. This is shown by the current density-voltage graphs shown in fig 2.3.

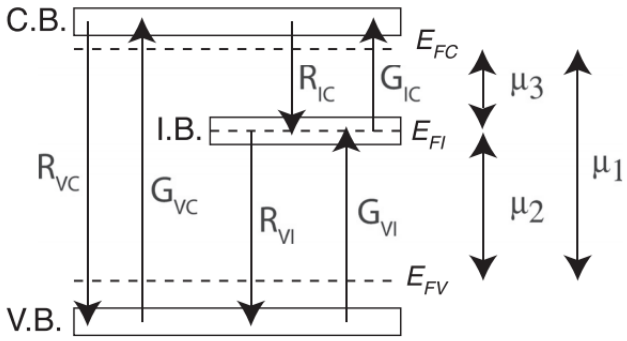

Figure 2.2: The energy levels and basic transitions in an IBSC made by Okada et al. $R_{VC,IC,VI}$ represent recombination between bands, $G_{VC,IC,VI}$ show generation, $E_{FV,FI,FC}$ are the quasi fermi levels of each energy band and $\mu_{1,2,3}$ are the electrochemical potentials between each fermi level.[12]

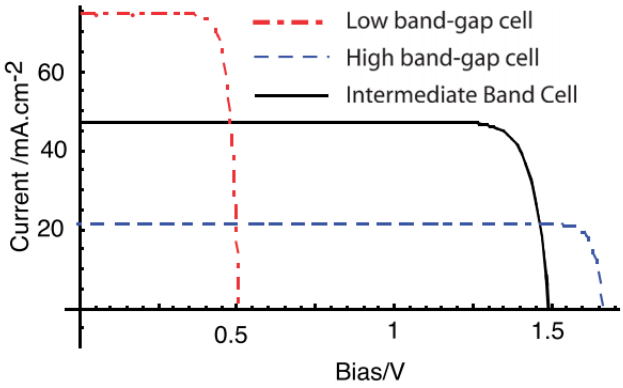

Figure 2.3: J-V curves for two SQ cells, one corresponding to the smallest bandgap found in an IBSC one corresponding to the largest band gap, the solid curve is that of an IBSC with the same absorption thresholds. [12]

The IBSC absorption curve shown in Fig 2.3 is able to maintain the broad absorption profile of the low band gap SQ cell, since the IB impurities can absorb the smaller energy photons that the main material cannot. However, the current density of the IBSC is still approximately half that of the low band gap SQ cell because the additional photocurrent created from the IB needs two photons for every electron hole pair emitted into the circuit, one to move an electron to the IB and the second to move it up to the

CB. [12][14]

The voltage produced by the IBSC can be larger than that of a SQ cell with an equivalent absorption spectrum because the open circuit voltage will still correspond to that of the large bandgap material used. The charge extraction only occurs from the CB and the VB, not directly from the IB. This is shown in fig 2.2, there are three electrochemical potentials, $\mu_{1,2,3}$ where $\mu_1 = \mu_2 + \mu_3$. However, the total potential will still be given by μ_1. There potential will still, however, be slightly lower than that of an SQ cell with the same CB-VB bandgap because of inevitable non-radiative recombination via the IB, shown by paths R_{IC} and R_{VI}, in addition to the recombination through R_{VC} in figure 2.2. [12]

2.4.2 State of the Art IBSC

IBSC could be an alternative to classic one junction devices, but currently the state of the development of such devices is not yet ready commercial application. However, the technology is moving in the right direction. In 2010 Luque et al. [16] wrote a paper describing the advantages and remaining challenges of practically producing IBSC, and concludes that overall there is plenty of hope that these devices can be made. In 2011 Luque and Marti [17] took an in depth look at IBSC that had been produced, and noted relevant advances that have been made within this research field. They found that recent results are taking large strides towards realizing a high efficiency IBSC.

There are currently two main directions that the research towards IBSC is taking. Some people are looking into producing quantum dots (QDs) inside the active material. Here the IB is formed by confined states made by the QDs inside the main bandgap of the active material. The main problem with this approach is that there is often a strong thermal connection between the IB and the CB and this makes it difficult to split the quasi fermi levels of the IB and CB at room temperature, using only solar energy. To split this thermal connection and demonstrate open circuit voltages limited by the CB-VB bandgap of the host material, low temperatures are required. [17] [18]

The other research direction, which is what is considered in this thesis, tries to produce IB by developing alloys and doping that naturally exhibits the IB. Walukiewicz et al. [19] were the first group to produce a functioning alloy based IBSC. They used photo reflectance spectroscopy to show that an IB had been created in the bandgap of highly mismatched semiconductor materials like $ZN_{1-y}Mn_yO_xTe_{1-x}$ and $GaN_xAs_{1-x-y}P_y$. The first Bulk IBSC were ZnTe doped with oxygen to form the IB, made by Wang et al. [20]. An increased current and efficiency was observed from the IB cell, compared to the ref-

erence cell. However, the IB cells also had a lower output voltage. The IB cells clearly demonstrated absorption of photons with energies lower than the ZnTe bandgap, making it clear that such devices do indeed have promise.

In 2011 López et al. [21] overcame the low output voltage that Wang et al. [20] observed, by introducing a blocking layer that prevents electrons from tunneling from the IB and the substrate CB. The cell they made consisted of $GaN_{0.024}As_{1-0.024}$, where 0.024 was the nitrogen concentration that produced the desired bandgaps. Introducing the blocking layer produced a cell with an open circuit voltage of 0.92 V at room temperature and 20 suns illumination, which was much higher than the 0.42 V produced by the reference cell. Additionally, López et al. observed for the first time an electroluminescence peak at 0.9 V, demonstrating that radiative recombination was taking place between a partially filled IB and the CB. This proves that there thus must be quasi fermi level splitting between the CB and the IB in this cell, and as such this research is a highly important step towards realizing a high efficiency IBSC.

2.4.3 Nitrogen doped Cu2O as an IBSC material

The theoretical efficiency limit of 63.2 % under maximum solar light can be reached with an absorber material that has E_g = 1.9 eV and an IB at 0.7 eV from the VBM or from the CBM. [13]. The maximum theoretical efficiency has been shown to drop to 49% under AM1.5G, using materials with bandgaps of either 2.1 eV with the IB at 0.7 from the VBM (or CBM)[22] or 2.5 eV with the IB at 0.9 eV from the VBM (or CBM) [23]. Thanks to its energy gap of 2.1 eV, Cu_2O could be a very good material for this type of device.
Nitrogen is a good dopant that could be used to make an IB material from Cu_2O. It should be simple to dope the Cu_2O with nitrogen in large consternations, [23] and it has been shown to be a good p-type dopant [24]. The acceptor level of nitrogen doping in Cu_2O has been estimated to be 0.14 eV from the VB. [25]

Malerba et al. [26] wrote a paper in 2012 investigating the possibility of using nitrogen doped Cu_2O as an IB material. Cu_2O films were doped with nitrogen from 1 at% to 2.5 at%, and were then tested for absorption and resistivity. It was found that the films with the highest levels of nitrogen doping were more conductive and more absorbent than the undoped films. Additionally The increased absorption took place at two below bandgap energy levels, 0.45 eV and 0.72 eV, and the absorption bands appeared to correlate with the level of nitrogen doping. This suggests that N:Cu_2O is a very promising material for IBSC, and as such will be considered in this thesis.

Chapter 3

Literature Review

In the experimental part of this thesis, the active material that will be used for the IB host is p-type Cu_2O, and the n-type material in the junction will be Al:ZnO (AZO). In order to design such a solar cell an extensive literary review was conducted to find the main advantages and challenges with this heterojunction.

The material properties of Cu_2O and ZnO are discussed in sections 3.1 and 3.2. The methods used previously to make ZnO/Cu_2O junctions are discussed in section 3.3, the challenges that have been discovered thus far are discussed in section 3.4, and finally possible solutions are discussed in Section 3.5.

Both ZnO and Cu_2O are relatively underdeveloped for solar cells in comparison to materials like silicon or GaAs, who are the most commonly used in commercial solar cells. The junction has been tried a number of times, and Cu_2O was one of the earliest materials that were considered for solar cell use. [8] However, as of yet interface problems have limited efficiencies. It is therefore reasonable that further research into the relevant materials in this thesis will present solutions that can be able to overcome the challenges presented in the literature.

3.1 Cu_2O as a Solar Cell Material

Copper(I) Oxide, or Cu_2O, has long been considered an interesting material for solar cell use. This is a large part because it is both non-toxic and abundant. In addition it has a relatively high mobility at room temperature, and as long as it is close to a single crystal it has pretty decent minority carrier diffusion length. [27] Cu_2O is intrinsically

p-type due to Cu vacancies in the lattice and it has a direct band gap of 2.07 eV. [28] All of this means that the calculated theoretical conversion efficiency (Shockley-Queisser efficiency limit) of 20%, which is reasonably high and means that Cu_2O is a material that should be further studied for solar cell use. [29]

However there have been no Cu_2O solar cells made so far that lives up to the promise of the theoretical data. This largely because manufacturing can be tricky as a result of the presence of CuO which can occur. This causes problems like Schottky junctions and lattice defects that degrade mobility and conductivity as well as causes non radiative recombination. [30] In addition to this, the Cu_2O films made so far often demonstrate a low collection probability of photoexcited carriers and high surface recombination. [29] This means that despite the promising theoretical efficiency, Cu_2O has so far been a disappointing solar cell material experimentally.

3.2 ZnO as a Solar Cell Material

ZnO is a good electron acceptor with a hexagonal crystal structure, and is useful as an n-type semiconductor in inorganic thin film solar cells. It is common in such thin films to dope ZnO with aluminum at the Zn sites, creating AZO, as this improves carrier transport properties. [31] Zinc oxide, and its aluminum doped variant is a commonly used in conjunction with the p-type Cu_2O. It is intrinsically n-type, due to oxygen vacancies, and it has a large band gap of 3.3 eV which means it transmits smaller wavelengths to the active Cu_2O material. The aluminum doping significantly increases the conductivity, the charge carrier density and the mobility, making it ideal for solar cell use. [32]

3.3 Notable Cu_2O/ZnO Heterojunctions

A number of people have previously made Cu_2O/ZnO heterojunctions, and a summary of notable attempts and the achieved conversion efficiencies are listed in Table 3.1 from highest to lower efficiencies.

Using thermally oxidized copper sheets made in a furnace under controlled atmospheric conditions as both the substrate and the active layer is a simple way to limit the amount of CuO and Cu in the junction. A number of ZnO/Cu_2O junctions made on such oxidized copper sheets, and these attempts were summarized by Minami et al. in a 2011 review paper [33]. This paper discusses a number of junctions, but the most efficient cell produced was an AZO/ZnO/Cu_2O junction where the AZO and ZnO were deposited

by pulsating laser deposition (PLD). This cell had an efficiency of 3.83 % and an open circuit voltage of 0.69 V.

More recently, in 2012, Minami et al. [34] made a similar junction where they used PLD to first deposit a buffer layer of $Zn_{0.91}Mg_{0.09}O$ and then the n-type AZO layer on a thermally oxidized copper sheet. The conversion efficiency this time was much higher, 4.3 %, and the open circuit voltage reached was 0.8 V.

Possibly the best ZnO/Cu_2O junction to date was made by Minami et al. in 2013 [35]. This time PLD was again used to first deposit Ga_2O_3 buffer layer and second a n-type AZO layer on the thermally oxidized copper sheets. The conversion efficiency reached was as high as 5.38 % and the cell had an open circuit voltage of 0.8 V.

The highest efficiency cell that has been constructed without resorting to using thermally oxidized copper sheets was made by Lee et al. in 2014. [36]. The Cu_2O layer was produced on a gold electrode by galvanostatic electrochemical deposition at 40 °C, before atomic layer deposition (ALD) was then used to deposit a Ga_2O_3 buffer layer, like the highest efficiency cell made by Minami et al. [35] and finally an AZO layer. This cell had a fairly promising efficiency of 3.97% and an open circuit voltage of 1.2 V.

Hussain et al. [37] used in 2011 radio frequency sputtering to deposit first ZnO then used electrodeposition to produce the Cu_2O. This was a notable attempt because the paper studied varying deposition potentials for the Cu_2O layer in order to maximize the (111) orientation in the Cu_2O lattice and minimize defects. they also found that pre-annealing the ZnO film before Cu_2O deposition resulted in larger particle size, increased electron mobility and higher conductance, and this almost doubled the effectivity of the cells produced. The highest efficiency cell produced was at 0.24% and it had an open circuit voltage of 0.34 V.

Katayama et al. [38] found in 2004 that making the heterojunction at low temperatures avoids the thermal reaction that creates a copper rich area at the junction and forms a Schottky barrier. For this reason they used a two step electrodeposition method do deposit the layers because electrodeposition can be done at low temperatures. The cells produced had a conversion efficiency of 0.117 %, an open circuit voltage 0.19 V and a short circuit current of 2.08 mA cm^{-2} .

In 2006 Minami et al. [39] made a study on the effects of the various deposition methods have on the ZnO/Cu_2O junction efficiency. dc magnetron sputtering (dc-MSP),

PLD, and vapor arc plasma evaporation (VAPE) were explored as possible deposition methods. The highest efficiencies were reached by VAPE and PLD respectively, with efficiencies of 1.52% and 1.42% under AM 2 solar radiation and 200 °C.

Multiple attempts have been made at making a junction that does not require a vacuum during deposition. This is in order to make the process cheaper and more commercially viable. Fujimoto et al. [40] used in 2013 electrodeposition (ECD) to deposit a FTO/ZnO/Cu2O/Au heterojunction from pH-adjusted electrolytes consisting of LiOH, NaOH or KOH. The best junction produced by Fujimoto et al. was one made using LiOH, it had a conversion efficiency of 1.43 % and an open circuit voltage of 0.54 V.

Levskaya et al. [41] used atmospheric atomic layer deposition (AALD) to produce a simple ZnO/Cu_2O junction with a conversion efficiency of 1.46 % and a V_{OC} of 0.49 and another junction with a $Zn_{0.79}Mg_{0.21}O$ that managed a conversion efficiency of 2.2 % and a V_{OC} of 0.65 V. More junctions made under atmospheric conditions can be seen in Table 3.1, and while it is clear that these cannot compete with the best junctions produced in vacuums, the atmospheric junctions are clearly achievable.

Table 3.1 clearly shows that the junctions that perform the best are made of a combination of thermally oxidized sheets, buffer layers and AZO deposited in a vacuum.

Table 3.1: Cu2O-based solar cell efficiency latest developments (to 2014). The table is based on one made by Levskaya et al [41]

Type of junction	PCE %	Voc	Deposition Method	ref
Cu2O-based junctions formed in vacuum				
AZO/Ga_2O_3/Cu_2O	5.38	0.8	PLD on Cu_2O sheet	[35]
AZO/$Zn_{0.91}Mg_{0.09}O$/Cu_2O	4.3	0.8	PLD on Cu_2O sheet	[34]
AZO/ZnO/Cu_2O	4.12	0.72	PLD on Cu_2O sheet	[42]
AZO/Ga_2O_3/Cu_2O	3.97	1.2	ALD	[36]
AZO/ZnO/Cu_2O	3.83	0.69	PLD on Cu_2O sheet	[33]
AZO/a-ZTO/Cu_2O	2.85	0.62	ALD	[43]
AZO/a-ZTO/Cu_2O	2.65	0.55	ALD	[44]
AZO/Cu_2O	2.53	0.55	PLD on Cu_2O sheet	[35]
ITO/ZnO/Cu_2O	2.01	0.6	IBS	[30]
ZnO:Ga/Cu_2O	1.52	0.41	VAPE	[39]
AZO/Cu_2O	1.39	0.4	dc-MSP	[39]
AZO/Cu_2O	1.21	0.41	PLD	[45]
AZO/Cu_2O	0.24	0.34	electrodeposition	[37]
Cu2O-based junctions formed without vacuum				
ZnO/Cu_2O	0.12	0.19	ECD	[38]
ZnO/Cu_2O	1.43	0.54	ECD	[40]
ZnO/Cu_2O	1.28	0.59	ECD	[46]
ZnO/Cu_2O/Cu_2O+	0.9	0.32	ECD	[47]
ZnO/Cu_2O	0.47	0.28	ECD	[48]
ZnO/Cu_2O	0.41	0.32	ECD	[49]
ZnO/Cu_2O	1.46	0.49	AALD	[41]
ITO/$Zn_{0.79}Mg_{0.21}O$/Cu2O	2.2	0.65	AALD	[41]

3.4 Challenges Associated With Cu_2O/ZnO Heterojunctions

It is an indicative of the challenges with the ZnO/Cu_2O junction that the highest conversion efficiency reached is 5.38% in 2013 by Minami et al. [35] when the Shockley-Queisser efficiency limit of Cu_2O and ZnO are 20% and 18% respectively. Generally the conversion efficiencies of junctions do not even reach near the 5.38% value, hovering between 1% and 4%. [41] This indicates that further research into identifying and overcoming the problems that arise under design or manufacturing could allow the Cu_2O/ZnO heterojunction to become more efficient than what has currently been achieved.

One of the largest drains on effectivity of ZnO/Cu_2O based cells that has been identified is the interfacial defects that appear. [50] High defect densities at the junction will lower the built in potential of a pn-junction, and thus decrease its photovoltaic properties. [51] Abu and Musa noted that a ZnO/Cu_2O junction can often become a ZnO/Cu/Cu_2O

Schottky junction since the Zn has a tendency to reduce the Cu_2O to Cu. [52] Achieving good junction quality and low defect density is therefore a large challenge, so the deposition method and parameters, as well as possible surface treatments for the Cu_2O have to be looked into. Poor charge transport across the junction can also be an issue, so iincreasing the quality of the lattice matching is also a considerable challenge that needs to be addressed. [53]

3.4.1 Recombination of charge across the Junction

Creating a high quality junction means limiting non-radiative recombination across the junction. Jeong et al. wrote a paper on temperature dependent J-V characteristics of ZnO/Cu_2O junctions and concluded that the three biggest causes of recombination were interfacial recombination, tunneling of holes to recombine with the same interfacial states, and tunneling of electrons into interfacial states to recombine. These three recombination paths are shown in Fig. 3.1. Of these three, the interfacial recombination was the largest and the rate limiting factor at all temperature ranges.

As can be seen in Figure 3.1, the activation energy for recombination is roughly 1.1 eV. This value has been calculated by Jeong et al. using literature values, but they also made experimental measurements and found that E_a = 0.99 eV - 1.34 eV. [54] This is less than the 2.2 eV bandgap of Cu_2O, indicating that there are interfacial states at the junction allowing charge transport across the junction and causing recombination.

Interfacial recombination occurs when holes in the VB are able to diffuse into interfacial states in the bandgap to recombine with electrons trapped there. This is shown as Path 2 in figure 3.1. The second largest source of recombination is shown by Path 1 in figure 3.1 and it occurs mostly at high temperatures, when holes are able to tunnel through the junction due to band bending, and recombining with the electrons in the interfacial states. This type of recombination can be limited by introducing a buffer layer at the junction and is therefore not. Finally Path 3 in figure 3.1 describes electrons tunneling from the ZnO conduction band to interfacial trap states.

3.4.2 Material Properties

The crystallinity and quality of the component Cu_2O and ZnO, as with most other pn-junctions, has a very large effect on the performance of the heterojunction. [51] Ideally both materials would be produced as single crystals, and this is particularly important

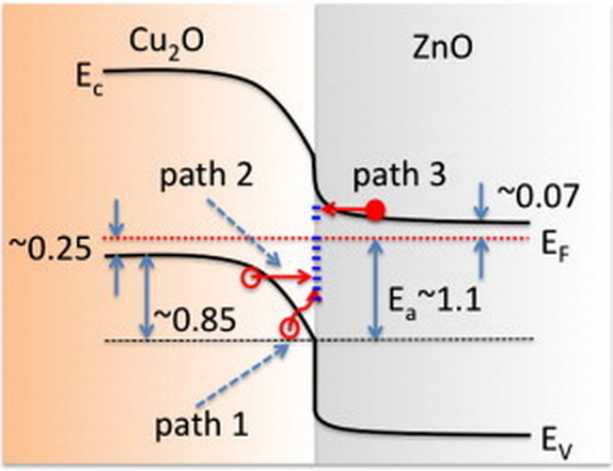

Figure 3.1: Band diagram of a Cu_2O/ZnO heterojunction with E_V is the energy of the VB, E_C is the energy of the CB, E_F is the energy of the fermi level, and E_a is the activation energy. Path 1, Path 2 and Path 3 are the three paths that charges can recombine. [54]

for the active material Cu_2O. For this purpose, deposition methods and parameters that increase crystallite size in one particular orientation should be considered.

Cu_2O

A very large challenge that need to be considered is the crystalline quality of the Cu_2O thin films. It has been found by Hussain et al. [37] that particle size, crystalline faces and the level of crystallinity in Cu_2O determines the quality of the pn-junction interface. The energy levels, densities, and distribution of interface states are highly affected by the exposed crystal face of the Cu_2O material at the junction. Fewer interface states means smaller amounts loss to recombination, and as will be shown in Section 3.5.1 it is desirable to produce the (111) orientation to decrease lattice mismatch which can lead to junction defects.

Mittiga et al. [30] argues, the high resistivity of the Cu_2O is the limiting factor of efficiency in ZnO/Cu_2O junctions. Therefore one of the challenges that need to be considered is how to produce Cu_2O thin films with lower resistivity. Li et al. [55] investigates how buffer layers and growth conditions increase mobility, and also discussed the connection between crystalline quality and conductivity.

ZnO

ZnO has a larger bandgap than Cu_2O, ZnO has a band gap of roughly 3.3 eV and Cu_2O has a band gap of roughly 2.1 eV. This means that in a solar cell the ZnO should be the first layer exposed to the light, so that shorter wavelengths can be transmitted through to the Cu_2O layer with the smaller bandgap. Katayama et al. [38] observes that ZnO has a low transmittance at certain wavelengths of light, so the ZnO layer has to be deposited for optimal transmittance.

As with Cu_2O, increasing the crystallinity of the ZnO layer will decrease the defects at the interface. Hussain et al. [37] found that pre-annealing the ZnO film resulted in larger particle size, increased electron mobility and made the films more conductive, and this almost doubled the effectivity of the ZnO/Cu_2O cells produced. This is evidence that making sure to maximize all material properties of the ZnO layer is vital.

ZnO is a transparent conductive oxide (TCO), and as such it is a widely used and highly researched. For this reason ZnO and its aluminum doped counterpart is a fairly simple material to deal with. It is easy to deposit, has a low resistivity and high mobility. Generally, any ZnO deposited should be created to maximize crystallinity and conductivity.

3.5 Overcoming Challenges

Solving the challenges that have been observed producing ZnO/Cu_2O junctions is vital. This means finding ways to eliminate lattice mismatch defects that act as recombination centers, increasing the transmissivity of the ZnO layer, increasing the crystal quality and reducing the resistivity in the Cu_2O layer. It has not yet been considered a priority to increase the transmission of ZnO, but it is acknowledged as a potential issue. Using thinner ZnO films will increase the transmissivity in a simple way, so limiting the thickness of this layer is a simple way to decrease the limiting ability of this challenge, assuming the conductivity remains suitably high.

3.5.1 Minimizing Interface Problems

Minimizing the defects and charge transport issues at the interface of the pn-junction is a vital part of increasing the efficiency of the ZnO/Cu_2O solar cell. A number of solutions has been suggested to increase the quality of the junction, like using growth order to create higher lattice matching[53], using wet chemical etching to remove CuO and other contaminants before ZnO is deposited [56], and using nanoscale structuring to

increase interface surface area [57]. The most popular method used to increase junction quality is inserting a buffer layer between the ZnO and the Cu_2O layers.[56]

Lattice Matching

One of the larger drains on the conversion efficiencies in ZnO/Cu_2O junctions is induced by defects that arise from lattice mismatch between the individual materials. Akimoto et al. [53] did a comparative study of two heterojunction structures, one where ZnO was deposited on Cu_2O (structure-I) and another where Cu_2O was deposited on ZnO (structure-II). It was found that depositing Cu_2O on ZnO was far superior to the reverse, with respect to crystallographic orientation, defects, as well as with respect to current-voltage characteristics. This superiority was prescribed to the fact that the hexagonal structure of the (0001) orientation of Wurtzite ZnO induced growth of the similarly hexagonal (111) orientation of Cu_2O. The structure of the (0001) ZnO orientation and the (111) Cu_2O orientation are shown in Figure3.2.This similar structure causes a lattice mismatch calculated by Akimoto et al. to be 7.1%

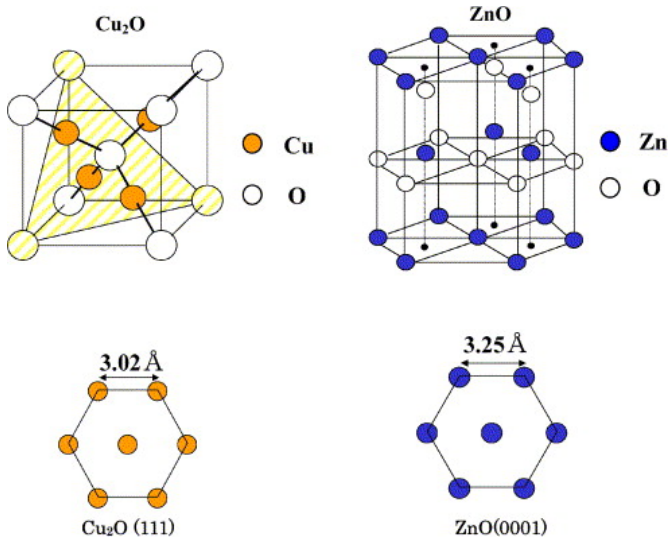

Figure 3.2: Crystal Structures of the atomic arrangements of Cu_2O and ZnO as made by Akimoto et al. [53]

Figure 3.3 shows the XRD profiles of structure-I and structure-II. Clearly structure-2 has superior crystallographic alignments, where the ZnO (0001) peak and the Cu_2O (111) peak are both clearly defined, with small FWHM indicating large crystallite sizes.

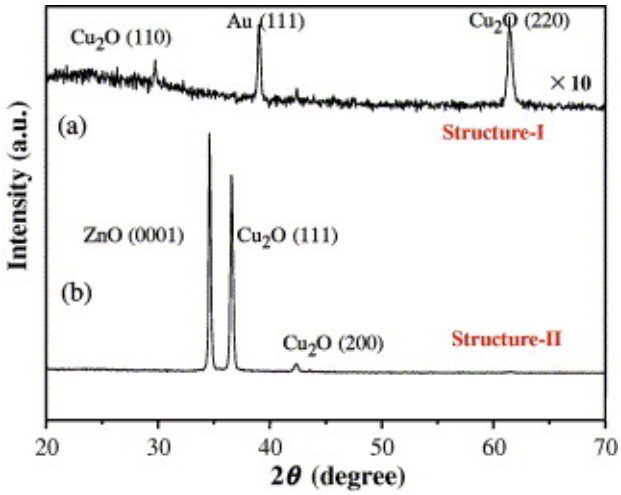

Figure 3.3: XRD profiles of structure-I (ZnO grown on CU_2O) and structure-II (Cu_2O grown on ZnO) as made by Akimoto et al. [53]

Note that the (0001) orientation of the ZnO is the same as its (002) orientation in simplified notation. After this point (002) will be used to describe the hexagonal face of the ZnO crystal structure.

Wet Chemical Etching

Another method used to increase junction efficiency is treating polycrystalline Cu_2O sheets with wet etching to remove traces of CuO on the surface before ZnO is deposited on the sheets. This method was used by Miyata et al. [56] among others for decent results. They obtained a smooth Cu_2O surface without any CuO, by first treating with a solution of iron chloride ($FeCl_3$) and hydrochloric acid (HCl), then a solution of nitric acid (HNO_3) and sodium chloride (NaCl), and last ammonium persulfate ($(NH_4)_2S_2O_8$).

Nanoscale Structures

Changing the architecture of the pn-junction has also been suggested as a method of increasing the efficiency of ZnO/Cu_2O junctions. Musselman et al. [57] used nanostructures to reduce the electron transport lengths, and thus decreasing the chance of recombination. They used electrodeposition to create a self-assembling array of ZnO nanowires into the core of the Cu_2O material, which created a longer continuous junction containing abrupt interfaces. A diagram of the junction can be seen in Fig. 3.4. It was also found that this nanowire array decreased the optical depth of the absorbing material by scattering light and thus allowing charges to be collected from further into

the material.

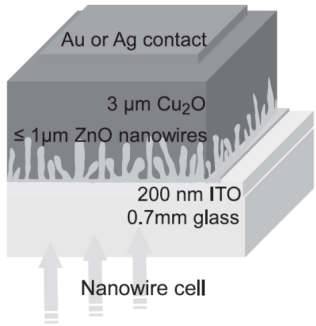

Figure 3.4: Schematic of cell designed with nanowires to decrease electron transport length. [57]

In his Doctoral thesis Yun Seog Lee [58] also investigated using nanostructures to increase the short minority carrier diffusion length of Cu_2O. Using colloidal lithography and hydrothermal growth, ZnO nanowire are grown into the bulk of the Cu_2O material. The power conversion efficiency saw an increase from 0.35 % to 0.88 % under 1-sun intensity with the added array, a small but not insignificant increase. Optical simulations were also performed to determine the effects of this geometry on light absorption, and it was found that the nanowire resulted in locally amplified absorption in the Cu_2O.

Cheng et al. [59] studied the possibility of using electrodeposition to deposit Cu_2 into cavity like nanopaterns that have been fabricated by lithography and hydrothermal growth into the ZnO layer. It was found that this technique increased the pn-junction area and enhanced the percentage of charge carriers that were collected. This gave a significant increase in the PCE from 0.15 % of the planar structure to 0.51 % in the nanostrucured device.

Introducing a Buffer Layer

It has been suggested by a series of people that adding a buffer layer between the p-type and n-type layers of the semiconductor could decrease the amount of mismatch and defects which act as recombination centers. A buffer layer may also prevent reduction from happening between the ZnO and Cu_2O layers, and it may decrease the recombination that occurs via tunneling.[56] [55] Evidence that adding a buffer layer increases the efficiency of the ZnO/Cu_2O junction can be seen in Table 3.1 in Section 3.3 where all the highest solar cell efficiencies that have been reached are made in cells

with buffer layers. Some of the highest ZnO/Cu_2O produced so far have been made from depositing additional layers by PLD on thermally oxidized sheets. Minami et al. [35] made two such cells one with a buffer layer which had the record efficiency of 5.38 % and another without which had the efficiency 2.53%. A number of materials have been suggested as capable of acting as a buffer layer. Jeong et al. [54] uses TiO_2, Miyata et al. [56] suggests both $Zn_{1-x}Mg_x$ and ZnO-In_2O_3, Yun Seog Lee [58] uses amorphous $Zn_{1-x}Sn_xO$ (a-ZTO), and Minami et al. [34] used $Zn_{1-x}Mg_xO/Cu_2O$. Finally, Minami et al. [35] as stated earlier, used to great effect Ga_2O_3, creating the highest recorded ZnO/Cu_2O junction.

The most commonly used buffer material is undoped or amorphous ZnO, as can be seen in Table 3.1 this has been done by a number of people such as Minami et al. [33], Nishi et al. [42], Lee et al. [43] and Lee et al. [44].

3.5.2 Improving Material Properties

Materials in a pn-junctions used for solar cells should have large grains, high mobility and low resistivity in order to maximize the quality of the cell. [30] It is therefore desirable to make the crystallinity of the materials involved as mono-crystalline as possible.

Producing Cu_2O materials with high quality

Depositing Cu_2O with a high level of crystallinity can be difficult, not just because of interfacial defect states, but also because it is tricky to avoid producing domains of CuO or Cu both in the bulk material and at the interfaces. Rakhshani et al. [60] made a review paper on the deposition and oxidation of cuprous oxide, and found the optimal pressure and temperature ranges for creating Cu_2O rather than CuO or Cu through thermal oxidation of Copper films. The results shown in the form of a phase stability graph are shown in Figure B.3 in Appendix B.

The phase stability results of thermally annealed copper found by Rakhshani et al. agrees with what Chen et al. [61] found in their study of PLD conditions to produce Cu_2O. Figure 3.5 clearly shows that using oxygen pressures of 0.004 Pa to 0.04 Pa yields pure Cu_2O thin films, and that at 0.4 Pa the result is a mixture of CuO and Cu_2O, and any higher pressures gives pure CuO.

Then using constant pressure of 0.04 Pa Chen et al. investigated a new set of Cu_2O films at a variety of substrate temperatures and found that the best crystallographic structure in the Cu_2O films deposited at higher substrate temperatures. Figure 3.6 shows that at

400°C the (200) orientation dominates the Cu_2O structure, and that as the temperature rises to 600°C or 700°C the (111) orientation becomes more dominant.

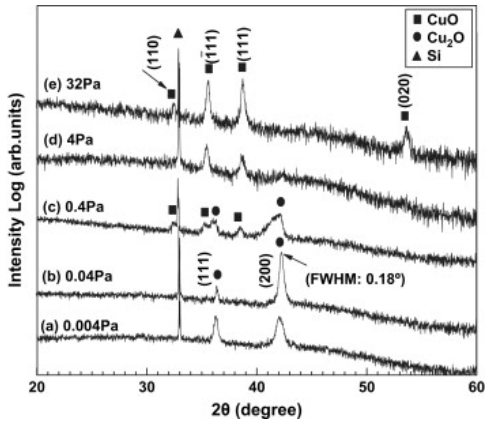

Figure 3.5: XRD patterns of Cu_2O films prepared at 500 °C with oxygen pressures of (a) 0.004 Pa, (b) 0.04 Pa, (c) 0.04 Pa, (d) 0.4 Pa, (d) 4 Pa and (e) 32 Pa. Made by Chen et al. [61]

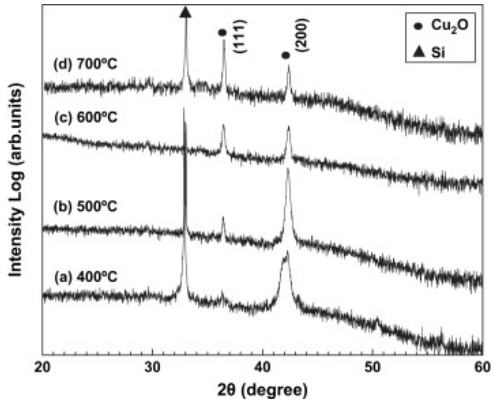

Figure 3.6: XRD patterns of Cu_2O films deposited under oxygen pressure of 0.04 Pa with substrate temperatures of (a) 400°C, (b) 500°C, (c) 600°C and (d) 700°C. as made by Chen et al. [61]

Rakhshani et al. [60] shows how the oxygen partial pressure during reactive sputtering affects the conductivity of the copper films produced, be they CuO, Cu or Cu_2O. As is shown in Figure B.4 in Appendix B the optimal oxygen partial pressure for production of higher resistivity Cu_2O films lies somewhere between 0.4×10^{-3} Torr and 0.6×10^{-3} Torr.

Low Resistivity Cu_2O

Mono crystalline Cu_2O with equivalent doping will be far less resistive than the polycrystalline variety,[30] so in order to tackle this challenge increasing the crystallinity should be considered in the ways that are described in the previous section. Specifically looking at resistivity, Mittiga et al. [30] found that slowly cooling the Cu_2O after oxidation would produce films with high resistivity whilst quench cooling the Cu_2O once it reaches 450 °C halved the resistivity. They also postulated that doping the Cu_2O with materials such as F, P, N, Cl, In, Mg, Si, Na or Cl might reduce the resistivity. They found that Cl doping was the best for this purpose, but it was also discovered that the doping had the effect of strongly reducing the minority carrier diffusion length. Malerba et al. [26] produced up to 2.5 at % nitrogen doped Cu_2O films and found that the films with higher nitrogen doping showed marked increase in conductivity. The film with the lowest nitrogen doping, 1.15 at % had a resistivity of 12 Ω cm whilst the one with 2.54 at % had a resistivity of 1.14 Ω cm. Malerba et al. claim that this is the lowest resistivity reported for this semiconductor.

High Quality ZnO

The crystalline quality of thin film ZnO depends strongly on the substrate upon which it is deposited. Shan et al. [62] wrote a paper describing how to optimize the electrical properties of ZnO when deposited on glass, GaAs (100), Si(111), and Si(100). It was found that the optimal deposition temperatures were 200 - 500°C for the glass, 200 - 500°C for the GaAs, 300 - 500°C for the Si(111), and 300 - 500°C for the Si(100). The crystallographic orientations of ZnO as a function of substrate temperature are shown in Fig.3.7 demonstrating these conclusions.

Shan et al. [62] suggest in their paper that the crystal structure of ZnO can be optimized for the (002) direction for any of the suggested substrates, as long as the substrate temperature during deposition is within the ideal range.

Shen et al. [63] also studied the effects of varying the substrate on the properties of the ZnO films. They compared glass substrates to two different synthetic plastic substrates, polyethylene naphthalate (PEN) and polyethylene terephthalate (PET) at room temperature under radio frequency magnetron sputtering. It was found that the glass substrates created compressive stress while the plastic substrates creates tensile stress.

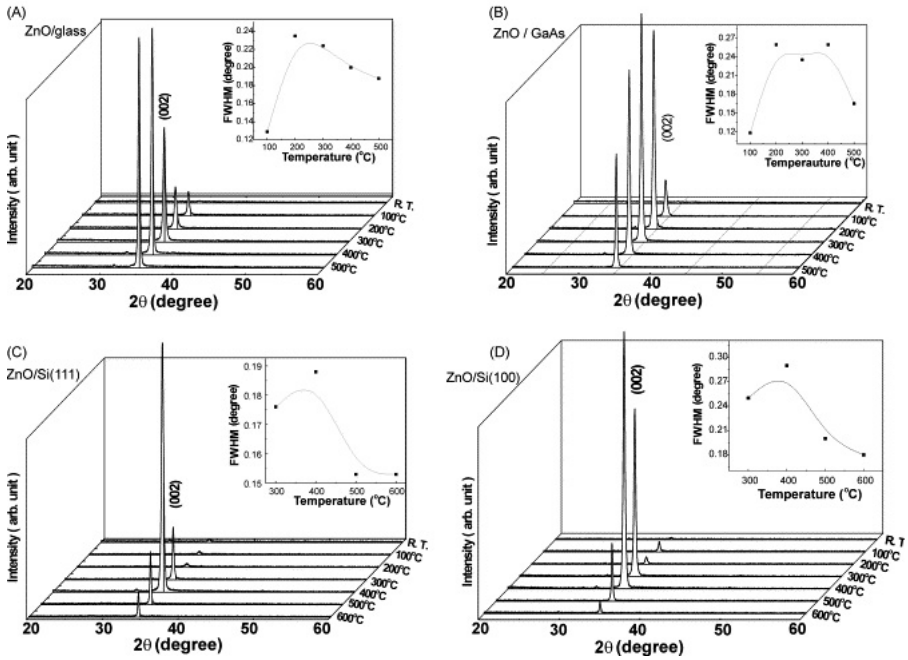

Figure 3.7: XRD patterns of ZnO thin films grown at different temperatures on glass (A), GaAs (B), Si (111) (C), and Si (100) (D). Shan et al.[62]

The XRD analysis shows that all three substrates produce highly oriented (002) films, but the glass substrates produce films with fewer additional peaks.

Cho et al. [64] found that increasing the deposition temperature during rf magnetron sputtering of ZnO thin films from 200 °C to 300 °C to 400 °C increased the grain size of the (002) orientation from 20 nm to 30 nm to 40 nm.

ZnO Electrical Properties

Kong et al. [65] studied the effects of deposition parameters on the electrical properties of AZO. In the study AZO was deposited on glass substrates by magnetron sputtering. It was found that using deposition temperatures of 250 °C and upwards increased the crystallite size and the conductivity of the AZO. Additionally, Kong et al. found that introducing any amount of oxygen into the chamber whilst depositing AZO by sputtering only lowered the conductivity of the films produced. This conclusions confirmed the earlier results Jeong et al. [66], who also demonstrate that low oxygen content produced the most conductive AZO films. Park et al. [67] found that increasing the substrate deposition temperature during magnetron sputtering to 400 °C and 500 °C further in-

creased the crystallite and grain sizes, in addition to decreasing the resistivity.

The results of Shen et al. [63] from the study of substrate effects on ZnO properties also discussed in the previous section, conclusively shows that glass substrates produces films with much better electrical properties than the synthetic plastic substrates. The film deposited on glass had lower resistivity, higher hall mobility and carrier concentration than the films deposited on PEN or PET.

Cho et al. [64] found tested ZnO resistivity at 100 °C, 200 °C, 300 °C and 400 °C and found that increasing the deposition temperature to 200 °C decreased the resistivity markedly from 1.2 Ω cm to 0.6 Ω cm and that at 300 °C and 400 °C the resistivity was almost constant at 0.5 Ω cm with only the 400 °C film being only slightly more conductive.

Tanaka et al. [68] deposited AZO by PLD rather than sputtering, and they found that 300 °C was the optimal substrate temperature for achieving high resistivity. Any higher or lower temperatures would decrease the resistivity and the carrier concentration.

3.5.3 Ohmic Electrode Contacts

Reducing the overall resistance in the junction is important to increase the effectivity of the cell, and to do this the ohmic contact between the Cu_2O and its electrode has to be optimized. One of the most commonly used metals for creating an ohmic contact to Cu_2O is Gold. [69] This is because it does not oxidize the Cuprous oxide to CuO or even Cu which can create a Schottky junction. [70]

To create an ohmic contact to the n-type ZnO, a conductive material with a lower work function than the electron affinity of ZnO need to be found. The electron affinity of ZnOs ranges from 4.2-4.35 eV. [71] Preciously both Al and Ti have been used for ohmic contacts of ZnO, as they have respective work functions of 4.28 eV and 4.33 eV. [72]

Chapter 4

Proposed Design

This chapter suggests a possible IBSC design that the materials studied in this thesis could form. Figure 4.1 shows a side view of the proposed design used in this thesis. The AZO, ZnO and Cu_2O layers are to scale relative to each other, that is, the Cu_2O is double the thickness of the AZO which is double the thickness of the ZnO. The Au, Mo and glass substrate thicknesses in this diagram are arbitrarily chosen. Figure 4.2 shows the same design shown from the bottom, so that the Au layer is exposed. The cell is designed so that light will pass through the glass substrate and Mo electrode fingers before reaching the pn-junction.

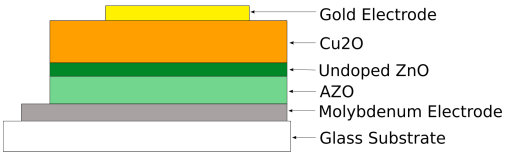

Figure 4.1: Profile view of layers in device

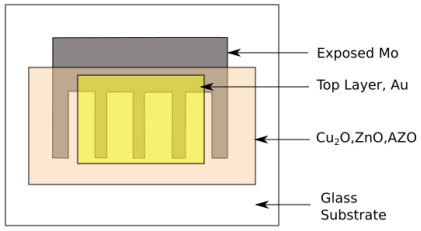

Figure 4.2: Top View of Cell after all layers have been deposited

First the limits for the deposition parameters used for deposition of Cu_2O will be discussed in Section 4.1, then ZnO material deposition parameters are discussed in Section 4.2. The order of the layers is explained in Section 4.3 and the buffer layer selection is described in Section 4.5. Electrode choices are discussed in Section 4.4 and finally substrate selection is discussed in Section 4.6.

4.1 Cu_2O

The first material whose deposition parameters need to be considered for the solar cell, is of course the p-type Cu_2O active material. Deposition parameters that are to be used will be selected to optimize crystal structure and conductivity, as outlined in Section 3.5.2.

4.1.1 Optimizing Cu_2O crystal structure

Section 3.5.2 outlines the findings of Chen et al. [61] and Rakhshani et al. [60] with respect to producing Cu_2O thin films with high crystalline quality. Their findings suggest that a temperature range of 600 and higher, as well as oxygen pressures lower than 0.04 Pa (3 x 10 $^{-4}$ Torr) are best for producing Cu_2O without CuO and Cu.

Additionally as shown in Section 3.5.1 depositing Cu_2O on ZnO will have the smallest amount of lattice mismatch because the hexagonal ZnO encourages growth of the (111) orientation in the cubic Cu_2O. This suggests then that the Cu_2O deposited in this thesis should be aimed at the (111) orientation to encourage lattice matching as this will likely decrease the defect density at the junction. The results from Chen et al. suggest that lower pressures, in the 0.004 Pa (3 x 10^{-5} Torr) range, will further discourage growth of the (200) orientation, in comparison to the (111) orientation, in Cu_2O. This should then be kept in mind during deposition for this thesis.

Figure 4.3 is based on the research of Chen et al.[61] on deposition parameters of Cu_2O by PLD. The figure shows a rough outline of the parameters that need to be applied to produce films made of Cu_2O and not CuO. As can be seen in the figure, the temperatures need to be higher than 400 °C and the oxygen pressures lower than 0.4 Pa (3 x 10^{-3}Torr).

For choosing specific parameters inside the range suggested by the PLD research by Chen et al. we consider the thermal oxidation data from Rakhshani et al. [60]. Their data suggest that using temperatures at about 700 °C and oxygen pressures of about 1 x 10 $^{-3}$ Torr to 1 x 10 $^{-5}$ Torr may work, and these parameters are fairly appropriate, since this pressure and temperature ranges is easy to achieve with the available PLD system.

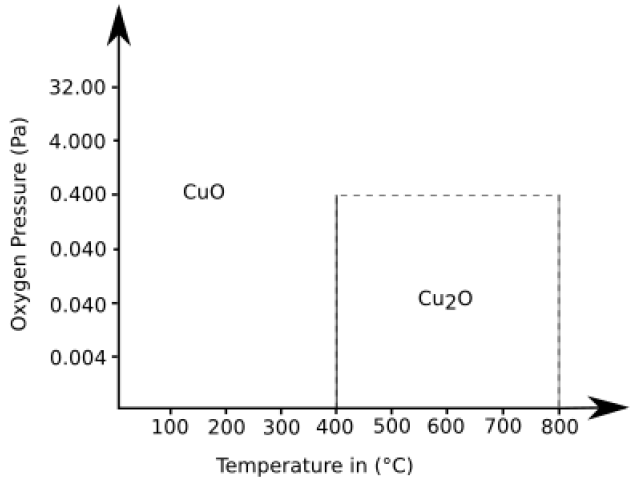

Figure 4.3: The temperature and oxygen pressure settings needed to create pure Cu_2O and not CuO during PLD. The dotted line suggests that an oxygen pressure lower than 0.4 Pa is needed.

4.1.2 Cu_2O as an IBSC material

Malerba et al. [26] conducted a study on nitrogen doped Cu_2O as a possible IB solar cell material. For this purpose they looked at the effect of doping level on the transmittance and the absorbance spectra to determine if doping produced the desired IB rather than simply producing impurity based non-radiative recombination centers. The study found that they were able to produce Cu_2O films doped with varying levels of nitrogen, during RF magnetron sputtering with a relative flow rate ($F(N_2)/F(O_2)$) from 0.145 to 0.155 sccm. This resulted in films with doping levels ranging from 1.15 at. % to 2.54 at. %. As Fig. 4.4 clearly shows, increased doping gives a lower transmittance and a higher absorbance.

The additional absorbance in the photon energy spectrum occurs at about 0.45 eV and 0.72 eV, which is well below the 2.1 eV bandgap of the Cu_2O. Additionally, the intensity of these absorption bands correlate well with the nitrogen doping levels.

Malerba changed the nitrogen doping by adjusting the oxygen flow compared to the nitrogen flow. So similarly, for this thesis, changing the relative oxygen and nitrogen flow during Cu_2O deposition will be attempted in order to dope the Cu_2O with nitrogen. It must however be kept in mind that the films produced by Malerba were made by sputtering, not PLD, so actual flow values are not comparable.

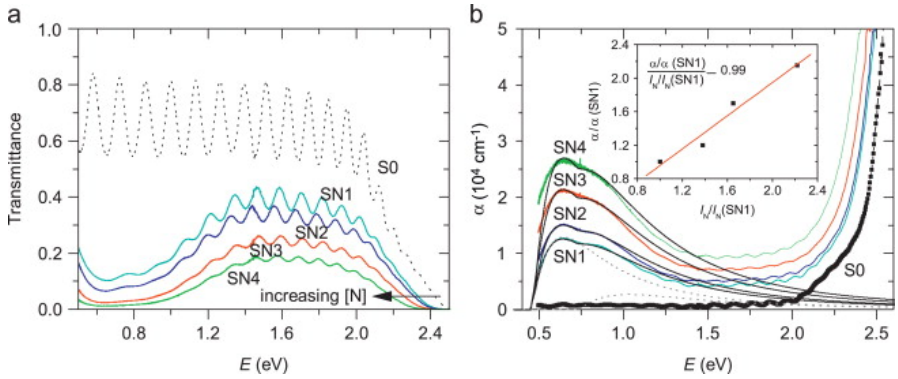

Figure 4.4: Transmittance (a) and absorption coefficient (b) spectra of doped and undoped samples. For the less doped sample the two single contributions of αIR are also reported as an example. Figure made by Malerba et al [26]

4.2 AZO

Aluminum doped zinc oxide, often called AZO, will be used for the n-type material in this thesis. The quality of the AZO layer is vital both because as the n-type material it needs to have a high electron mobility, and because its it will act as the substrate for the Cu_2O layer and a high defect density will induce junction defects and other similar problems.

It will be assumed in this thesis that AZO and ZnO react fairly comparably in terms of changes to crystalline quality and resistivity as a reaction to changes in the deposition parameters. However, it needs to be noted that Lee et al [32] found that increasing the aluminum doping, whilst keeping other deposition parameters constant, will decrease the crystallite size of the (002) orientation from 48.27 nm when there is no Al doping to 36.20 nm when there is 1 at. % Al doping and 33.41 nm when there is 4 at. % Al doping. Grain size was also seen to decrease with increased doping, as measured by SEM. Additionally the Hall mobility was seen to decrease slightly with Al doping, and this was probably a result of the decreased grain sizes, since the grain boundary scattering would increase with smaller grains. However, as is to be expected and desired, the resistivity decreased markedly with 1 at. % Al doping.

As shown in Section 3.5.2 ZnO, and thus AZO, will generally orient hexagonally with the c-axis perpendicular to the substrate within varying deposition parameters depending on the substrate. That is to say, grow in the (002) orientation. Shan et al. [62] found that for glass substrates the optimal substrate temperatures during deposition is in the 200 - 500 °C range. Kong et al. [65] found that crystalline properties of AZO will be more

desirable when the AZO is deposited at temperatures around 250 ° with no additional oxygen in the deposition chamber. However, they also found that higher temperatures than 250 ° would slightly increase the resistivity again. Park et al. [67] However, found that increasing the substrate deposition temperature to 400 °C or 500 °C only further increased the crystallite size of the (002) orientation and decreased the resistivity.

For the deposition of AZO for this thesis then, deposition temperatures of 300 °C and 400 °C will be investigated, and no oxygen will be introduced into the chamber.

4.3 Deposition Sequence

As was outlined in Section 3.5.1 the deposition sequence of ZnO and Cu_2O has a large effect on the lattice mismatch and defects. Akimoto et al. found that the ideal sequence is to deposit ZnO first and then Cu_2O over it, as the spontaneous growth of the (002) orientation in the ZnO structure encourages growth of the (111) orientation in cubic Cu_2O. This structure has a lattice mismatch of 7.1%,.

4.4 Electrodes

Selecting metals that work as electrodes without causing significant losses is an important part of designing a solar cell. One of the most important parameters that need to be considered to select an electrode material is its work function.

4.4.1 Bottom electrode, Molybdenum

The most tricky electrode to determine a material for was the bottom electrode, which should create an ohmic contact to the AZO layer.

Commonly used: Aluminium

Previously made junctions using Cu_2O as the active material commonly use Cu foil heated in an oven, upon witch AZO and electrodes are then deposited. Alternatively electrodeposition or sputtering has been used on most active materials. For these kinds of junctions aluminum is a common electrode material. This project revolves around doping the Cu_2O with nitrogen, something that necessitates that the Cu_2 be made by some other molecular deposition method. Depositing Cu_2O rather than Cu or CuO requires certain parameters of temperature and pressure.

The temperature parameters necessary to create Cu_2O rather than CuO or Cu necessitates that the electrode deposited before the copper would need to withstand temperatures up to 800°C without loosing structure or softening. This made choosing the commonly used material aluminum for the bottom electrode nonideal as it has its melting point at 660°C and its softening point at 330°C.

Molybdenum

Since aliminuim will not be a viable choice for electrode, another metal with a higher melting point needed to be found. Molybdenum is a metal whose melting point, 2623 °C is far above the temperatures needed to deposit Cu_2O, and is therefore considered.

Kamohara et al.[73] studied the use of Mo as an electrode for an aluminium nitride (AlN) film. AlN has the same crystal structure as AZO, wurtzite, with fairly similar lattice constants a = 3.11 Å for AlN and a = 3.25 Å for AZO. Kamahora et al. found that Mo was an ideal electrode with respect to crystal structure. As can be seen in Fig. 4.5 the wurtzite material orients nicely on top of the Mo. Kamohara et al further studied the use of an inter layer to further increase crystal quality and decrease interface defects, but this will not be attempted in this thesis due to time constraints.

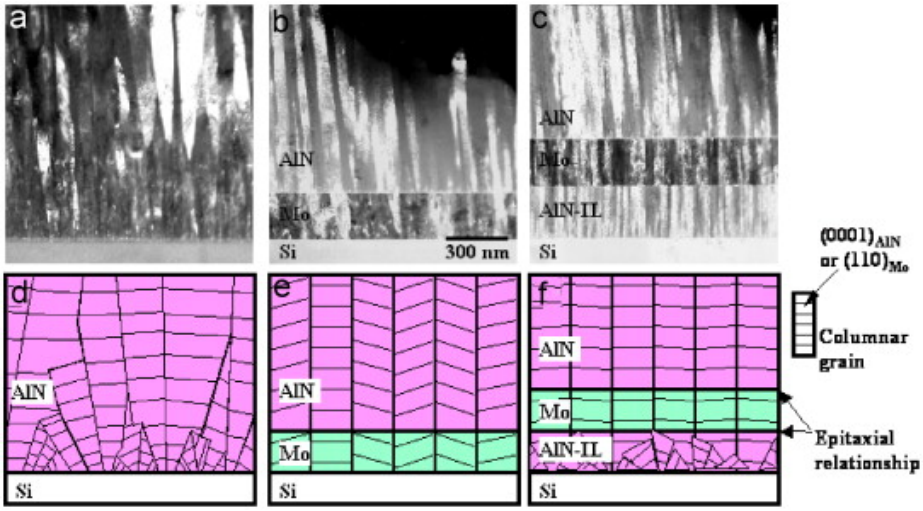

Figure 4.5: TEM dark field images of cross-sectional of AlN films prepared at a sputtering pressure of 0.36 Pa on (a) Si, (b) Mo/Si and (c) Mo/AlN-IL/Si substrates taken with reflection of g=011¯1 for AlN. Schematic diagrams of cross-sectional: (d) AlN/Si, (e) AlN/Mo/Si and (f) AlN/Mo/AlN-IL/Si samples as made by Kamohara et al.[73]

Kashyout et al. [74] made Molybdenum thin films on a soda lime glass substrate by DC magnetron sputtering, and then measured the electrical properties as well as the structural properties of the films. Figure 4.6 shows that longer deposition times and higher deposition power will create electrodes with lower resistivities, and Figure 4.7 shows that using substrate temperatures higher than 200 °C is ideal is the deposition power is 200W.

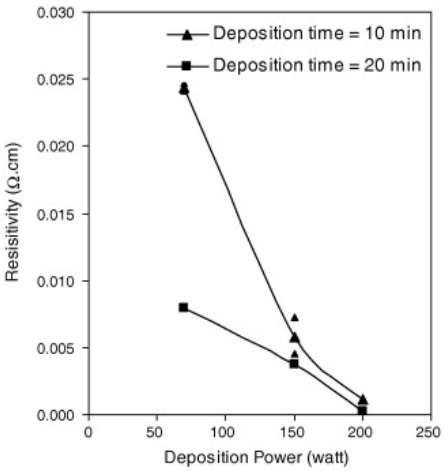

Figure 4.6: Molybdenum resistivity versus deposition power, for deposition times of 10 and 20 min, deposited on substrates with temperature 450 °C as made by Kashyout et al. [74]

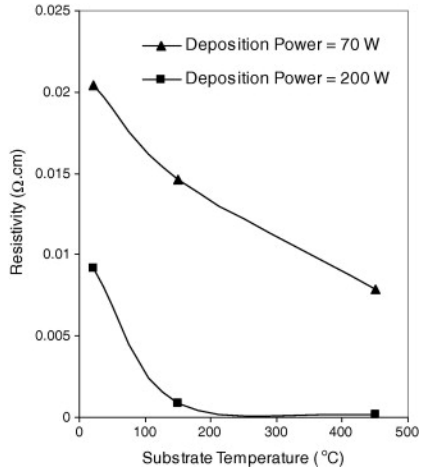

Figure 4.7: Molybdenum resistivity versus substrate temperature, made at deposition powers of 70W and 200W, for samples prepared with a 20 min deposition time as made by Kashyout et al. [74]

The work function of Mo can be engineered to be anywhere between 4.3 eV and 4.95 eV. [75] This could be a problem, as the an ohmic contact electrode should have a lower work function than the electron affinity of the contact material. The electron affinity of ZnO ranges from 4.2-4.35 eV, [71] so Mo could work as an electrode and it could potentially fail if its work function is too large.

4.4.2 Top electrode, Gold

Gold is a common electrode contact material for Cu_2O, and it has been used and confirmed by papers such as Li et al. [55] or Jeong et al. [54]. Gold has a work function of 5.1 eV, which falls well within the Cu_2O bandgap.

4.5 ZnO, Buffer Layer

Section 3.5.1 describes the advantages of using a buffer layer between the AZO and Cu_2O layers. A number of materials are suggested as viable options, and among them undoped ZnO is suggested. This is a readily available material in our lab, and as such will be used in this thesis.

4.6 Substrate

As shown in Section 3.5.2, choosing the right substrate can strongly affect the ZnO deposited on it. Of the materials studied by Shan et al. [62] the cheapest and most readily available material is glass. Common glass microscope slides will be cut into shape and cleaned before use in this thesis.

Chapter 5

Methodology and Experimental Setups

The main purpose of the experimental side of this project was to investigate the materials in the ZnO/Cu_2O junction, and to use the parameters investigated to attempt to produce a functioning solar cell and an IB version of the same cell. The main method of thin film production was Pulsating Laser Deposition (PLD), and it was used to produce AZO, ZnO and Cu_2O. The experimental setup of this deposition method is described in Section 5.1 and the methodologies of the layers deposited by this method is described in the subsections 5.1.1, 5.1.2 and 5.1.3.

The deposition method used for production of the conductive contacts was magnetron sputtering and electron beam evaporation, the setup and methodology for these depositions are described respectively in Sections 5.2 and 5.3.

To characterize the films produced by PLD, the main methods were X-ray Diffraction (XRD) and Four Point Probe. The setup for these characterization methods are described in sections 5.5.2 and 5.5.3. Additionally transmission electron microscopy (TEM), described in Section 5.5.4 and X-ray photoelectron microscopy (XPS), described in Section 5.5.5 was used to study some Cu_2O films.

5.1 Pulsed Laser Deposition (PLD)

The main method for the production of the thin films in this project are made by PLD. This deposition method works by focusing a laser onto a target of a particular material that is to be deposited. The energy from the laser vaporizes the material in the target into a plasma plume directed upwards. The substrate that the material is to be deposited on is placed facing down inside the plume, usually in the outer edges, and the contents of the plasma will then solidify onto the substrate.

The setup of the PLD chamber used in this thesis is drawn in Fig. 5.1. In this figure it is shown how the laser enters the chamber through a quarts window, which is rotatable, removable and cleanable. The laser beam then hits a target that can rotate individually and by a carousel. This rotation is designed so that the laser impact is distributed around the target so it not hit the same spot repeatedly, in order to minimize target damage and pocketing. Such damage could make continued use of the same targets produce films of decreasing quality. The laser impact on the target creates a plasma plume on impact with the laser, as shown in Fig. 5.1. To produce the thin film the substrate is then placed at some point inside the plume, allowing plasma ions to land and form crystal lattices. A heater of adjustable temperature is inside the substrate stage, allowing the backside of the substrate to be heated. The substrate stage can also be rotated to increase film uniformity.

In this particular project a 248 nm KrF laser working at 25 kV is used. This gives roughly the average power of 95 mJ per pulse, as measured by a power meter after the final focusing lens, before the beam enters the vacuum chamber. To maximize power at the target, the target is placed at the focal point of the final lens directing the laser. The actual power of the beam will be slightly less at the target than that measured outside the window, as some energy is absorbed or reflected by the quartz. This loss is minimized by rotating and cleaning the window once all clean spots have been rotated through. In addition to this, the laser power depletes naturally in cycles as the gas inside the laser chamber is used. To counteract this the high voltage was be adjusted slightly in order to keep the beam power before before the quartz window roughly constant at 95 mJ per pulse.

Changing the particle energy of atoms in the plume will systematically change the texture and microstructure of films produced. Particle energy can be changed by adjusting the high voltage, which will change the fluence at the target, or changing the repetition rate. A higher repetition rate results in a higher vaporization rate of the target, and thus

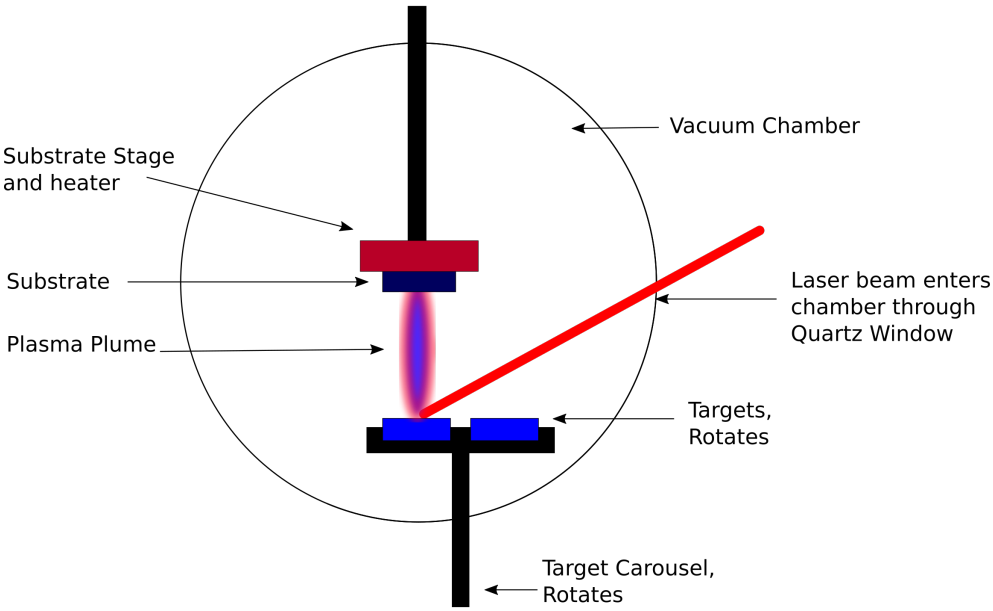

Figure 5.1: Schematic of our PLD system

a higher deposition rate. The energy change when changing pulse rate occurs as a result of the laser having less time to recharge between each pulse, and thus each individual pulse contains less energy. Another method of changing the particle energy is changing the substrate-target distance during deposition. The kinetic energy of atoms will vary depending on their distances from the target since the atoms in the outer edges of the plume will have travelled further and lost more energy. [76]

5.1.1 AZO

In this work, AZO films deposited from an alumina and zinc oxide target are used as the n-type layer in the AZO/Cu_2O junction. The target is made from a mixture of ZnO and Al_2O_3, with 98 wt % ZnO and 2 wt % Al_2O_3. To determine the settings that are to be used for films in the complete junction, a series of independent AZO films grown on glass substrates by PLD are made.

Literature studies, discussed in Section 3.5.2, show that the growth of AZO by PLD is best accomplished at around 400 °C and above if crystalline growth is of importance.

If the resistivity is to be as high as possible, then the deposition temperature should be around 300 °C or higher as has been found by Tanaka et al. [68] and Cho et al. [64]. To decide on the optical temperature for the purposes of an AZO/Cu_2O junction in this thesis, then AZO films deposited by PLD with temperatures of 400 °C and 300 ° will be made.

To test for the optimal substrate-target distance during PLD of AZO, films will be deposited with substrate-target distances of 45 mm, 55 mm and 65 mm for substrate temperatures of both 400 °C and 300 °C.

All AZO films deposited at 300 °C were deposited for 20 000 pulses at 5 Hz. The films made at 400 °C will be deposited for all three substrate-target distances for both 20 000 pulses and 40 000 pulses at 5 Hz.

5.1.2 Cu_2O

As shown in Figure B.3 and in Section 3.5.2 the deposition of Cu_2O should take place within a certain temperature and pressure range to avoid CuO or Cu in the sample. The cooling of the samples takes place at high vacuum, so that the films are not exposed to the CuO phase stability region while cooling. All Cu_2O samples were deposited with a substrate temperature of 750 °C, a substrate-target distance of 55 mm and for 40 000 pulses at 5 Hz unless otherwise stated. A full list of Cu_2O films produced is shown in Table 5.1.

The first Cu_2O thin film deposited was made as an undoped control. 3 sccm of O_2 and no nitrogen was introduced in the chamber. The chamber pressure was 1.3 x 10 $^{-3}$ Torr.

Next a film was made with nitrogen introduced to attempt to create an IB material. 3 sccm of O_2 and 30 sccm of N_2 was introduced into the chamber, making the pressure during deposition 3.6 x 10 $^{-3}$ Torr.

Changing the nitrogen/oxygen flow rate ratio in the tank was done in an attempt to induce doping. 1 sccm of O_2 and 33 sccm of N_2 was introduced into the chamber, making the pressure 3.7 x 10 $^{-3}$ Torr.

Once again the nitrogen/oxygen flow rate ratio was changed, with 0 sccm of O_2 and 33 sccm of N_2. This time the total pressure in the chamber was 3.7 x 10 $^{-3}$ Torr.

It was attempted to use sputtering of Cr atoms during PLD to create nitrogen ions that would more readily incorporate into the Cu_2O lattice. This was theorized to work, since previously successful attempts to dope Cu_2O with nitrogen were done during sputtering processes, such as that done by Malerba et al. [26] or Nakano et al. [84]. These two films were only sputtered for 20 00 pulses at 5 Hz. There was 2 sccm of $)_2$ and 5 sccm of Ar in the chamber during both depositions, while one had 30 sccm of N_2 and the other 5 sccm of N_2 in the chamber. The Cr was sputtered at 50 W.

Two films were made at a substrate temperature of 650 °C for 40 000 pulses at 10 Hz, with a substrate-target distance of 45 mm and 1 sccm of O_2. One was made with 25 sccm of N_2 and a chamber pressure of 6.8 x 10^{-3} and the other with 5 sccm of N_2 and a chamber pressure of 9.1 x 10^{-3}

Table 5.1: List of Cu_2O films produced in this thesis, with identifying factors

Substrate temperature	Chamber Pressure (Torr)	O_2 (sccm)	N_2 (sccm)	Ar (sccm) Cr sputter	Name
750 °C	1.3 x 10^{-3}	3	0	-	3O2,00N2,750
750 °C	3.6 x 10^{-3}	3	30	-	3O2,30N,750
750 °C	3.6 x 10^{-3}	1	33	-	1O2,33N2,750
750 °C	3.7 x 10^{-3}	0	33	-	0O2,33N2,750
750 °C	6.0 x 10^{-3}	2	10	20	2O2,10N2,20Ar,750
750 °C	9.1 x 10^{-3}	2	30	5	2O2,30N2,5Ar,750
650 °C	6.8 x 10^{-3}	1	25	-	1O2,25N2,650
650 °C	1.9 x 10^{-3}	1	5	-	1O2,5N2,650

5.1.3 ZnO

Undoped ZnO films will be deposited from a Zn target made from melted Zn sheets. To obtain ZnO rather than Zn from deposition, 10 sccms of oxygen is introduced into the chamber during deposition.

All Zn films deposited in this thesis were made with a substrate temperature of 400 °C, a substrate-target distance of 55 mm, 10 sccm of O_2 in the chamber, so that the pressure in the chamber was 1.9 x 10^{-3}. The films were deposited for 10 000 pulses at a rate of 5 Hz

5.1.4 Solar Cells

All full solar cells were made with the same Mo and Au electrodes as described in Sections 5.2 and 5.3. This section describes the varying combinations of compositions of thin film layers produced by PLD that make up solar cells produced in this thesis.

Unless otherwise stated, the first layer deposited by PLD for all Solar cells was an AZO layer made at a substrate temperature of 400 °C, with a substrate-target distance of 5 Hz, for 20 000 pulses at 5 Hz. The next layer deposited was an undoped ZnO layer made at 400 °C, with a substrate-target distance of 5 Hz, for 10 000 pulses at 5 Hz. All substrate-target distances for the Cu_2O were 55 mm, Cu_2O films used in cells were all deposited for 40 000 pulses at 10 Hz, and the substrate temperature was 750 °C unless otherwise stated. All but one of the Cu_2O layers used in cells are identical to Cu_2O films deposited and studied individually. The Cu_2O films can be seen in Table 5.1.2.

The first five cells were made with the ZnO buffer layer, and Cu_2O layers made with increasing nitrogen content and decreasing oxygen content as shown in Section 5.1.2. The fifth cell was the only cell made with a Cu_2O layer that was not studied individually, as it was damaged. The Cu_2O film in question was made with 40 000 pulses at 10 Hz, 10 sccms of O_2 and 20 sccms of N_2 and a substrate temperature of 750.

The last two cells made were without the undoped ZnO layer. Both were simply designed with the standard AZO layer and a Cu_2O layer. The Cu_2O layers were both made at 650 °C for 40 000 pulses at 10 Hz with 1 sccm of O_2. The difference was that one was made with 25 sccm of N_2 and the other with 5 sccm of N_2 in the chamber.

Table 5.2: List of Solar Cells as a product of their layers

AZO	ZnO	Cu_2O	Name
400C,55mm,20k	400C,55mm,10k	3O2_00N2_750	Cell 1
400C,55mm,20k	400C,55mm,10k	3O2_30N2_750	Cell 2
400C,55mm,20k	400C,55mm,10k	1O2_33N2_750	Cell 3
400C,55mm,20k	400C,55mm,10k	0O2_33N2_750	Cell 4
400C,55mm,20k	400C,55mm,10k	10O2_20N2_750	Cell 5
400C,55mm,20k	-	1O2_5N2_650	Cell 6
400C,55mm,20k	-	1O2_25N2_650	Cell 7

5.2 Sputtering, Mo

Sputtering is a widely used technique both for eroding surfaces and for depositing materials. Sputtering occurs when a plasma is accelerated at a target material, the target ions then hit surface atoms of the target and with enough kinetic energy the atoms can be knocked free. These ejected atoms are then called sputtered atoms. The process is described visually in Figure 5.2

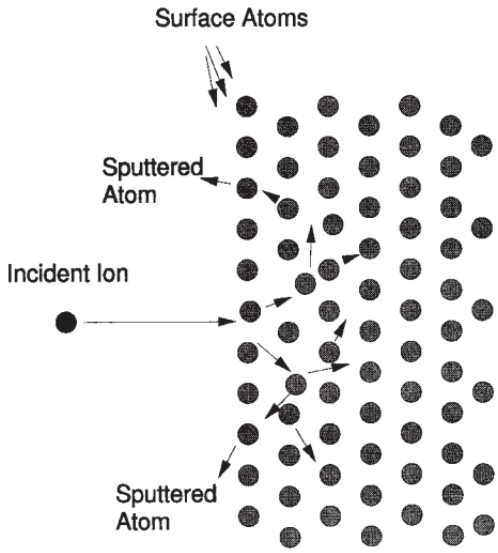

Figure 5.2: Atomic scale schematic of sputtering process[77]

If sputtering is to be used as a technique for etching, the surface that is to be cleaned is placed directly in the way of the target atoms, allowing the surface atoms to be knocked off and the material cleaned. This type of plasma cleaning works as a form of sandblasting that forms microscopic erosions on a surface without having to chemically treat it. For depositing through sputtering, a substrate of some kind is placed in the way of the sputtered atoms so that the atoms can hit the substrate and form a thin film on it. Thus the deposition works by collecting the atoms onto a substrate that are eroded off of a target material.[77]

The accelerated plasma is usually made up of inert ions, like Ar^+ or Kr^+, alternatively small molecular ions like O_2^+ or N_2^+ can be used.[77] The sputtering plasma used for this

project consisted of Ar^+ ions.

For the purpose of this thesis, sputtering is to be used for the deposition of metal electrodes. Kamohara et al. [73] used rf magnetron sputtering to create Mo bottom electrodes for AlN films and found that it was a good deposition method for this purpose.

This project uses an Custom ATC-2200V model AJA Sputter and Evaporator. A dc energy source was used to sputter a Molybdenum target under 200W for 20 minutes to provide electrodes that were about 100 nm thick. The glass substrates are taped to a substrate stage with a mask over them. The mask is a steel plate larger than the substrate, with a hole cut into it that allows the deposited Mo to form fingers going perpendicularly out of a contact bar. An image of the mask can be seen in Fig. C.1 in Appendix C. The glass substrates were pre-cleaned by plasma etching for 3 minutes before deposition, removing the top nanometers of contamination and surface roughness.

5.3 Electron Beam Evaporation, Au

Electron Beam Evaporation is a thin film deposition technique that targets a high energy beam of electron at a material, causing a vapor to form that can then condense on a substrate. In more detail, the source material is placed in a crucible. Inside the crucible a filament is placed under a large voltage, producing a beam of electrons. This beam is then guided by a series of magnets to hit the surface of the source material, heating it above its evaporation point. This causes a vapor of the material to rise like a plume, which then can solidify and produce a film on the surface of a substrate placed upside down inside the vapor. [77]

E-beam evaporation is preferable to regular thermal evaporation because it allows a larger amount of energy to be placed into the source material. This makes yields films with higher densities and higher adhesion to the substrate. [77]

In this thesis, the final layer of Au is deposited by E-beam evaporation. samples are taped to a substrate stage with a mask over them. The mask consists of a steel plate larger than the cell, with a 1.0 cm x 0.7 cm hole cut into it. This hole is smaller than the Cu_2O layer, so that the Au layer can be deposited without coming into contact with the Mo electrode and shorting the cell. An image of the mask can be seen in Fig. C.1 in Appendix C. Deposition is set to deposit an Au layer that is 50 nm at a rate of 10 nm per minute.

5.4 Substrate Preparation

All thin films are originally deposited on 18 mm x 18 mm glass substrates that are 1 mm thick. These are made from microscope slides that are cut into shape by a diamond scribe. To produce optimal and uncontaminated substrates, the glass squares are first placed five minutes in a glass beaker with Acetone in a sonic cleaner, then they are transferred to a new beaker with IPA, and again cleaned sonically for five minutes. Then they are removed and dried with small gusts of nitrogen gas, and placed in a sample holder that has been cleaned similarly. Gloves are worn at all times during handling of samples and sample holder to avoid causing contamination on the substrates from skin and fingerprints. Once the substrates are cleaned, they and the sample holder are placed in the vacuum chamber as quickly as reasonably possible.

5.5 Solar Cell Testing and Thin Film Characterization

Once thin films are produced they are tested by a number of methods. The setup and theory behind the characterization methods are described in this subsection.

5.5.1 Profilometer

It is necessary to know film thickness for the purposes of calculating resistivity, and for comparing crystallite sizes. For measuring the thickness of the films a Deltak 150 Profilometer was used. The Deltak 150 is a contact stylus profilometer that works by running a stylus over a sample surface whilst recording any height differences. These height differences are then sent to a computer. The resolution of the profilometer is supposed to be 1 Å, however, it was found during measurement that for the films made in this thesis, which were at the 1000 Årange, it was difficult to achieve measurements with any accuracy. Measuring the height at the same spot could give results varying with as much as 50 % error. For this purpose all thin film thicknesses were rounded to to nearest 100 nm (or to the nearest 1000 Å).

5.5.2 Xray Diffraction (XRD)

The classic XRD measurement works by sending an X-ray towards a sample at some incident angle before the beam is then scattered by the sample. The scattered X-rays will interfere destructively and constructively, giving rise to peaks of varying intensity, creating a diffraction pattern with intensity peaks that appear at characteristic values of 2θ according to the crystal structure diffracting the photons. The location and intensity of the measured 2θ values depend on the crystal structure that diffract them and can

thus give valuable information such as the chemical nature and the arrangement of the atoms.[78]

Braggs Law, shown in Equation 5.1, describes how X-rays interact with crystal planes. Two incoming parallel X-rays will reflect off of two parallel crystal planes as shown in Fig. 5.3. The X-ray hitting the bottom plane will have to travel slightly further than the top X-ray, causing a phase difference that can be used to calculate the distance d between the two planes. [78]

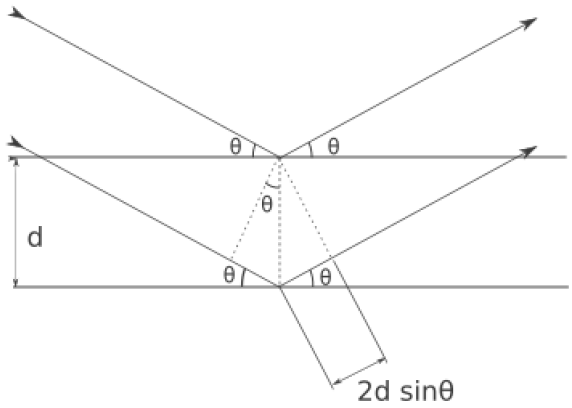

Figure 5.3: Two parallel X-ray waves reflecting off of two parallel atomic planes separated by the distance d, according to braggs law

$$s2dsin\theta = n\lambda \tag{5.1}$$

The distance d calculated by Braggs equation can then be used to determine the size of a unit cell with axes a, b and c, using the (hkl) indexes of the crystal planes. For a cubic material this relation is simple as the lattice constants a = b = c and becomes as shown in Equation 5.2. [78]

$$\frac{1}{d^2} = \frac{h^2 + k^2 + l^2}{a^2} \tag{5.2}$$

For the more complicated hexagonal structure where a ≠ b ≠ c, the relation is more complicated as shown in Equation 5.3. [78]

$$\frac{1}{d^2} = \frac{4}{3}\frac{h^2 + hk^2 + k^2}{a^2} + \frac{l}{c^2} \tag{5.3}$$

The method used to analyze the thin films by XRD is called grazing incidence. The setup of such measurements is shown in Fig. 5.4, which shows an X-ray beam hitting the target with a small constant angle ϕ designed so that the beam only hits the film and not the substrate. The X-ray is then diffracted by the film at a variety of angles 2θ which the detector can measure by moving in the vertical plane.

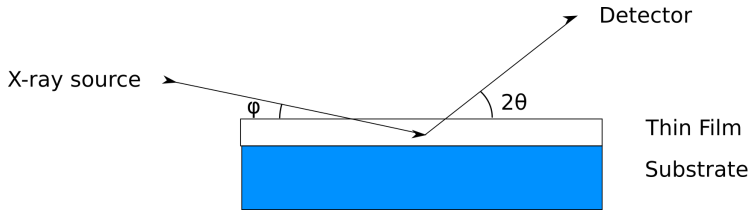

Figure 5.4: Setup of a Grazing Incidence XRD measurement

A disadvantage with using grazing incidence is that the X-ray only hits one spot on the thin film, so it can only measure a small sample of the entire film. This could potentially be a problem if the measured section of the film is not a representative of the entire film.

For all measurements done in this thesis the incoming angle ϕ is 1°, the measurements were done in the 2θ range 25° - 75° for two hours. The measurements were preformed by a D8 Advance DaVinci produced by Bruker, and the software used to analyze peaks was *diffract.suite EVA*.

Peak Profile Analysis

One of the most valuable pieces of information that can be gleaned from an XRD measurement is the crystallite size of the orientation. This value can be calculated from the FWHM of the peak corresponding to that orientation using the Scherrer equation shown in Eq. 5.4

$$\tau = \frac{K\lambda}{\beta cos\theta} \tag{5.4}$$

Where τ is the mean size of the crystalline domains. This value may be smaller or equal to the grain size. K is a dimensionless shape factor that is generally close to one, but varies slightly according to the shape of the crystallite. λ is the x-ray wavelength used to make the XRD measurement. β is the FWHM of the peak in radians, after the instrumental line broadening has been subtracted. Finally, θ is the Bragg angle the measure-

ment was taken at.

For the purposes of our experiment the incident angle is 1 °, the X-ray wavelength is 1.5406 Å from a Cu anode. Since the calculations of crystallite sizes will be for comparison within the paper, the shape factor K can be assumed to be unity and the instrumental line broadening 0.

It must be noted that for smaller peaks it can be hard to determine an accurate estimate of the FWHM. The smaller the intensity of a peak, the more likely it is that noise or random errors will affect the values. The viability of the FWHM values have to be evaluated individually and subjectively.

5.5.3 Four Point Probe

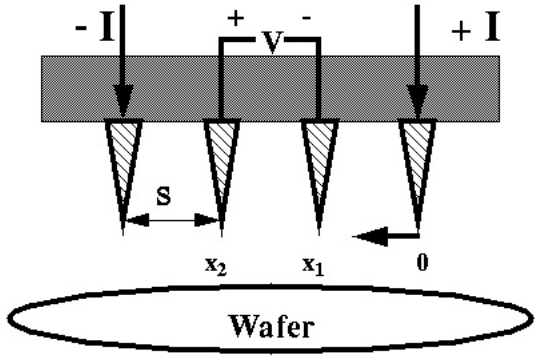

Figure 5.5: Schematic of a Four Point Probe, made by James Chan [79]

The four point probe measures the resistivity of a material by sending a current between the two outer probes, and then measuring the potential difference between the inner two probes. This is done for a series of different currents, which can then be used with ohms law, Eq. 5.5, to calculate the resistance.

$$V = IR \tag{5.5}$$

The resistance can then be used to find the sheet resistivity (R_s), assuming that the sample is fairly thin.

$$R_s = 4.53 \times \frac{V}{I} \tag{5.6}$$

The sheet resistivity can then be multiplied by the total film thickness, d, to find the resistivity in Ω cm, as seen in Eq. 5.7.

$$\rho = R_s \times d \tag{5.7}$$

The thicknesses of the films have been measured using a Profilometer, but due to the lack of uniformity in both the films and the substrate as well as the uncertainty in the device, the thicknesses are only accurate to the 100 nm scale.

5.5.4 Transmission Electron Microscope (TEM)

The crystallite sizes measured by XRD are only representative in the vertical plane. The horizontal crystalline quality of the Cu_2O films is also of interest, as this is the plane that will be in contact with the AZO. TEM has therefore been used on one film, to gain an idea of the horizontal grain size of Cu_2O films produced in this thesis. This is not directly comparable to the vertical crystallite sizes measured, as one grain can contain a number of crystallites due to stacking faults.

TEM is a microscopy method that is commonly used to investigate the structure of material. The method works by transmitting a beam of highly accelerated electrons though a very thin sample. The electrons can be diffracted, cause X-rays to be emitted, emit secondary electrons or simply back-scatter. Adjusting the lens system inside the microscope will allow the operator to choose the desired imaging effect which can then be measured. [80]

In this thesis two bright field images are presented. Such bright field images are formed by placing an aperture into position so that only the electrons that have not been diffracted by the materials are observed. This results in an image formed by brighter areas of the image where electrons have passed through the sample unimpeded, and darker areas where the majority of electrons have been scattered so very few have passed through. The resulting image gives a very good representation of the shapes and sizes of grains in the sample. [80]

TEM measurements in this thesis were made by Emil Christiansen, performed on the Cu_2O film with the largest (111) oriented crystallites determined from XRD called 3O2_30N2_750.

5.5.5 X-ray Photoelectron Spectroscopy

X-ray Photoelectron Spectroscopy, or XPS is a widely used technique used to determine the chemical composition of the surface of materials. The method can be used to determine both the chemical state and the electronic state of elements in the material in the parts per thousand range.

XPS works by irradiating a substance with X-rays and then measuring the number of electrons that are exited, as well as the kinetic energy of these electrons. As the energy of the incoming X-ray photons is known, the electron binding energy, and thus the chemical composition can thus be measured due to conservation of energy. Earnest Rutherford determined that Equation 5.8 could be used to calculate the binding energy. [78]

$$E_{Binding} = h\nu - (E_{Kinetic} + \phi) \tag{5.8}$$

In Eq. 5.8, $E_{Binding}$ is the binding energy of the electrons, $h\nu$ is the energy of the incoming photons, $E_{Kinetic}$ is the measured kinetic energy of the outgoing electrons. The work function ϕ is an instrumental factor, not a material factor.

Since XPS only analyses up to the top 10 nm of the material, it can be useful to use sputter-etching before any measurements are taken to clean off surface contaminants.

All XPS measurements in this thesis were done by PhD Mohammadreza Nematollahi, in the NTNU physics department.

Chapter 6

Experimental Results and Discussion

In this section all experimental results will be presented and discussed. In order to produce the best possible solar cells the material parameters of layers have to be studied first to learn which parameters works best with respect to crystal structure and electrical properties. Once the material parameters of individual layers have been studied and optimal parameters have been determined an attempt will be made to produce full solar cells using the optimal parameters. The I-V curves of these solar cells will then be presented and discussed to determine if the attempt was successful.

The results are divided by layers, first the XRD and resistivity results of AZO are presented Sections 6.1.1 and Section 6.1.2 and then all AZO results are discussed together in Section 6.1.3. Next the XRD results from the undoped ZnO layers are presented and discussed in Section 6.2. Then the Cu_2O results are presented by characterization method and discussed in Section 6.3. First the XRD results are presented in Section 6.3.1, the TEM results are presented in Section 6.3.2, the resistivity results are presented in Section 6.3.3, the XPS results are presented in Section 6.3.4 and finally all of the Cu_2O results are discussed in Section 6.3.5. Once the materials have been studied, the solar cells presented are discussed as a whole. The I-V results taken between the electrodes are presented in Section 6.4.1 and the XPS results taken from the Mo electrode of a completed electrode are presented in Section 6.4.2, then the solar cells are discussed in Section 6.4.3.

6.1 AZO thin films

In order to make the best possible p-Cu_2O/n-AZO junction both of the layers, AZO and Cu_2O, must be optimized. For the AZO layer this means optimizing the crystal structure and the sheet resistivity. As section 3.5.1 shows, it is desirable to deposit AZO mainly in its (002) orientation. Therefore, the crystallinity of AZO films deposited at various temperatures, substrate-target distances and film thickness are investigated in Section 6.1.1. It is also desirable to have as low a resistivity as possible, so the resistivity of the AZO films for the same variables are investigated in Section 6.1.2.

6.1.1 XRD Results

The XRD measurements in this section were done to determine if the substrate-target distance has an effect on the crystalline quality of the AZO films deposited.

Figure 6.1 shows the XRD results measured from three AZO films made with increasing distance between the substrate and target. All three films were made with 20 000 pulses and a substrate temperature of 400 °C. It is possible that increasing the target-substrate distance has decreased the thickness of the films slightly, but the profilometer used to measure the thicknesses is not sensitive enough to detect this. As discussed in Section 5.5.1, each film thickness is rounded to the nearest 100 nm, and for the films made with 20 000 pulses this means all films are considered 100 nm thick.

Analyzing Figure 6.1 shows that the AZO films made at 400° all have peaks at 2θ = 34, 43, 63 and possibly one at 68. Due to the high level of noise the *Bruker* software cannot determine the exact 2θ values of the peak tops or match these tops to theoretical database values, but from the literature it can be determined that the (002), (102) and (103) peaks of ZnO occur at values roughly close to 2θ = 34, 47 and 63 respectively.[32][63][81] The observed peaks and their literature values are listed in Table 6.1.

Figure 6.2 shows the XRD data obtained from three films made at a substrate temperature of 300 °C, with the same three substrate-target distances as the 400 °C films. These three films are also estimated to have the same thickness of 100 nm.

Like the films made at 300 °C the *Bruker* software is unable to determine the exact locations of the peaks due to noise. There are, however, observable peaks at 2θ = 34, 47 and 63 that correspond to the (002), (102) and (103) peaks of ZnO. A list of the observed peaks, their theoretical values and the HKL index is shown in Table 6.1.

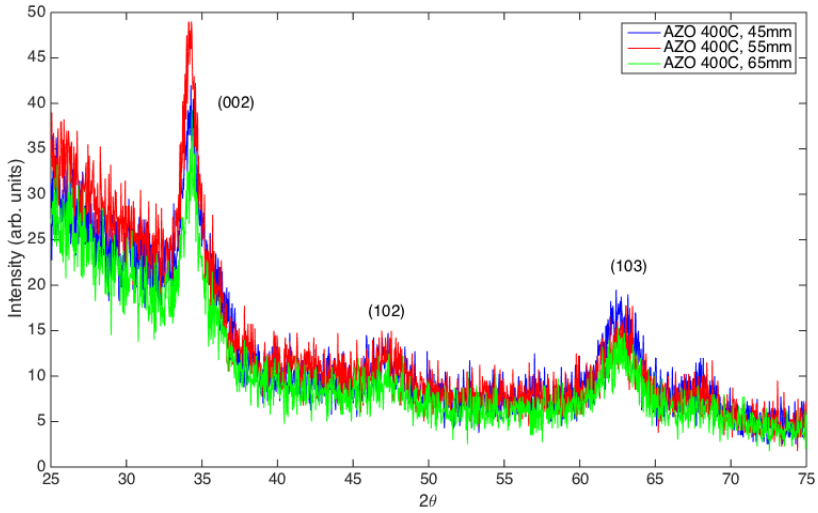

Figure 6.1: XRD data from AZO thin films made at 400°C with differing distances between the substrate and target during deposition. The green data points were taken from the film made at 45 mm from the target, the red were made at 55 mm from the target and the green were made at 65 mm from the target.

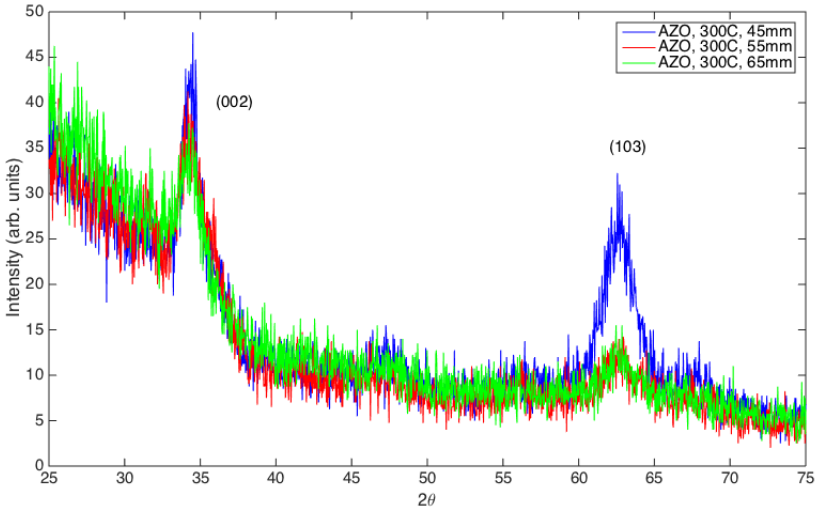

Figure 6.2: XRD data from AZO thin films made at 300°C with differing distances between the substrate and target during deposition. The green data points were taken from the film made at 45 mm from the target, the red were made at 55 mm from the target and the green were made at 65 mm from the target.

Observably it appears as if the films made at 300 °C have slightly smaller (102) peaks. In addition to this the 300 °C film with 45mm as its substrate-target distance appears to have a disproportionally large (103) peak compared to the other five films.

Table 6.1: XRD peaks observed from data taken from AZO films. Literature values obtained from [32][63][81]

Experimental 2θ	Litterature 2θ	HKL
34	34.4	(002)
47	47.5	(102)
63	62.8	(103)

In order to obtain more accurate data on the vital (002) peaks of the ZnO films, additional XRD measurements were made, this time in the 2θ range of 25 - 50 °. The XRD data from these close scans are shown in Figure B.2 and Figure B.1 in Appendix B. This close scan allowed the instrument to spend more time measuring each data point in this region, and decreasing the noise slightly. This XRD data was analyzed to obtain the FWHM and crystallite sizes of the six AZO (002) peaks, shown in Table 6.2.

Table 6.2: Comparing crystallite sizes determined from the (002) peak of AZO films

S-T Distance	Temp.	Peak top, 2θ	FWHM	Crystallite Size (Å)
45 mm	300	34.3	1.2	77
	400	34.2	1.4	66
55 mm	300	34.4	1.7	54
	400	34.2	1.1	84
65 mm	300	34.1	1.4	66
	400	34.3	1.1	84

The (002) peaks in Table 6.2 shows that for the samples with substrate-target distances 55 mm and 65 mm the crystallite size is larger for the samples made at the highest temperature. This trend is not observed for the samples made at the closest substrate-target distance, where the 300 °C sample appears to have a larger (002) peak than the 400 °C sample.

6.1.2 Resistivity Results

The resistivity of all AZO films deposited were measured. The results are shown in Table 6.3. Graphing the results in Table 6.3 gives Figure 6.3, where resistivity is plotted as a

function of substrate-target distance for the two temperatures, and Figure 6.4, where resistivity is plotted as a function of substrate-target distance for the two thicknesses.

Table 6.3: Resistivity of AZO films made at two temperatures and two thicknesses

Substrate	300 °C, 100 nm	400 °C, 100 nm	400 °C, 200 nm
65 mm	2.93 x 10^{-3} Ωcm	3.75 x 10^{-3} Ωcm	1.79 x 10^{-3} Ωcm
55 mm	1.43 x 10^{-3} Ωcm	3.69 x 10^{-3} Ωcm	1.47 x 10^{-3} Ωcm
45 mm	0.59 x 10^{-3} Ωcm	1.82 x 10^{-3} Ωcm	1.25 x 10^{-3} Ωcm

Graphing the resistivity for the two temperatures, seen in Fig. 6.3, shows that for each substrate-target distance the lower temperature gives lower resistivity. For both deposition temperatures the resistivity increases with substrate-target distance. The difference in resistivity between the two substrate temperatures is not so large however, as is demonstrated by the fact that the smallest substrate-target distance (45mm) shows a lower resistivity for the film made at 400 °C than the film made at 300 °C has for the largest substrate-target distance (65 mm).

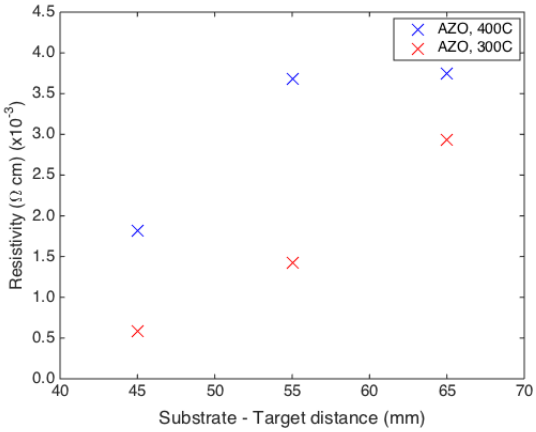

Figure 6.3: Resistivity measurements as a function of substrate-target distance, made at variable deposition temperatures and constant 100 nm thickness. The red data points were measured from a film made at 300°C and the blue data points were measured from a film made at 400°C.

Graphing the resistivity of the three AZO films to compare effect of film thickness, shown in Fig. 6.4, makes it clear that thicker films have lower resistivity. As with the films made at the lower temperature, it is clear that the films made with smaller substrate-target distances are less resistive as well, though the effect is less notable in the thicker films.

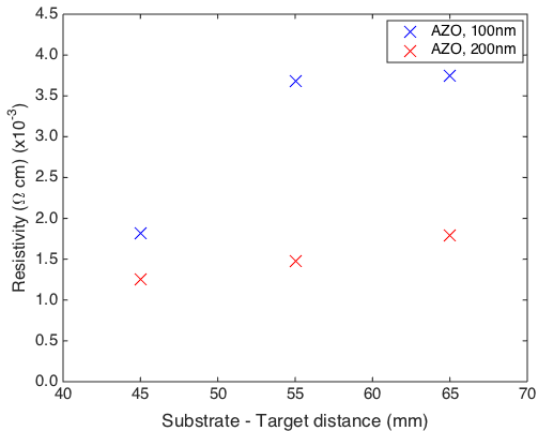

Figure 6.4: Resistivity measurements as a function of substrate-target distance, made at variable film thicknesses and constant 400 °C substrate temperature. The red data points were measured from films that were 200 nm thick, while the blue data points were made from films that were 100 nm thick.

6.1.3 Discussion of AZO results

To determine the temperature and substrate-target distance that will be used during deposition of the films for the junction, both the crystalline structure and the resistivity have to be considered simultaneously.

As has been noted previously, if the AZO is highly aligned in the (002) orientation the Cu_2O will be able to align in the similar way, decreasing the number of interface defects that are likely to occur. It is therefore highly important to attempt to deposit AZO films that are as (002) oriented as possible. Shan et al. [62] suggests that higher temperatures (400 °C or above) are favorable during the deposition process because this yields better alignment of the ZnO in the (002) orientation. The results of crystallite size of the (002) orientation as a function of substrate temperature from the work of Tanaka et al. [68] show a very clear correlation. As the substate temperature is increased from 200 °C to 500 °C the crystallite size increases from about 25 nm to almost 40 nm.

The results shown in Table 6.1 may agree with the results of Shan et al. and Tanaka et al. if not by a large margin. The films deposited at 400 °C have a larger (002) oriented crystallite than the films deposited at 300 °C at two out of the three substrate-target distances. The crystallite sizes measured at the smallest substrate-target distance of 45 mm show that the lower substrate temperature produced a slightly larger (002) crystallite size, which contradict both Shan et al. and Tanaka et al. This may be an anomaly or

an indication that something else has happened during deposition, it would be impossible to know without further investigating a wider range of parameters. To determine if the crystallite sizes at the substrate-target distance of 45 mm is an indication of a trend, a larger substrate temperature range such as 200 °C and 500 °C as well as considering the substrate-target distance of 35 mm may need to be investigated. However, for the purposes of this thesis, the optimal parameters for depositing large (002) crystallite size are substrate temperature of 400 °C with either a substrate-target distance of 55 mm or 65 mm.

Notably, it is unexpected that the 300 °C, 45 mm film has a disproportionately large (103) oriented peak. The same peak size increase is not shown in the 45 mm film made at 400 °C, so there is no distinct trend for films made with small substrate-target distances. It might be necessary to repeat the deposition and measurement of this film to confirm this data. Nevertheless this does suggest that the combination of 300 °C substrate temperature and 45 mm substrate-target distance would be the least ideal for the purposes of this thesis.

Figure 6.3 clearly shows that a lower temperature gives slightly lower resistivity, for each individual substrate-target distance. This contradicts the results of Cho et al. [64] and Park et al. [67] whose results show that higher deposition temperatures give lower resistivities. Both Cho et al., who studied undoped ZnO, and Park et al., who studied AZO, deposited their films by sputtering, not by PLD as was done in this thesis, and this could account for the difference. Unlike Park and Cho et al. Tanaka et al. [68] deposited AZO by PLD and they found that the lowest possible resistivity was achieved at 300 °, and that increasing the substrate temperature to 400 °C or 500 °C, or decreasing to 200 °C would all increase the resistivity. Tanaka et al. also found that carrier concentration was the highest at 300 °C. The increase in resistivity and decrease in carrier concentration at substrate temperatures larger or smaller than 300 °C was attributed by Tanaka et al. to an increase in oxygen content in the films. Since they found that films deposited with higher substrate temperatures had a higher percentage of oxygen atoms to each zinc atom, they suggested that this would decrease the concentration of native donors. Tanaka et al. found that they were able to counteract this oxidation and depletion of native donors by depositing the films with a suppressing H_2 atmosphere that prevented increased oxidation at higher temperatures. In these H_2 atmosphere experiments it was found that increased substrate temperatures decreased the resistivity as is seen in films deposited by sputtering.

The resistivity of the films can also be seen to increase as a function of the substrate-

target distance as can be seen from both Fig. 6.3 and Fig. 6.4. Tanaka et al. [68] found that the optimal substrate-target distance for depositing low resistivity AZO was 30 mm. This thesis does not attempt to deposit at substrate-target distances that small, but it is evident that the substrate-target distances that approach the 30 mm distance that Tanaka et al. found have lower resistivities than the larger distances.

The decision on what parameters to use during AZO deposition for the final junction came down to a compromise between crystallinity and resistivity. The optimal settings for increased crystal growth in the (002) direction appears to be 400 °C with either 55 mm or 65 mm as the substrate-target distance. Of these two films the one produced at 55 mm has the lower resistivity. The films produced at the higher substrate temperature will, as demonstrated, produce films with slightly higher resistivities. However, the biggest detriment to a successful junction is often mismatch or defects at the interface, and these will be reduced the most by maximizing the crystal structure at the cost of the resistivity. It should also be considered that the differences in the resistivities for both temperatures and thicknesses are not very large, only on the order of 1 x 10^{-4} Ω cm.

Thus, the parameters used in deposition of AZO thin films for the solar cell assembly will be a substrate temperature of 400 °C and a substrate-target distance of 55 mm, to maximize the crystallite size of the (002) orientation. Additionally the films will be produced by 20 000 pulses, to produce 100 nm thick films, as the thinner films are almost as conductive as the thicker films and they will be slightly more transparent as well as take shorter time to deposit.

6.2 ZnO films

Figure 6.5 shows an XRD measurement of three 200 nm thick samples. The first one is an undoped ZnO film, the second one consists of 100 nm of undoped ZnO grown on top of 100 nm of AZO, and the last is 200 nm of pure AZO.

The purpose of these XRD measurements was to determine if the undoped ZnO films deposited from a constructed Zn target made from a melted Zn sheet would be able to function adequately. The undoped ZnO is to be used as a buffer layer in an AZO/Cu_2O heterojunction, and thus needeeds to grow structurally similar to the commercially purchased AZO target. The results clearly show that the self constructed Zn target deposits films that are structurally fairly similar to the films deposited by the commercial target. All three samples strongly display the (002) peak, this peak being dominant for the com-

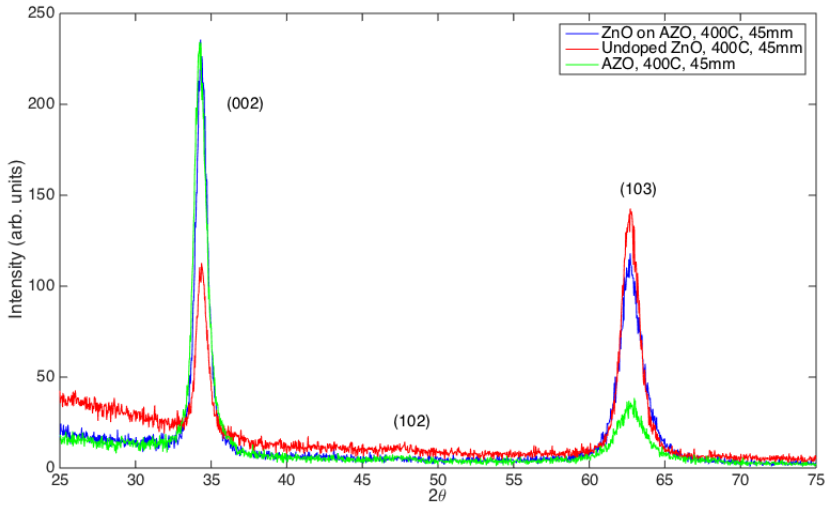

Figure 6.5: XRD results of an 100nm undoped ZnO thin film grown on glass (red), 100nm undoped ZnO film grown on 100nm of AZO (blue) and 200nm of AZO (Green)

Table 6.4: Peaks for ZnO on AZO data in Fig 6.5

(*hkl*)	Sample	2θ	Theoretical 2θ	FWHM	Crystallite Size
(002)	ZnO on AZO	34.357	34.379	0.882	104.8 Å
	Undoped ZnO	34.368	34.419	0.826	111.9 Å
	AZO	34.255	34.422	0.966	95.6 Å
(102)	ZnO on AZO	-	-	-	-
	Undoped ZnO	-	47.536	-	-
	AZO	-	-	-	-
(103)	ZnO on AZO	62.680	62.777	1.523	67.9 Å
	Undoped ZnO	62.710	62.875	1.317	78.5 Å
	AZO	62.851	62.864	1.587	65.2 Å

mercial AZO and the constructed ZnO deposited onto a layer of AZO. The constructed ZnO by itself.

6.2.1 Discussion of ZnO Results

All three of the samples display two visible peaks at $2\theta \simeq 34$ and $2\theta \simeq 63$ corresponding to the (002) and (103) peaks of ZnO.[32][63][81] Both of these peaks are wurtzite (hexagonal) which is ideal for this particular heterojunction. A notable difference between the three films is that the undoped ZnO film has a slight peak at $2\theta = 47.5$, corresponding to

the (102) peak of ZnO. This peak is, however, not visible when the ZnO is grown on top of AZO, as it will be when the heterojunction is constructed. The intensity of the (103) peak in the ZnO on AZO sample appears to have a much higher intensity than that of the AZO sample, but the FWHM which is used to calculate the crystallite size suggests that the (103) crystallite size is actually not that much larger for the ZnO on AZO sample than it is for the AZO sample as Table 6.1 shows.

In addition to this the crystallite size for the (002) peaks of the ZnO on AZO and the AZO samples are comparable in size, being 104.8 Åand 111.9 Årespectively. This is better than the simple ZnO sample whose (002) peak is 95 Å. This suggests that growing the ZnO on top of the AZO helps arrange the ZnO into the crystal structure of the substrate, into the (002) direction as is desired.

Figure 6.5 therefore conclusively demonstrates that the constructed Zn target functions sufficiently well enough to deposit an undoped ZnO buffer layer in a AZO/ZnO/Cu_2O heterojunction.

6.3 Cu_2O Films

To make the best possible ZnO/Cu_2O junction, one of the most important things to do is to optimize the Cu_2O layer. For this purpose a number of Cu_2O thin films have been deposited on glass substrates under various conditions, as described in Section 5.1.2. Grazing Incidence XRD measurements were made on all films, in order to attempt to determine which deposition parameters that will maximize growth in the (111) orientation. These results are shown in Section 6.3.1. To determine the order of magnitude of the planar grains in the Cu_2O films, a TEM image was taken from one of the films with the largest (111) crystallite. XPS measurements were done on some films, to test for Nitrogen content as well as to check the phase of the copper. XPS results from Cu_2O films are shown in Section 6.3.4. Finally, for each of the thin films, resistivity measurements were made. Cu_2O films with lower resistivities are more likely to conduct mobile charge out of the junction without recombining, so this is a vital characteristic to control. The resistivity results are shown in Section 6.3.3.

6.3.1 Cu_2O XRD

Grazing Incidence XRD measurements were taken of all Cu_2O films made, and the results of those measurements are shown in this section. The Grazing Incidence XRD method is explained in Section 5.5.2. For each XRD result the peaks detected were

matched through the *Bruker* database of elements to theoretical models both for Cu_2O and CuO. If peaks existed that could not be attributed to the two oxidized states, the data was also matched to a model of unoxidized metallic Cu. The peak data was then analyzed to find the FWHM of all peaks distinct enough for this to be determined. This information was then used to calculate the crystallite sizes of the orientations corresponding to the peaks with the Scherrer equation described in Section 5.5.2.

Figure 6.6 shows the XRD measurements taken from the series of Cu_2O films made by PLD at 750 °C with varying levels of oxygen and nitrogen and no sputtering.

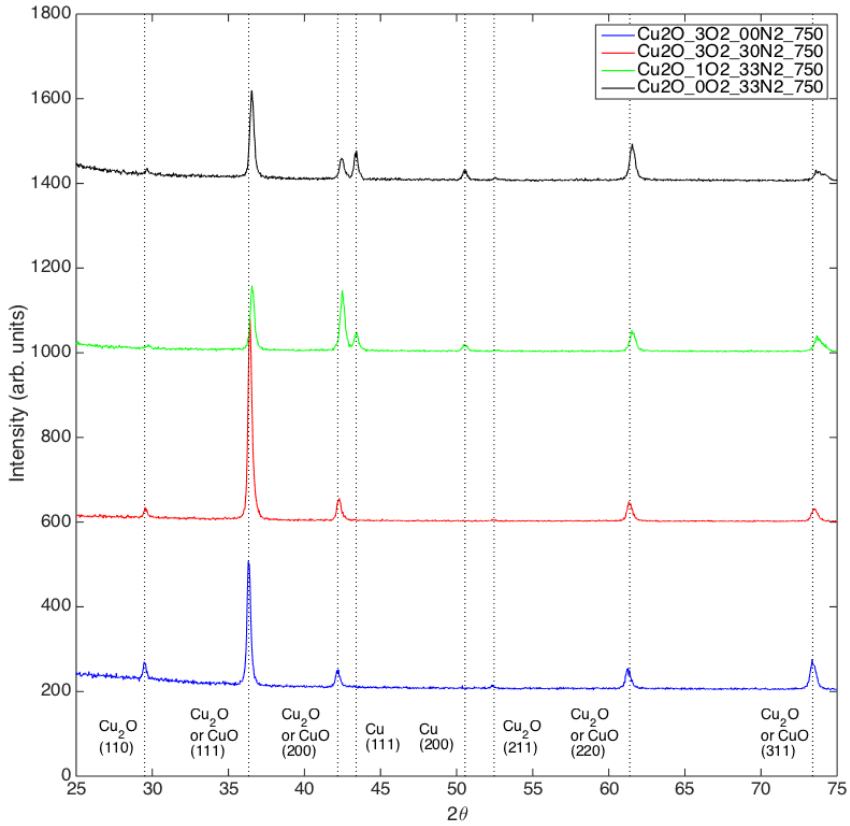

Figure 6.6: XRD measurements made from the four Cu_2O films that were made at 750 °C with no sputtering. Dotted lines indicate peak positions of the Cu2O-3O2-00N2-750

The literature, as explained in section 3.5.2, suggests that even though the target is composed only of Cu_2O the deposited sample will contain some CuO and Cu unless oxygen

pressure in the chamber falls within the right parametrs. Therefore the first film deposited, the Cu_2O_3O2_00N2_750 film seen in Fig. 6.6, was produced with 3 sccms of O_2 injected into the chamber during deposition, making the chamber pressure 1.3 x 10^{-3} Torr. A detailed summary of the peaks detected in this film can be seen in Table 6.5.

Table 6.5: Peaks detected from Cu2O_3O2_00N2_750 XRD data seen in Fig. 6.6. The data was taken from a 200 nm thick Cu_2O film made at 750 °C with 3 sccm of O_2 in the chamber.

2θ	2θ Cu_2O (*hkl*)	2θ CuO (*hkl*)	FWHM	Crystallite Size (Å)
29.505	29.672 (110)	-	0.3	304
36.347	36.428 (111)	36.637 (111)	0.227	335.8
42.191	42.314 (200)	42.559 (200)	0.33	286.7
52.363	52.468 (211)	-	-	-
61.264	61.384 (220)	61.761 (220)	0.38	269.9
73.416	73.582 (311)	74.003 (311)	0.46	239.3

The possible theoretical CuO peaks are shown in the table as they are reasonably close to the detected peak values. However, the detected peaks are far closer to the theoretical database values Cu_2O peaks in all cases. It is therefore likely that this film is made purely of Cu_2O, and that it is highly dominated by the (111) orientation.

The second series of data seen in Fig. 6.6, named Cu2O_3O2_20N2_750, was an attempt to make an IB material by directly doping the Cu_2O. For this purpose 30 sccm of N_2 gas was introduced during deposition, in addition to the original 3 sccm of O_2. Table 5.1, the pressure in the chamber during this deposition was 3.6 x 10^{-3} Torr. Compared to the first film, this one demonstrates a much more intense (111) peak, and all the other peaks appear to be slightly smaller. The (211) Cu_2O peak detected in the first film at 2θ = 52.363 cannot even be seen in this film. A detailed summary of the peaks detected, their FWHM and their crystallite sizes can be found in Table 6.6. From the table it can be seen that the calculated crystallite sizes are far larger for the (110) and the (111) peaks than any of the others, The dominant peak is clearly the one corresponding to the (111) orientation. Whilst the XRD cannot determine wether or not the Cu_2O has been successfully doped with nitrogen, it does appear that the increased chamber pressure has increased the crystalline quality of the film.

Like with the 3O2_00N2_750 film, the CuO database values are included in the table because they are reasonably close to the measured peak values. As with the previous film,

Table 6.6: Peaks detected from XRD data from the Cu2O_3O2_30N2_750 data seen in Fig. 6.6. The data was taken from a 200 nm CU_2O thin film deposited with 30 sccm N_2 and 3 sccm O_2 in the chamber, with the substrate at 750 °C.

2θ	2θ Cu_2O (*hkl*)	2θ CuO (*hkl*)	FWHM	Crystallite Size (Å)
29.562	29.572 (110)	-	0.4	228
36.426	36.428 (111)	36.637 (111)	0.297	313.2
42.273	42.314 (200)	42.559 (200)	0.33	286.8
52.363	52.468 (211)	-	-	-
61.366	61.384 (220)	61.761 (220)	0.4	256
73.520	73.528 (311)	74.003 (311)	0.5	220

however, the database values for the Cu_2O peaks are all closer to the measured peaks than the CuO database peaks. There is little indication of a double peak, so as before it is reasonable to assume that the film is made purely of Cu_2O.

The third XRD result shown in Fig. 6.6 is called Cu2O_1O2_33N2_750. Under the deposition of this film, with the goal of producing an IB material, it was attempted to further decrease the oxygen flow in the chamber to 1 sccm whilst increasing the nitrogen flow to 33 sccm. This was done because oxygen is a highly reactive material and reducing the oxygen content whilst increasing the nitrogen content would increase the probability of nitrogen substitution taking place during crystal production. It can clearly be seen that whilst the total pressure in the chamber is still reasonably high, 3.6 x 10 $^{-3}$ Torr, the oxygen pressure is too low to produce a thin film without producing some peaks that cannot be attributed to Cu_2O, and can therefore only be metallic Cu. As can be seen in the summary of peaks in Table 6.7, both the (200) oriented peak from Cu_2O or CuO and the (111) oriented peak from the Cu are large both in intensity and crystallite size, meaning that the more desired (111) form the Cu_2O will be less dominant. There is also a fairly significantly sized (200) oriented Cu peak, so the two Cu peaks have crystallite sizes 338.1 Å and 293 Å , one larger than and the other almost as large as the 302.3 Å sized (111) Cu_2O crystallite.

Unlike the two first films, in this one it is more ambiguous if the peaks are attributed to Cu_2O or CuO. The measured peaks all fall somewhere between the database values for Cu_2O and CuO. It may be that there is some percentage of CuO in the films as well as Cu_2O.

The last Cu_2O thin film XRD shown in Fig. 6.6 was made with no O_2 in the chamber in an attempt to see if the Cu_2O material deposited from the target could become doped

Table 6.7: Peaks detected from XRD data called Cu2O_1O2_33N2_750 seen in Fig. 6.6. It was taken from a a 200 nm thick Cu_2O film made at 750 °C with 1 sccm of O_2 and 33 sccm of N_2 in the chamber.

2θ	$2\theta Cu_2O$ (*hkl*)	2θCuO (*hkl*)	2θCuO (*hkl*)	FWHM	C.S. (Å)
29.727	29.572 (110)	-	-	-	-
36.575	36.428 (111)	36.637 (111)	-	0.315	294.9
42.498	42.314 (200)	42.554 (200)	-	0.341	277.8
43.400	-	-	43.473 (111)	-	-
50.554	-	-	50.674 (200)	-	-
61.570	61.384 (220)	61.761 (220)	-	0.42	245.0
73.721	73.528 (311)	74.003 (311)	74.679 (220)	0.52	212.1

with some N_2 without the reactive oxygen present in the chamber. The thin film was thus produced with 0 sccm of O_2 and 33 sccm of N_2, the chamber pressure was 3.7 x 10^{-3} Torr. The XRD results taken from this thin films are shown as 0O2_33N2_750 in Fig. 6.7, and the peaks with the information extracted from them are shown in Table 6.8. From the graph it can be observed that removing the oxygen present in the chamber during deposition has vastly increased the production of metallic copper in the film. The (111) oriented Cu peak is now larger than the (200) oriented CuO/Cu_2O peak that has in all other films been larger. Table 6.8 confirms this, the copper (111) orientation has a crystallite size of 355.6 Å while the (200) CuO/Cu_2O orientation is only at 297.9 Å. The (200) copper orientation also has a large crystallite size with 344.7 Å. Both of these Cu crystallites are thus larger than the (111) oriented CuO/Cu_2O crystallite, indicating that metallic copper rather than the oxidized versions dominates in this film.

Table 6.8: Peaks detected from the XRD data called Cu2O_0O2_33N2_750 seen in Fig. 6.6. The data was taken from a 200nm thick Cu_2O film made at 750 °C with 0 sccm of O_2 and 33 sccm of N_2 in the chamber during deposition.

2θ	$2\theta Cu_2O$ (*hkl*)	2θCuO (*hkl*)	2θCu (*hkl*)	FWHM	C.S. (Å)
29.645	29.572 (110)	-	-	-	-
35.550	36.428 (111)	36.637 (111)	-	0.308	302.3
42.458	42.314 (200)	42.559 (200)	-	0.318	297.9
43.386	-	-	43.473 (111)	-	-
50.542	-	-	50.674 (200)	-	-
52.540	52.468 (211)	-	-	-	-
61.552	61.384 (220)	61.761 (220)	-	0.42	244.6
73.734	73.258 (311)	-	-	-	-
74.128	-	74.003 (311)	74.679 (220)	-	-

As with the 1O2_33N2_750 film, the measured peaks in 0O2_33N2_750 fall somewhere between the database values for Cu_2O and CuO. It could be that the peaks represent some combination of the two materials.
From Fig. 6.6 it appears that the (111), (200), (220) and (311) peaks that could be either CuO or Cu_2O shift slightly towards the right as the oxygen content is lowered. As can be seen from tables 6.5, 6.6, 6.7 and 6.8 it can be seen that the theoretical 2θ values for CuO are all slightly larger than those for Cu_2O. Additionally the (110) and (211) peaks that correspond only to Cu_2O become smaller as the oxygen is reduced. While not conclusive, considering that the peaks probably consist of a combination of CuO and Cu_2O, this indicates that the films made with more oxygen in the tank have more Cu_2O than the films made with less oxygen. This apparent increase of CuO with decreased oxygen pressure contradicts the findings of Rakhsani et al. [60], shown in Fig. B.3, which suggests that it might be erroneous to conclude that the peak shift is an indication of CuO and more that it is an instrument error in the XRD equipment.

Figure 6.7 shows XRD measurements made from the four slightly more novel Cu_2O films that were produced. The first film that can be seen is the same as the first film seen in Fig. 6.6 for reference, so that comparisons between the two graphs can be made.

The first novel set of films made were two where chromium sputtering was introduced during PLD of Cu_2O. This was done with the intention that the sputtered Cr atoms would hit the inert N_2 molecules and split them up into more reactive nitrogen atoms that have a higher probability of reacting and integrating with the crystal lattice. This idea stemmed from the successful nitrogen doping of Cu_2O by Malerba et al. [26] and Nakano et al. [84] which were both completed during sputtering processes.

The first chromium sputtered film shown in Fig. 6.7, called Cu2O_2O2_30N2_5Ar_750, was made with 2 sccm of O_2 and 30 sccm of N_2 in the chamber during deposition. In addition to this the sputtering process required 5 sccm of Ar to produce sputtered Cr atoms. The peaks detected from this sample and their theoretical matches from the database are summarized in Table 6.9. As is clearly shown the visible peaks correspond to the same crystallographic orientations as seen in previous films. There are some notable differences, such as that the (211) orientation is not visible in the noise, and that the (110) is much harder to discern and as such no useful FWHM estimation or crystallite size calculation is possible. Just from glancing at the graph it is clearly observable that the (111) orientation is less dominating than in the Cu2O_3O2_00N2_750 film as well as most of the films shown in Fig 6.6. This is confirmed from looking at the crystallite sizes in the table. The four measurable peaks comparative crystallite sizes 299.5

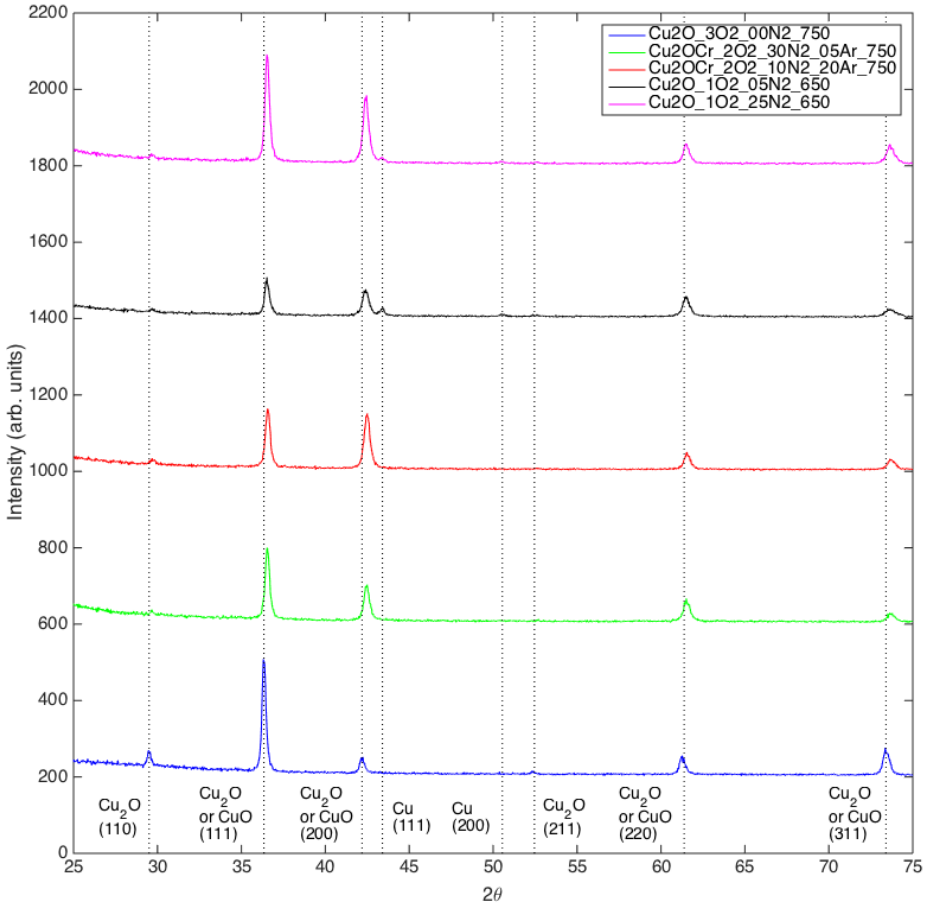

Figure 6.7: XRD measurements made from the two Cu_2O films that were made with sputtering at 750 °C, the two films made at 650 °C and the film made with 3 sccm of O_2 with no nitrogen that can also be seen in Fig. 6.6 for comparison

Å, 257 Å, 241.5 Å and 240.9 Å. The (200) and (220) orientations have both grow in size compared to the (111) orientation, and as observed from the graph, the (111) orientation is far less dominating than it has been in earlier films.

The second chromium sputtered film shown in Fig. 6.7, called Cu2OCr_2O2_10N2_20Ar, was made with 2 sccm of O_2 and 10 N_2. Here the N_2 concentration was at a slightly lower 10 sccm and the Ar supply was increased to 20 sccm both to ignite the plasma and to keep the chamber pressure roughly similar to the first sputtering attempt. The peaks detected by XRD can be seen in Table 6.10 and are fairly similar to the other sputtering attempt. The decrease in N_2 pressure appears to have further encouraged growth of the

Table 6.9: Peaks detected from the XRD data called Cu2OCr_2O2_30N2_5Ar in Fig. 6.7. The data was taken from a 100 nm thick Cu_2O film made at 750 °C with 2 sccm of O_2, 30 sccm of N_2 and 5 sccm of Ar in the chamber

2θ	$2\theta Cu_2O$ (hkl)	2θCuO (hkl)	FWHM	Crystallite Size (Å)
29.672	29.757 (110)	-	-	-
36.549	36.650 (111)	36.637 (111)	0.372	299.5
42.462	42.612 (200)	42.559 (200)	0.369	256.6
61.534	61.345 (220)	61.761 (220)	0.425	241.5
73.694	73.997 (311)	74.003 (311)	0.46	239.8

(200) orientation. The summary of information extracted from the peaks can be seen in Table 6.10. The deviation between the crystallographic orientations appears to be very small, as all crystallite sizes are on the order of 200 Å . It seems that lowering the nitrogen concentration in the vacuum chamber has further degraded the monocrystallinity of the thin film even though the overall pressure is not too changed.

Table 6.10: Peaks detected from the XRD data called Cu2OCr_2O2_10N2_20Ar in Fig. 6.7. The data was taken from a 100 nm thick Cu_2O film made at 750 °C with 2 sccm of O_2, 10 sccm of N_2 and 2 sccm of Ar in the chamber.

2θ	$2\theta Cu_2O$ (hkl)	2θCuO (hkl)	FWHM	Crystallite Size (Å)
29.709	29.572 (110)	-	-	-
36.574	36.428 (111)	36.637 (111)	0.336	276.6
42.489	42.314 (200)	42.559 (200)	0.383	247.3
61.560	61.384 (220)	61.761 (220)	0.414	248.3
73.714	73.528 (311)	74.003 (311)	0.54	204.3

Also seen in Fig. 6.7 is a second pair of novel Cu_2O films made at a slightly lower temperature, 650 °C. This was done in an attempt to decrease the necessary time for heating and cooling the substrate as well as decreasing the amount oxygen and nitrogen neccesary to avoid producing metallic copper in the films.

The result of the first such film produced at the lower temperature, which was made with 1 sccm of O_2 and 5 sccm of N_2, can be seen in Fig. 6.7 with the name Cu2O_1O2_05N2. There are 5 clearly visible peaks, and three more smaller ones detected by the *Bruker* software. There are at least two peaks that cannot be attributed to CuO or Cu_2O, so the data also needed to be matched to cubic metallic copper to account for all peaks. In addition, the CuO/Cu_2O (311) peak is widened to such an extent that there is possibly

a (220) oriented Cu peak inside of it. The (111) peak does still appear to be the largest crystallite, but the (200) peak is very nearly the same size. The summary of the peaks detected and their associated crystallite sizes can be seen in Table 6.11.

Table 6.11: Peaks detected from the XRD data called Cu2O_1O2_05N2 in Fig. 6.7. The data was taken from a 200 nm thick Cu_2O film made at 650 °C with 1 sccm of O_2, 5 sccm of N_2 in the chamber.

2θ	$2\theta Cu_2O$ (*hkl*)	2θCuO (*hkl*)	2θCu (*hkl*)	FWHM	Crystallite Size (Å)
29.622	29.572 (110)	-	-	-	-
36.543	36.428 (111)	36.637 (111)	-	0.330	281.7
42.407	42.314 (200)	42.559 (200)	-	0.441	214.5
43.324	-	-	43.473 (111)	-	-
50.547	-	-	50.375 (200)	-	-
52.570	52.468 (211)	-	-	-	-
61.508	61.384 (220)	61.761 (220)	-	0.48	213.9
73.655	73.528 (311)	74.003 (311)	73.997 (220)	0.7	157

The second film deposited at the lower substrate temperature of 650 °C was made with a higher N_2 flow in the tank, 25 sccm. The XRD data taken from this film can be seen in Fig. 6.7 under the name Cu2O_1O2_25N2_650. Increasing the nitrogen content once more has the effect of reducing both the noise and the intensity of all peaks other than that of the peak corresponding to the (111) orientation. Clearly both Cu peaks have become smaller, relative to the Cu2O_1O2_05N2_650 film, with the introduction of additional nitrogen. The detected peak positions, theoretical values for Cu_2O, CuO and Cu as well as the FWHM and crystallite sizes for all peaks are summarized in Table 6.12. The sizes of all Cu peaks are either too small to be able to measure the FWHM and thus calculate the crystallite size, or too small for the FWHM to be reliable. Nevertheless there is still some Cu present in the thin film. In addition to this the (110), (211) and (220) all appear to be less dominant than in the low temperature film with less N_2.

The data displayed in Fig. 6.7 shows that, as in Fig. 6.6, the peaks from all four films are shifted slightly to the right of the peaks detected from the reference film, Cu2O_3O2_00N2_750. This may indicate that there is some CuO present in films made with lower oxygen content, since the theoretical 2θ values of cubic CuO are slightly larger than those from Cu_2O. However, as before this still contradicts the findings of Rakhsani et al. [60] relating phase stability of copper and its oxides to temperature and oxygen pressure. All films were well within the temperature and oxygen pressure band shown in Fig. B.3 and

Table 6.12: Peaks detected from the XRD data called Cu2O_1O2_25N2 in Fig. 6.7. The data was taken from a 200 nm thick Cu_2O film made at 650 °C with 1 sccm of O_2, 25 sccm of N_2 in the chamber.

2θ	$2\theta Cu_2O$ (hkl)	2θCuO (hkl)	2θCu (hkl)	FWHM	Crystallite Size (Å)
29.653	29.572 (110)	-	-	-	-
36.546	36.428 (111)	36.637 (111)	-	0.372	295.5
42.426	42.314 (200)	42.559 (200)	-	0.364	260.3
43.416	-	-	43.473 (111)	-	-
50.559	-	-	50.375 (200)	-	-
52.569	52.468 (211)	-	-	-	-
61.514	61.384 (220)	61.761 (220)	-	0.39	263.3
73.665	73.528 (311)	74.003 (311)	73.997 (220)	0.55	200.5

as such are likely to consist of Cu_2O rather than CuO.

6.3.2 TEM

In order to determine order of magnitude of the planar grain sizes, one TEM image was taken from the most mono crystalline Cu_2O film, the Cu2O_3O2_30N2_750. This was done in order to determine is the crystallite sizes measured in the bulk of the material were representative of the crystal structure in the volume of the thin films. It must be noted that one grain, as can be imaged by TEM, can contain more than one crystallite as there can be stacking faults that separate crystallites of the same orientation whilst they remain the same grain.

Figure 6.8 shows one image taken at 60 thousand magnification, and Fig. 6.9 part of the same image is shown under 150 thousand magnification. The grains shown in Fig. 6.9 can be found crossing the red line on the right side of the circle in Fig. 6.8.

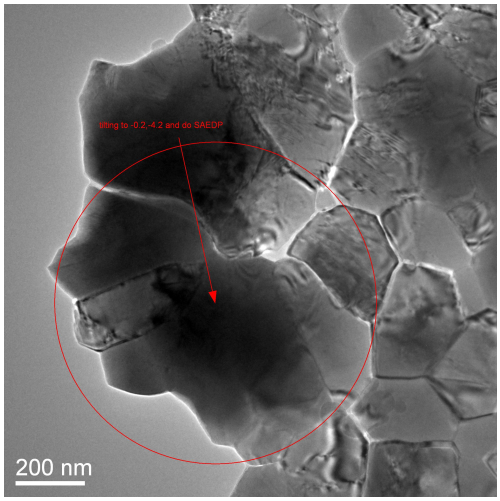

Figure 6.8: TEM image of the CU2O_3O2_30N2 film. It is magnified 60 thousand times.

From the image that has been magnified 60 thousand times, a couple of grains are clearly visible, and it appears that they are hexagonal in shape. The image taken at 150 thousand magnification shows two large grains, and they both appear to be roughly 400 nm across. As can be seen from Fig. 6.8 some grains may be slightly smaller, but they do appear to be within the same order of magnitude.

The grain sizes shown by the TEM images are larger than the crystallite sizes calculated for the same film, seen in Table 6.5, by an order of 10. This suggests that there are stacking faults, subgrains, or surface defects within the grains,[82] though it is not an

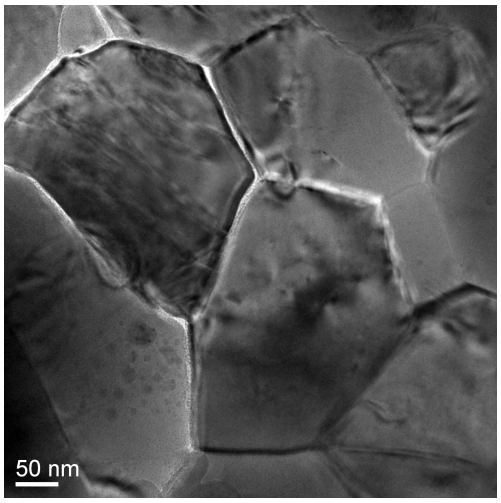

Figure 6.9: TEM image of the CU2O_3O2_30N2 film. It is magnified 150 thousand times.

absolute indication since the grains displayed here are planar whilst the crystallite sizes measured were perpendicular to the substrate. It should also be noted that 400 nm grain sizes is a fairly decent result, whilst the film is not mono crystalline by any stretch, the crystalline quality is still reasonable for an attempted solar cell design.

6.3.3 Resistivity

The resistivities of the Cu_2O films were measured by four point probe, and calculated as shown in Section 5.5.3. The results of those measurements are shown in Table 6.13 descending from the film with the lowest resistivity to the one with the highest.

Table 6.13: Resistivities of Cu_2O Films, ranked by resistivity from lowest to highest

Resistivity (Ω cm)	Deposition temp	Chamber Pressure (Torr)	O_2 (sccm)	N_2 (sccm)	Ar (sccm)
93.0	750 °C	3.6×10^{-3}	3	30	-
217.1	750 °C	1.3×10^{-3}	3	0	-
1283.8	750 °C	3.7×10^{-3}	0	33	-
1314.0	750 °C	6.0×10^{-3}	2	10	20
1763.3	750 °C	9.1×10^{-3}	2	30	5
6016.1	750 °C	3.6×10^{-3}	1	33	-
8881.7	650 °C	6.8×10^{-3}	1	25	-
10877.6	650 °C	1.9×10^{-3}	1	5	-

The table demonstrates that films made with higher oxygen content are generally less

resistive than those with low oxygen content. The only exception to this rule is the film made with no oxygen, but which in turn had a very high nitrogen flow and so a high chamber pressure. It is clearly not only chamber pressure that determines the resistivity, as the 1O2_33N2_750 film and the 3O2_30N2_750 films have almost the exact same chamber pressure, but the film with lower oxygen content is far more resistive than the film with 3 sccm of O2.

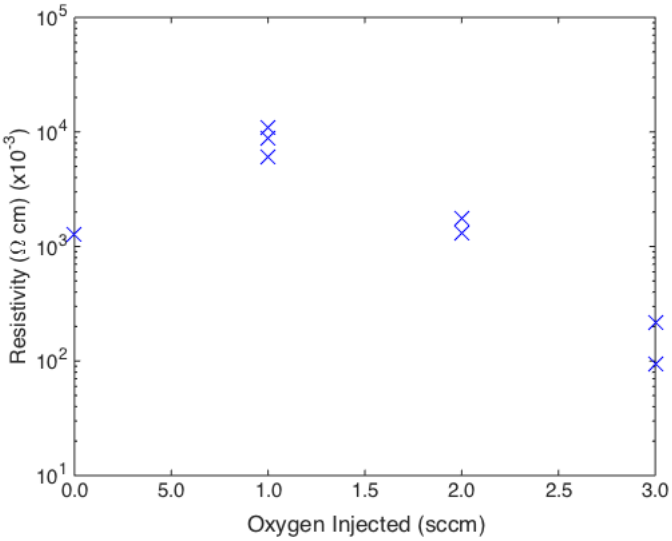

Figure 6.10: A semilogarithmic plot, showing the resistivity of the Cu_2O films as a function of the oxygen content present under deposition

It is also appears that films produced with higher nitrogen flow also are less resistive than those produced with lower nitrogen flow. This is true for the 3O2_30N2_750 which is more conductive than the 3O2_00N2_750 film and for the 1O2_25N2_650 film which is more conductive than the 1O2_05N2_650 film. In both of these cases all deposition parameters except for nitrogen flow are constant, so it is clear that increasing the nitrogen flow has had some effect on resistivity. This is not, however, a completely conclusive sign that the films have been successfully doped as increasing the nitrogen flow also increased the chamber pressure during deposition. A reverse of this decrease in resistivity with increased nitrogen flow was observed in the two chromium sputtered films. That is, for these two films the 2O2_10N2_20Ar film is less resistive than the 2O2_30N2_5Ar film. Notably, the more resistive 2O2_30N2_5Ar film had an overall lower chamber pressure during deposition, 6.8 x 10^{-3} Torr, than the more conductive 2O2_10N2_20Ar

which was deposited at 9.1 x 10^{-3} Torr. In these two films the argon flow parameter was also changed, and it could be that this change in pressure has also had some effect on decreasing resistivity.

There are clearly many factors affecting the resistivity of the Cu_2O films produced in this thesis, and oxygen flow clearly has a large impact. The size of the (111) oriented crystallite size may also appear to have some effect on the resistivity. Figure 6.11 shows the resistivity of the Cu_2O films graphed as a function of the crystallite size of the (111) orientation, and Table 6.14 lists the films by crystallite size so that data points in Fig. 6.11 can be identified.

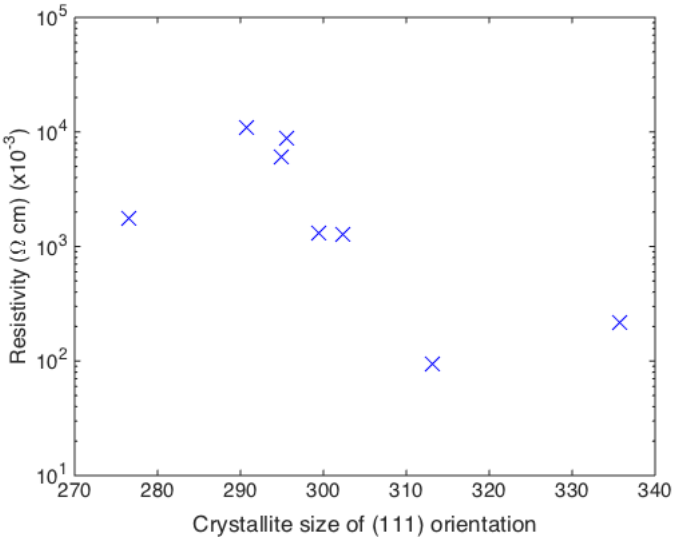

Figure 6.11: A semilogarithmic plot, showing the resistivity of the Cu_2O films as a function of the crystallite size corresponding to the (111) orientation

There appears to be a slight trend that films with smaller (111) crystallites are more resistive. The exceptions to this trend is the film with the largest (111) crystallite, which was made with no nitrogen flow, and the film with the chromium sputtered film with the smallest (111) crystallite. Whilst there are clearly other factors that effect the resistivity of the Cu_2O films, it appears that generally films with larger (111) crystallites are more conductive.

Table 6.14: Reference table for Fig. 6.11. Lists the Cu_2O films and their resistivities, from largest (111) oriented crystallite size to smallest, so that data points in figure can be identified by their films.

(111) Oriented Crystallite Size (Å)	Resistivity (Ω cm)	Cu_2O film
335.8	217.1	3O2_00N2_750
313.2	93.0	3O2_30N2_750
302.3	1283.8	0O2_33N2_750
299.5	1763.3	2O2_30N2_5Ar_750
295.5	8881.7	1O2_25N2_650
294.9	6016.1	1O2_33N2_750
281.7	10877.6	1O2_05N2_650
276.6	1314.0	2O2_10N2_20Ar_750

6.3.4 XPS

To check if having nitrogen present during deposition of Cu_2O was enough to successfully dope the thin films, XPS measurements were done by Mohammadreza Nematollahi on selected films. The films selected were those that were most likely to have been successfully doped due to a high nitrogen flow in the chamber with respect to the oxygen flow. Films Cu2O_1O2_33N2_750 and Cu_2O_0O2_33N2_750 were tested in detail and shown here. The film called Cu2OCr_2O2_30N2_750 was also tested for nitrogen, and Mohammedreza stated no nitrogen was present. The total survey scans on the entire binding energy ranges of the Cu_2O films can be seen in Appendix B as Figures B.5, B.6 and B.7.

Figure 6.12 shows a detailed view of the binding energy range of nitrogen taken from the Cu_2O_1O2_33N2_750 film. There are no clearly visible peaks, only a large amount of noise. There might be a slight indication of two very noisy peaks at roughly 399 eV and 406 eV which could in an ideal world correspond to the N1s spectral line and a satellite. However, even if these were peaks and not just noise, the counts are so low that the doping level would be so low as to be negligible anyway. It is therefore highly unlikely that there is any nitrogen present in this film, at least in the nanometers of material closest to the surface.

Figure 6.13 shows a detailed view of the binding energy range of nitrogen, taken from the film called Cu2O_0O2_33N2_750. Similarly to the previous sample, there are no clearly visible peaks, only noise. Though there, once again, may be slight indications of noisy peaks at about 399 eV and 407 eV. However in this sample the noisy peaks are even less distinct than before, and as such any imagined or perceived nitrogen content

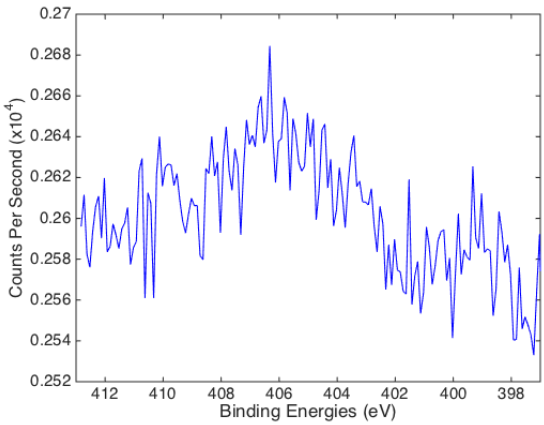

Figure 6.12: Detailed XPS in the N region of a Cu_2O film made at 750 °, with 1 sccm of O_2 and 33 sccm of N_2

could be written off as negligible. It is therefore highly unlikely that there is any nitrogen present in this film either, at least in the nanometers of material closest to the surface.

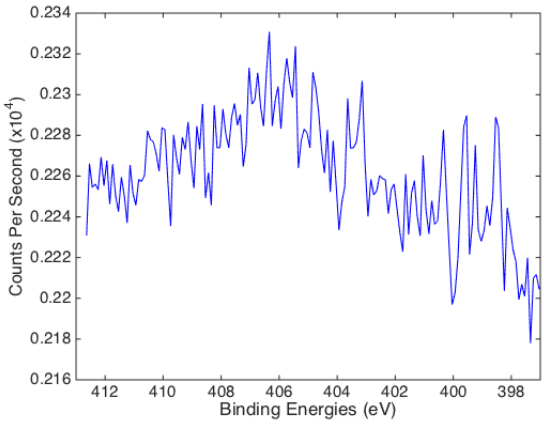

Figure 6.13: Detailed XPS in the N region of a Cu_2O film made at 750 °, with no O_2 and 33 sccm of N_2

As stated earlier, a similar scan was done for the Cr sputtered films deposited with 30 sccm of N_2 present during deposition. The data is not displayed here, as no close region scan in the nitrogen binding energy range was made, only a survey scan that has very little detail and was not pre sputter cleaned before the scan was made. However, Mohammedreza Nematollahi suggested that the survey scan indicated no more nitrogen

content than the two close scans.

6.3.5 Discussion of Cu_2O films

The three main goals for deposition of Cu_2O films was to produce a highly crystalline film with few defects, to produce a film with as low a resistivity as possible, and to produce a film doped with nitrogen to make an IB material.

The XRD shows clearly which films are the least viable, and which are more so . As can be seen in Figures 6.6 and 6.7, the 1O2_33N2_750 and 0O2_33N2_750 films as well as the two films made at 650 °C all clearly contain metallic copper, and as such would be completely useless for a high quality ZnO/Cu_2O junction. It appears that any films deposited under conditions with less than 2 sccm of O_2 in the temperature range used in this thesis will be unlikely to be good candidates for a ZnO/Cu_2O junction as they will only produce Schottky junctions.

The two films made under sputtering, with 2 sccm of oxygen, do not appear to contain any metallic copper, but the slight shift in the (111) and (200) peaks may indicate that there is some amount of CuO present in the thin films, though this is by no means conclusive. In fact, the phase stability graph of Rakhshani et al. [60] suggest that the films deposited with less oxygen pressure will be less likely to have CuO than those produced at higher oxygen pressures. If this is true then the peak shifting may be an instrument calibration issue rather than a material indication. This presence of CuO is neither verified nor confirmed, however, the phase stability of CuO may suggest than none of the films have any Cu_2O, and as such all films without Cu are viable candidates for the ZnO/Cu_2O junction.

As far as the XRD can determine, both the reference film, 3O2_00N2_750, and the film made with 3 sccm O_2 and 30 sccm of N_2, 3O2_30N2_750, appear to be made of only Cu_2O. This is supported by the (111) and (200) peak values being closer to the Cu_2O theoretical values that of the CuO theoretical values, as well as that the Cu_2O (111) peak is larger in these two films than in any of the others. The oxygen pressure during both depositions was P(O_2) = 1.3 x 10^{-3} Torr and for the film with nitrogen the total chamber pressure was P(chamber) = 3.6 x 10^{-3} Torr, both films were deposited at 750 °C.The deposition parameters for both of these films fall well inside what is suggested as ideal deposition parameters by Rakhshani et al. [60] in Fig. B.4 as well as Chen et al. [61] as outlined in Section 3.5.2. This would mean that these two films are both viable for a

ZnO/Cu_2O heterojunction

Additionally, the resistivity measurements demonstrate that the same two films, 3O2_00N2 and 3O2_30N2 are by far the least resistive. This is possibly a result of these films having a higher degree of crystallinity, as may be suggested by Fig. 6.10. This agrees with the results of Mittiga et al. [30] who suggests that higher degrees crystallinity generally gives lower resistivities since fewer grain boundaries that can will scatter mobile charge.

A decrease in resistivity was observed in two setts of films when nitrogen flow was increased, and no other parameters were changed. The films this effect was observed in were 3O2_30N2_750 which is more conductive than the 3O2_00N2_750 film and for the 1O2_25N2_650 film which is more conductive than the 1O2_05N2_650 film. Mittiga et al. [30] suggested that dopants such as nitrogen could have the effect of decreasing resistivity. Malerba et al. [26] observed this effect, and found that nitrogen doped films were indeed more conductive than their undoped counterparts. They found that a Cu_2O film doped with 2.5 at. % had a record breaking resistivity of 1.4 Ω cm, which is far more than the plain undoped Cu_2O thin films made by Mittiga et al. who have resistivities around 1000 Ω cm. As no other parameters have been changed between these two sets of Cu_2O films, it could very well be that some amount of nitrogen doping has been successful. However, this would need to be confirmed by EDS or XPS to be conclusive. Unfortunately, nether the 3O2_30N2_750 film or the 1O2_25N2_650 films were studied by XPS in this project.

Contrary to what the resistivity results may indicate, the XPS performed on the 1O2_33N2 and 0O2_33N2 films suggests the attempt at nitrogen doping may have failed. The two films studied by XPS both have higher nitrogen flow and lower oxygen flow than the two films that the resistivity measurements suggest may be doped, so if the XPS studied films are undoped it seems unlikely that the resistivity films are doped either. The failed attempt at doping may be because the form of nitrogen introduced into the chamber during deposition, N_2 is fairly unreactive, while the molecular oxygen also in the chamber is fairly reactive. All previous experiments that successfully produced nitrogen doped Cu_2O, that have been read during this project, have been produced by sputtering. [26] [84] It appears that the sputtering process lends itself more to doping at low N_2 flows.

In order to successfully dope the Cu_2O it may be attempted to introduce atomic nitrogen rather than the molecular form. Additionally, it may be interesting to do further tests with sputtering, varying parameters like power and further increasing the N_2 flow.

Finally, the TEM image confirms that the crystallinity of the 3O2_30N2_750 is at an acceptable scale in the plane parallel to the substrate. The 400 nm scale grains observed will be what forms contact with the ZnO and AZO layers. As the planar grains are even larger than the calculated normal crystallite sizes, this indicates that the defect density at the junction will be reasonably low and that the junction itself should work reasonably.

6.4 Solar Cells

An image of the fully assembled solar cell can be seen in Fig. 6.14. A four point probe was used to measure current-voltage characteristics between the electrodes noted in the image. The relationship was determined to be Ohmic in nature rather than characteristic of a diode, so XPS measurements were also made of the Mo electrode to test the material composition.

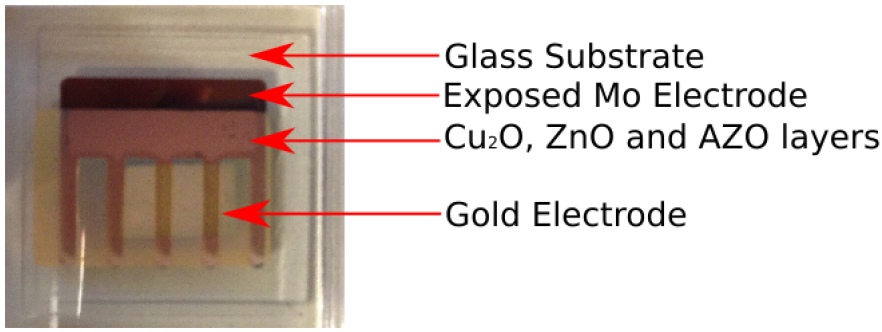

Figure 6.14: Image of the final assembled solar cell

6.4.1 I-V measurements

Do determine if the manufactured cells actually functioned as solar cells, I-V measurements were made on six of the seven solar cells that were produced. The composition of the six cells tested, all but Cell 2 which was damaged, are shown in Table 5.2. Using a four point probe and placing probes 1 and 2 on the exposed Mo electrode, and probes 3 and 4 on the gold electrode, gave the IV results shown in Fig. 6.15. The I-V behavior is clearly ohmic in nature rather than characteristic of a diode curve seen in Fig. 6.16.

The highly ohmic nature of the I-V curves suggest that the attempt at producing a solar cell has only produced a very complicated resistor. This happens when the series resistance, R_s, is extremely high causing it dominate all diode behavior to the point that only a common resistor remains. [7]

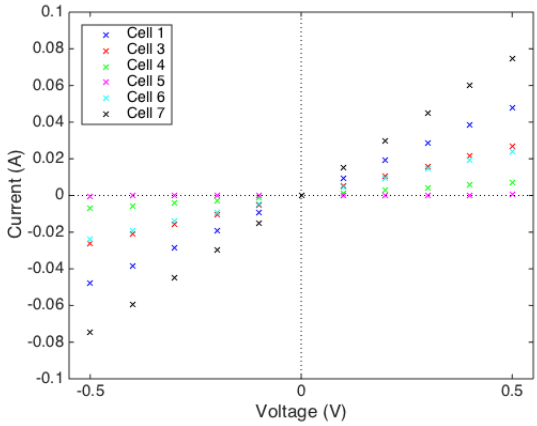

Figure 6.15: Four Point Probe I-V measurement comparison from non-illuminated cells 1,3,4,5,6,7 in Table 5.2. Cell 2 is not depicted as it broke, but it is assumed that it would behave similarly to the other 6 cells.

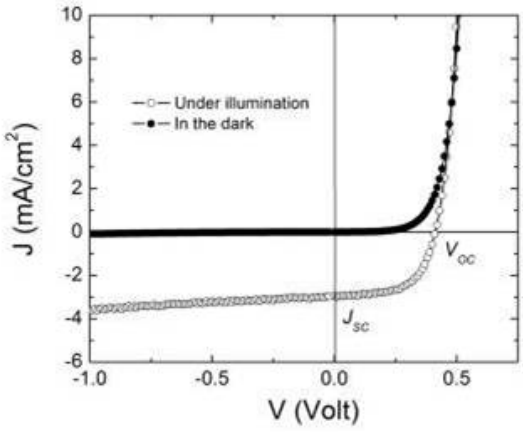

Figure 6.16: IV measurements of a functioning solar cell, taken from [85]

6.4.2 XPS

In an attempt to determine why the assembled solar cells do not function, an XPS measurement was made on the exposed part of the Mo electrode in a complete cell. The results are shown in Fig. 6.15. There are clear peaks in the oxygen, carbon and molybdenum binding energy ranges, these are summarized in Table 6.17.

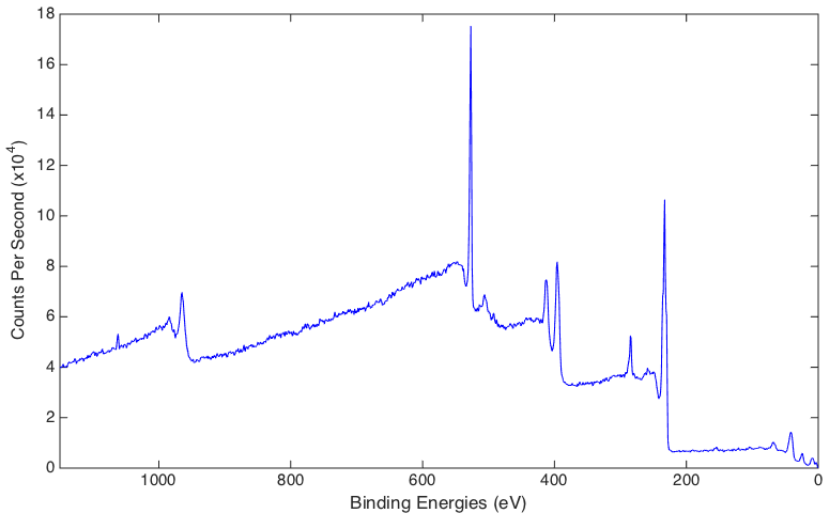

Figure 6.17: XPS Survey of the electrode on the completed device

Table 6.15: Survey XPS made on the Mo electrode of the solar cell.

Name	Position	FWHM	Area	At %
O 1s	526.89	2.982	5211.22	54.84
C 1s	284.89	2.973	9156.54	27.04
Mo 3d	232.89	5.729	73798.26	18.12

Another scan was made in the binding energy range of Mo, 226 eV - 240 eV. The results, seen in Fig. 6.18, shows thee peaks that represent the presence of various forms of molybdenum. The peaks have binding energy values of 236.3 eV, 232.9 eV and 229.6 eV. Consulting tables of XPS spectral line information from National Institute of Standards and technology, (NIST) suggests that these peaks all correspond to various oxides of Molybdenum and not the metallic form. The metallic Mo binding energy should be at around 227 eV where there is clearly no peak. A summary of XPS peaks corresponding

to 3d5/2 Mo oxidation states can be seeing Table 6.16, which has been sourced from an XPS reference page summarizing work from NIST [86]. The only peak unaccounted for in the Table is the one at 236.5 eV, which according to the same reference page is the split Mo_3 3d 3/2 binding energy.

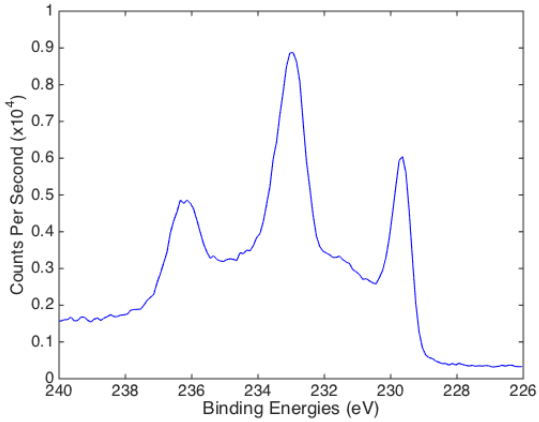

Figure 6.18: XPS data in the Bond Energy range of Molybdenum, taken from Fig. 6.17

Table 6.16: Average Mo 3d 5/2 binding energy values from a compilation of sources found at NIST. Table values were summarized by [86]

Compounds	3d 5/2 (eV)	St. Dev (eV)	no. of Ref.
Mo(0)	227.8	0.5	22
MoO_2	229.7	0.9	15
MoO_3	232.6	0.2	19

The results from the XPS clearly suggest that there is no metallic Mo, only oxidized variations of the material. Whilst both Mo and MoO_2 have very low resistivities on the order of 1 x 10^{-5} Ω cm, MoO_3 has a very high resistivity, which is on the order of 10^{12} Ω cm [87]. A combination of MoO_2 and MoO_3 could not work as an electrode as the MoO_3 content would destroy all electrode function with its high resistivity.

6.4.3 Discussion Solar Cell

The lack of characteristic I-V behavior in the completed solar cells indicate that something has gone wrong in the assembly. As literature shows, there have been many com-

pleted ZnO/Cu_2O junctions so it is likely that the problem lies somewhere within the design that took place in this thesis. The first potential error that needed investigating was that there was some short circuit between the Au and Mo electrodes, causing the shunt resistance to be so low that no diode behavior was possible. However, as newer cells were made with increasing care, the ohmic behavior continued, suggesting that there is some fundamental design flaw in the cell.

Next it was logical to look at the material composition of the Mo electrode, as careful study with a common light microscope shows some discoloration and yellowing of the electrode after the Cu_2O deposition took place. For this purpose XPS was used, and as the results in Fig. 6.18 shows, the Molybdenum present in the electrode has oxidized from its metallic form. Despite that the oxidation pressure necessary for MoO_x to form was not present during any of the deposition phases. It is likely that the high substrate temperature during Cu_2O deposition and the presence of the oxygen in the AZO layer on top of the Mo layer has caused the Mo to oxidize. This has made the series resistance in the cell so much higher than the shunt resistance, preventing diode behavior from taking place in any of the complete cells. It is also unfortunate that the work function of Mo is 4.6 eV

Similar designs have been proposed and created, Oku et al. [31] successfully made a glass-substrate/ITO/ZnO(Al)/Cu2O/Au heterojunction by spin coating and electrodeposition. Whilst deposition methods and parameters varied from those explored in this thesis, the focus on crystal structure of the Cu_2O and AZO layers were similar in intention. The cell design proposed by Oku et al. varied by two factors, the ITO rather than Mo electrode and the lack of an undoped ZnO layer. As the melting point of ITO is higher than 1500 °C using this material rather than Mo would have been a possible improvement and probably interesting path to further the research completed in this project.

Chapter 7

Conclusion

The focus of this thesis was to study the deposition parameters involved in the production of the ZnO/Cu_2O heterojunction with the intention of making an IBSC based on this heterojunction. First a literature study was conducted, looking at previous ZnO/Cu_2O junctions. Then an experimental study was conducted, focusing on improving the material quality of both the ZnO and Cu_2O layers. Additionally an attempt was made at producing an IB material with nitrogen doped Cu_2O, and to collect the parameters studied to produce a functioning solar cell.

The literature study focused on the record efficiency solar cells that have been made with ZnO/Cu_2O, on what challenges have been encountered with respect to this junction, as well as the possible solutions that have been considered to overcome these challenges. The highest efficiency ZnO/Cu_2O heterojunction that has been made so far was a 5.38 % efficiency cell made by Minami et al. [35] by depositing first a Ga_2O_3 buffer layer and then an AZO layer by PLD on thermally oxidized copper sheets. This is far from the conversion efficiencies of both Cu_2O and ZnO, which are 20 % and 18 % respectively. The most prominent challenges that have been identified are tied to the material quality of the Cu_2O layer, such as high resistivity and low crystallinity as a result of CuO contamination at the surface. The surface defects on the Cu_2O lead to unwanted charge transport and recombination at the junction interface. These challenges can be mitigated by growing single crystal Cu_2O both to decrease defects at the interface and to increase conductivity. Doping the material with p-type donors has also been attempted, and Mittiga et al. [30] found that Cl doping decreased the resistivity whilst Malerba et al. [26] reached a record low resistivity using N doping. Surface treatments of the Cu_2O have also been used, to remove CuO so to prevent Schottky junction formation and to decrease the interface defects that cause recombination.

In the experimental portion of this thesis AZO, ZnO and Cu_2O films were deposited on glass substrates by PLD. All films were studied individually by XRD to determine the dominant crystallites and their sizes, the resistivities of the AZO and Cu_2O films were measuredly four point probe, and two of the Cu_2O films were studied by XPS to determine if there was any nitrogen content and to attempt to determine the oxidation states of the copper in the films. One Cu_2O film was also studied by TEM imaging to obtain an idea of the planar grain sizes in the films produced in this thesis.

The AZO films studied in this project were considered on the basis of crystallite size and domination of the (002) orientation and resistivity. Films were made at 300 °C, 300 °C at substrate-target distances of 45 mm, 55 mm, and 65 mm. At 400 °C films were made that were 100 nm and 200 nm thick. It was concluded that the 100 nm thick film made at 400 °C at 55 mm substrate target distance was the best choice to include in the attempted solar cells because it combined the best crystal structure observed in this project with a resistivity which was not the low, but still acceptably low.

The Cu_2O films made in this thesis were deposited at varying oxygen flows and nitrogen flows, it was also attempted to change the deposition temperature and to induce doping by sputtering chromium. The viability of the films have to be considered on the basis of being pure Cu_2O, have as large a crystallite in the (111) orientation as possible, and they should have as low a resistivity as possible. The two films who had the lowest resistivity and the largest (111) oriented crystallite were the two films produced with 3 sccms of oxygen flow, a substrate temperature of 750 °C and no chromium sputtering. Neither of these films showed overt signs of containing CuO though it cannot be completely determined, and it is clear that neither film has any metallic copper. Of the two films, the film that was deposited with a flow of 30 sccms of N_2 was more conductive though it also had a slightly smaller (111) crystallite size. The best Cu_2O film produced for the purpose of a ZnO/Cu_2O junction in this project was therefore either the Cu_2O_3O2_00N2_750 film, with the largest (111) oriented crystallite and the second lowest resistivity or the Cu_2O_3O2_00N2_750 film with the lowest resistivity and the second largest (111) oriented crystallite.

It is unlikely that any IB materials have been sucessfully produced in this thesis. The resistivity measurements show that the films where nitrogen flow was increased are more conductive and therefore may have been doped. However, XPS measurements on films produced under an even higher nitrogen/oxygen flow rate ratio show almost no indication of any nitrogen in the XPS measurements, and the XPS peaks that may exist are so

noisy and small that they are negligible.

None of the attempts at producing a functioning solar cell in this project were successful. All cells, when tested, responded to a voltage across the electrodes with an ohmic current. The resistor-like nature of the current response indicates that the series resistance was too high, and as was experimentally tested this was probably a result of the molybdenum electrode oxidizing during Cu_2O deposition as a result of the high temperature and contact with the oxygenated ZnO layer and some oxygen in the chamber.

Further Work

One limiting factor to this project was that the scope was too extensive. It may have been interesting to focus only on producing good quality Cu_2O films as well as IB Cu_2O films. If this was done a more systematic approach to changing the flow parameters could be taken so that conclusions drawn from the XRD and resistivity measurements would be more clear. Additionally it would be interesting and useful to complete detailed XPS measurements on all Cu_2O films in the project to confirm the presence or lack thereof of nitrogen in all Cu_2O thin films.

Whilst the solar cells produced in this project did not work, it may be interesting to attempt to reproduce the cells with ITO electrodes rather than Mo. ITO is a highly conductive material that has been used with AZO previously by others like Oku et al. [31] to produce a functioning ZnO/Cu_2O junction. Using ITO rather than Mo, and then using the optimal parameters determined in this project would be interesting.

Appendix A

Acronyms

ALD Atomic Layer Deposition

AALD Atmospheric Atomic Layer Deposition

AZO Aluminium doped Zinc Oxide

CB Conduction Band

CBM Conduction Band Maximum

dc-MSP dc - Magnetron Sputtering

ECD Electrochemical Deposition

IB Intermediate Band

IBSC Intermediate Band Solar Cell

IBS Ion Beam Sputtering

ITO Indium doped tin oxide

NIST National Institute for Standards and Technology

PLD Pulsating Laser Deposition

PV Photovoltaic

SQ Shockley-Queisser

TEM Transmission Electron Microscopy

TCO Transparent Conductive Oxide

VAPE Vacum arch plasma evaporation

VB Valence Band

VBM Valence Band Maximum

XPS X-ray Photoelectron Spectroscopy

XRD X-Ray Diffraction

Appendix B

Additional Graphs

Additional AZO XRD graphs

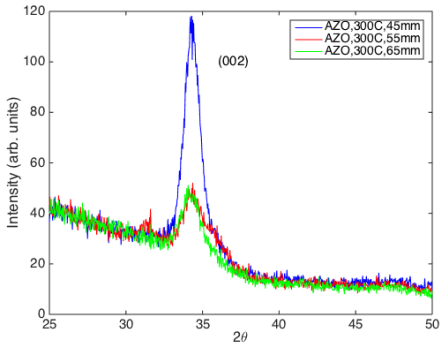

Figure B.1: XRD measurements of AZO films made with a substrate temperature of 300 °C with varying substrate-target distances. To reduce noise the 2θ range was set to 25 ° - 50 °

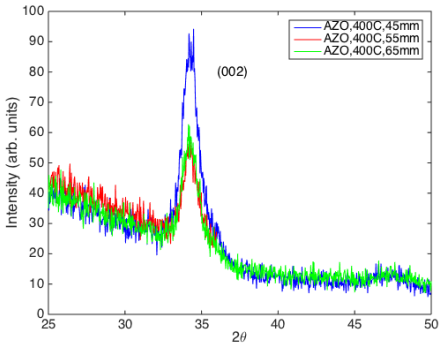

Figure B.2: XRD measurements of AZO films made with a substrate temperature of 400 °C with varying substrate-target distances. To reduce noise the 2θ range was set to 25 ° - 50 °

Copper phase graphs

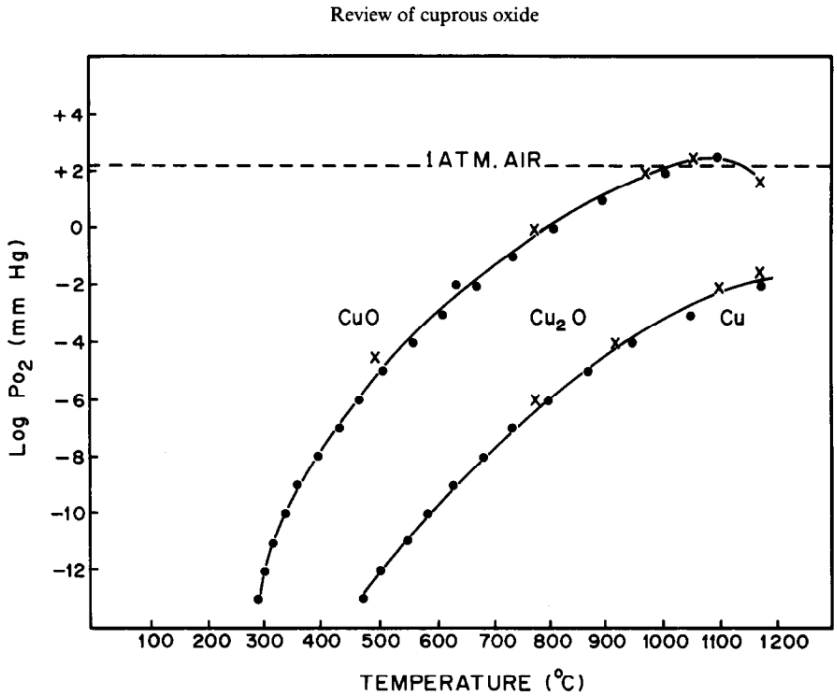

Figure B.3: A Pressure-Temperature phase stability diagram for the Cu-Cu_2O-CuO system as made by Rakhsani et al. [60]

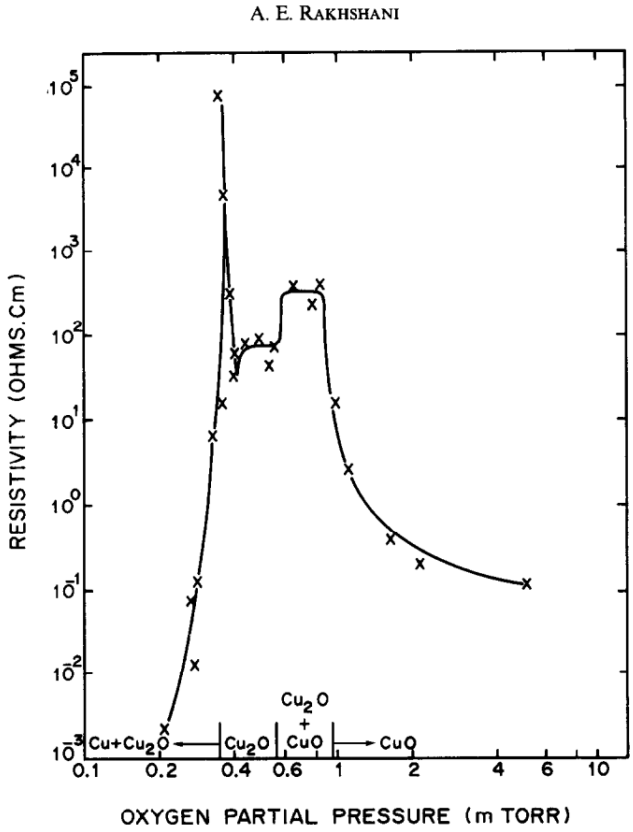

Figure B.4: Cu_2O resistivity as a function of oxygen partial pressure [60]

XPS survey Scans

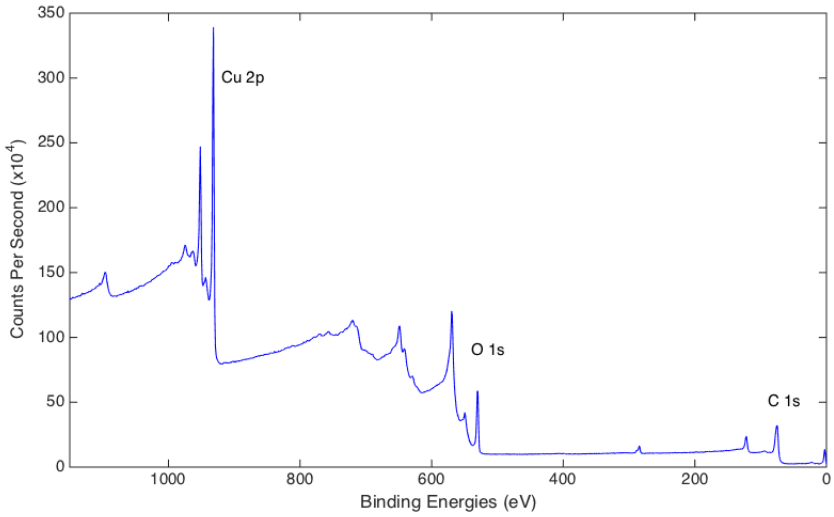

Figure B.5: XPS of a Cu_2O film made at a deposition temperature of 750 °, with 1 sccm of O_2 and 33 sccm of N_2

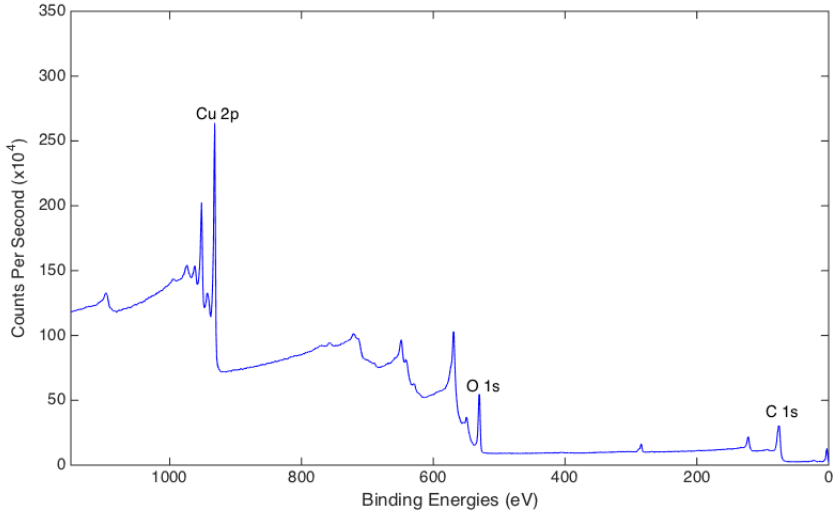

Figure B.6: XPS of a Cu_2O film made at a deposition temperature of 750 °, with no O_2 and 33 sccm of N_2

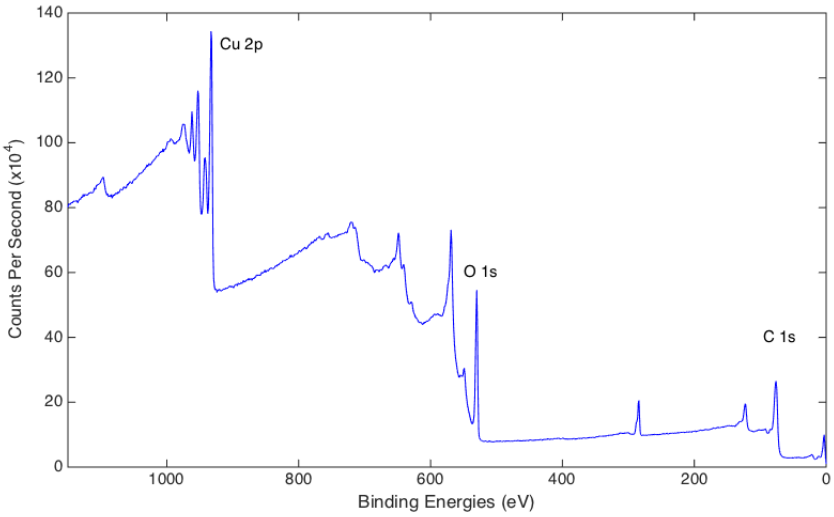

Figure B.7: XPS of a Cu_2O film made at a deposition temperature of 750 °, under Cr sputtering with 2 sccm O_2 and 30 sccm of N_2. This film was not sputter cleaned before scanning

Appendix C

Images

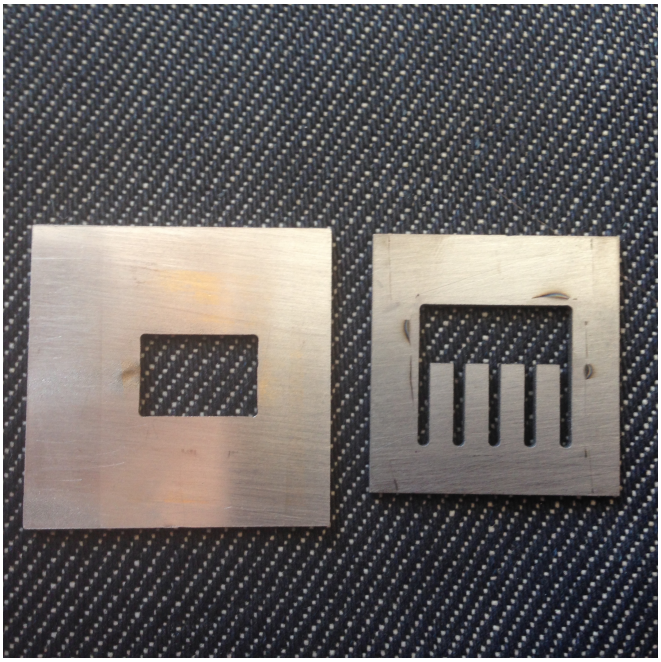

Figure C.1: The two steel masks produced for the purpose of masking the substrate during sputtering, so that electrodes would take the correct shape. The mask on the right was used for Mo deposition, and the one on the left was used for Au deposition.

Bibliography

[1] UN. World population to 2300. Technical report, United Nations Department of Economic and Social Affairs, 2004.

[2] Janet L. Sawin. Renewables 201: Global status report. Technical report, Renewable Energy Policy Network for the 21st Century (RED21), 2014.

[3] Solar generation 6: Solar photovoltaic electricity empowering the world. Technical report, European Photovoltaic Industry Association (EPIA), 2011.

[4] Cedric Philibert. Thechnology roadmap: Solar photovoltaic energy. Technical report, International Energy Agency, 2014.

[5] National Renewable Energy Laboratory. Research cell efficiency records, June 2015.

[6] Martin Green and Mary Archer, editors. *Clean Electricity from Photovoltaics*, volume 4 of *Series on Photoconversion of Solar Energy*. Imperial College Press, 57 Shelton Street, Covent Garden, London WC2H 9HE, England, 2 edition, 2015.

[7] Jenny Nelson. *The Physics of Solar Cells*. Imperial College Press, 2004.

[8] Loucas Tsakalakos, editor. *Nanotechnology for Photovoltaics*. CRC Press, Taylor and Francis Group, 6000 Broken Sound Parkway NW, Suite 300, 2010.

[9] Christiana Honsberg and Stuart Bowden. Open-circuit voltage.

[10] William Shockley and Hans J. Queisser. Detailed balance limit of efficiency of pn junction solar cells. *Journal of Applied Physics*, 32(3):510–519, 1961.

[11] Alexis De Vos. Detailed balance limit of the efficiency of tandem solar cells. *Journal of Physics D: Applied Physics*, 13(5):839, 1980.

[12] Y. Okada, N. J. Ekins-Daukes, T. Kita, R. Tamaki, M. Yoshida, A. Pusch, O. Hess, C. C. Phillips, D. J. Farrell, K. Yoshida, N. Ahsan, Y. Shoji, T. Sogabe, and J.-F. Guillemoles. Intermediate band solar cells: Recent progress and future directions. *Applied Physics Reviews*, 2(2), 2015.

[13] Antonio Luque and Antonio Marti. Increasing the efficiency of ideal solar cells by photon induced transitions at intermediate levels. *Phys. Rev. Lett.*, 78:5014–5017, Jun 1997.

[14] A. Marti, E. Antolin, C. R. Stanley, C. D. Farmer, N. Lopez, P. Diaz, E. Canovas, P. G. Linares, and A. Luque. Production of photocurrent due to intermediate-to-conduction-band transitions: A demonstration of a key operating principle of the intermediate-band solar cell. *Phys. Rev. Lett.*, 97:247701, Dec 2006.

[15] A Marti, N Lopez, E Antolin, E Canovas, C Stanley, C Farmer, L Cuadra, and A Luque. Novel semiconductor solar cell structures: The quantum dot intermediate band solar cell. *Thin Solid Films*, 511-512:Pages 638–644, July 2006.

[16] Antonio Luque, Antonio Marti, and Colin Stanley. Understanding intermediate-band solar cells. *Advances in Science and Technology*, 74:143–150, October 2010.

[17] Antonio Luque and Antonio Marti. Photovoltaics: Towards the intermediate band. *Nat Photon*, 5(3):137–138, 03 2011.

[18] E. Antolin, A. Marti, P.G. Linares, I. Ramiro, E. Hernández, C.D. Farmer, C.R. Stanley, and A. Luque. Advances in quantum dot intermediate band solar cells. In *Photovoltaic Specialists Conference (PVSC), 2010 35th IEEE*, pages 000065–000070, June 2010.

[19] W. Walukiewicz, W. Shan, K. M. Yu, J. W. Ager, E. E. Haller, I. Miotkowski, M. J. Seong, H. Alawadhi, and A. K. Ramdas. Interaction of localized electronic states with the conduction band: Band anticrossing in ii-vi semiconductor ternaries. *Phys. Rev. Lett.*, 85:1552–1555, Aug 2000.

[20] Weiming Wang, Albert S. Lin, and Jamie D. Phillips. Intermediate-band photovoltaic solar cell based on znte:o. *Applied Physics Letters*, 95(1):–, 2009.

[21] N. López, L. A. Reichertz, K. M. Yu, K. Campman, and W. Walukiewicz. Engineering the electronic band structure for multiband solar cells. *Phys. Rev. Lett.*, 106:028701, Jan 2011.

[22] Andrew S. Brown and Martin A. Green. Impurity photovoltaic effect: Fundamental energy conversion efficiency limits. *Journal of Applied Physics*, 92(3):1329–1336, 2002.

[23] Stephen P. Bremner, Michael Y. Levy, and Christiana B. Honsberg. Limiting efficiency of an intermediate band solar cell under a terrestrial spectrum. *Applied Physics Letters*, 92(17):–, 2008.

[24] Shogo Ishizuka, Shinya Kato, Takahiro Maruyama, and Katsuhiro Akimoto. Nitrogen doping into cu2o thin films deposited by reactive radio-frequency magnetron sputtering. *Japanese Journal of Applied Physics*, 40(4S):2765, 2001.

[25] David O. Scanlon and Graeme W. Watson. Undoped n-type cu2o: Fact or fiction? *The Journal of Physical Chemistry Letters*, 1(17):2582–2585, 09 2010.

[26] Claudia Malerba, Cristy Leonor Azanza Ricardo, Mirco D'Incau, Francesco Biccari, Paolo Scardi, and Alberto Mittiga. Nitrogen doped cu2o: A possible material for intermediate band solar cells? *Solar Energy Materials and Solar Cells*, 105(0):192 – 195, 2012.

[27] Bruno K. Meyer, Angelika Polity, Daniel Reppin, Martin Becker, Philipp Hering, Benedikt Kramm, Peter J. Klar, Thomas Sander, Christian Reindl, Christian Heiliger, Markus Heinemann, Christian Müller, and Carsten Ronning. Chapter six - the physics of copper oxide (cu2o). In Stephen J. Pearton Bengt G. Svensson and Chennupati Jagadish, editors, *Oxide Semiconductors*, volume 88 of *Semiconductors and Semimetals*, pages 201 – 226. Elsevier, 2013.

[28] Michael Nolan and Simon D. Elliott. The p-type conduction mechanism in cu2o: a first principles study. *Phys. Chem. Chem. Phys.*, 8:5350–5358, 2006.

[29] Yun Seog Lee, Mark T Winkler, Sin Cheng Siah, Riley Brandt, and Tonio Buonassisi. Hall mobility of cuprous oxide thin films deposited by reactive direct-current magnetron sputtering. *Applied Physics Letters*, 98(19):192115, 2011.

[30] Alberto Mittiga, Enrico Salza, Francesca Sarto, Mario Tucci, and Rajaraman Vasanthi. Heterojunction solar cell with 2substrate. *Applied Physics Letters*, 88(16):–, 2006.

[31] Takeo Oku, Tetsuya Yamada, Kazuya Fujimoto, and Tsuyoshi Akiyama. Microstructures and photovoltaic properties of zn(al)o/cu2o-based solar cells prepared by spin-coating and electrodeposition. *Coatings*, 4(2):203, 2014.

[32] Ka Eun Lee, Mingsong Wang, Eui Jung Kim, and Sung Hong Hahn. Structural, electrical and optical properties of sol–gel azo thin films. *Current Applied Physics*, 9(3):683–687, 5 2009.

[33] T. Minami, Y. Nishi, T. Miyata, and J. Nomoto. High-efficiency oxide solar cells with zno/cu2o heterojunction fabricated on thermally oxidized cu2o sheets. *Applied Physics Express*, 4, 2011.

[34] T. Minami, Y. Nishi, T. Miyata, and S. Abe. Photovoltaic properties in al-doped zno/non-doped $zn_{1-x}mg_xo$/cu_2o heterojunction solar cells. *ECS Trans.*, 50(51):59–68, 2012.

[35] Yuki Nishi Tadatsugu Minami and Toshihiro Miyata. High-efficiency cu_2o-based heterojunction solar cells fabricated using a ga_2o_3 thin film as n-type layer. *Applied Physics Express*, 6(4), April 2013.

[36] Y.S. Lee, D. Chua, R.E. Brandt, S.C. Siah, J.V. Li, J.P. Mailoa, S.W. Lee, R.G. Gordon, and T. Buonassisi. Atomic layer deposited gallium oxide buffer layer enables 1.2 v open-circuit voltage in cuprous oxide solar cells. *Advanced Materials*, 2014.

[37] Sajad Hussain, Chuanbao Cao, Ghulam Nabi, Waheed S. Khan, Zahid Usman, and Tariq Mahmood. Effect of electrodeposition and annealing of zno on optical and photovoltaic properties of the p-cu2o/n-zno solar cells. *Electrochimica Acta*, 56(24):8342 – 8346, 2011.

[38] J. Katayama, K. Ito, M. Matsuoka, and J. Tamaki. Performance of cu2o/zno solar cell prepared by two-step electrodeposition. *Journal of Applied Electrochemistry*, 34(7):687–692, 2004.

[39] Tadatsugu Minami, Toshihiro Miyata, Kazuhiko Ihara, Youhei Minamino, and Satoshi Tsukada. Effect of zno film deposition methods on the photovoltaic properties of zno–cu2o heterojunction devices. *Thin Solid Films*, 494(1–2):47 – 52, 2006. {ICMCTF} 2005 Proceedings of the 32nd International Conference on Metallurgical Coatings and Thin Films.

[40] K. Fujimoto, T. Oku, and T. Akiyama. Fabrication and characterization of zno/cu2o solar cells prepared by electrodeposition. *Applied Physics Express*, 6, 2013.

[41] Y. Ievskaya, R.L.Z. Hoye, A. Sadhanala, K.P. Musselman, and J.L. MacManus-Driscoll. Fabrication of zno/cu2o heterojunctions in atmospheric conditions: Improved interface quality and solar cell performance. *Solar Energy Materials and Solar Cells*, 135(0):43 – 48, 2015. {EMRS} 2014 Spring Meeting – Advanced materials and characterization techniques for solar cells {II}.

[42] Yuki Nishi, Toshihiro Miyata, and Tadatsugu Minami. The impact of heterojunction formation temperature on obtainable conversion efficiency in n-zno/p-cu_2o

solar cells. *Thin Solid Films*, 528(0):72 – 76, 2013. Proceedings of the 39th International Conference on Metallurgical Coatings and Thin Films (ICMCTF 2012) San Diego, California (USA) April 23-27, 2012 Proceedings of the 39th International Conference on Metallurgical Coatings and Thin Films (ICMCTF).

[43] S.W. Lee, Y.S. Lee, J. Heo, S.C. Siah, D. Chua, R.E. Brandt, S.B. Kim, J.P. Mailoa, T. Buonassisi, and R.G. Gordon. Improved cu2o-based solar cells using atomic layer deposition to control the cu oxidation state at the p–n junction. *Advanced Energy Mater*, 2014.

[44] Y.S. Lee, J. Heo, S.C. Siah, J.P. Mailoa, R.E. Brandt, S.B. Kim, R.G. Gordon, and T. Buonassisi. Ultrathin amorphous zinc-tin-oxide buffer layer for enhancing heterojunction interface quality in metal-oxide solar cells. *Energy and Environmental Science*, 6:2112, 2013.

[45] T. Minami, H. Tanaka, T. Shimakawa, and H. Sato T. Miyata. High-efficiency oxide heterojunction solar cells using cu2o sheets. *Japanese Journal of Applied Physics*, 43:L917 – L919, 2004.

[46] M. Izaki, T. Shinagawa, K.-T. Mizuno, Y. Ida, M. Inaba, and A. Tasaka. Electrochemically constructed p-cu2o/n-zno heterojunction diode for photovoltaic device. *Journal of Physics D: Applied Physics*, 40:3326 – 3329, 2007.

[47] A.T. Marin, D. Muñoz-Rojas, D.C. Iza, T. Gershon, K.P. Musselman, and J.L. MacManus-Driscoll. Novel atmospheric growth technique to improve both light absorption and charge collection in zno/cu2o thin film solar cells. *Advanced Functional Matter*, 23:3413–3419, 2013.

[48] K.P. Musselman, A. Wisnet, D.C. Iza, H.C. Hesse, C. Scheu, J.L. MacManus-Driscoll, and L. Schmidt-Mende. Strong efficiency improvements in ultra-low-cost inorganic nanowire solar cells. *Advanced Materials*, 22:E256–E258, 2010.

[49] S.S Jeong, A. Mittiga, A. Salza, A. Masci, and A. Passerini. Electrodeposited zno/cu2o heterojunction solar cells. *Electrochimica Acta*, 53:2226 – 2231, 2008.

[50] L.C. Olsen, F.W. Addis, and W. Miller. Experimental and theoretical studies of cu2o solar cells. *Solar Cells*, 7(3):247 – 279, 1982.

[51] Ben G. Streetman and Sanjay Kumar Banerjee. *Solid State Electronic Devices*. Pearson Prentice Hall, Upper Saddle River, New Jersey 07458, USA, sixth edition edition, 2006.

[52] Y. Abdu and A.O. Musa. Copper (i) oxide (cu_2o) based solar cells - a review. *Bayero Journal of Pure and Applied Sciences*, 2(2), July 2009.

[53] K. Akimoto, S. Ishizuka, M. Yanagita, Y. Nawa, Goutam K. Paul, and T. Sakurai. Thin film deposition of cu2o and application for solar cells. *Solar Energy*, 80(6):715 – 722, 2006. {SREN} '05 - Solar Renewable Energy News Conference.

[54] SeongHo Jeong, Sang Ho Song, Kushagra Nagaich, Stephen A. Campbell, and Eray S. Aydil. An analysis of temperature dependent current–voltage characteristics of cu2o–zno heterojunction solar cells. *Thin Solid Films*, 519(19):6613 – 6619, 2011.

[55] B.S. Li, K. Akimoto, and A. Shen. Growth of cu2o thin films with high hole mobility by introducing a low-temperature buffer layer. *Journal of Crystal Growth*, 311(4):1102 – 1105, 2009.

[56] Toshihiro Miyata, Tadatsugu Minami, Hideki Tanaka, and Horotoshi Sato. Effect of a buffer layer on the photovoltaic properties of azo/cu2o solar cells. volume 6037, pages 603712–603712–10, 2005.

[57] Kevin P. Musselman, Andrew Marin, Andreas Wisnet, Christina Scheu, Judith L. MacManus-Driscoll, and Lukas Schmidt-Mende. A novel buffering technique for aqueous processing of zinc oxide nanostructures and interfaces, and corresponding improvement of electrodeposited zno-cu2o photovoltaics. *Advanced Functional Materials*, 21(3):573–582, 2011.

[58] Yun Seog Lee. Defect engineering of cuprous oxide thin-films for photovoltaic applications. Master's thesis, Massachusetts Institure of Technology, 2013.

[59] Ke Cheng, Qianqian Li, Jian Meng, Xiao Han, Yangqing Wu, Shujie Wang, Lei Qian, and Zuliang Du. Interface engineering for efficient charge collection in cu2o/zno heterojunction solar cells with ordered zno cavity-like nanopatterns. *Solar Energy Materials and Solar Cells*, 116(0):120–125, 9 2013.

[60] A.E. Rakhshani. Preparation, characteristics and photovoltaic properties of cuprous oxide—a review. *Solid-State Electronics*, 29(1):7 – 17, 1986.

[61] Aiping Chen, Hua Long, Xiangcheng Li, Yuhua Li, Guang Yang, and Peixiang Lu. Controlled growth and characteristics of single-phase cu2o and cuo films by pulsed laser deposition. *Vacuum*, 83(6):927 – 930, 2009.

[62] F.K. Shan, B.C. Shin, S.W. Jang, and Y.S. Yu. Substrate effects of zno thin films prepared by {PLD} technique. *Journal of the European Ceramic Society*, 24(6):1015 – 1018, 2004. Electroceramics {VIII}.

[63] Hong-lie SHEN, Hui ZHANG, Lin-feng LU, Feng JIANG, and Chao YANG. Preparation and properties of azo thin films on different substrates. *Progress in Natural Science: Materials International*, 20(0):44–48, 11 2010.

[64] Shin-Ho Cho. Effects of growth temperature on the properties of zno thin films grown by radio-frequency magnetron sputtering. *Transactions on Electrical and Electronic Materials*, 10(6):185–188, 2009.

[65] Hui Kong, Pingxiong Yang, and Junhao. Chu. Processing parameters and property of azo thin film prepared by magnetron sputtering. *Journal of Physics: Conference Series*, 276, 2011. (Visited on 06/07/2015).

[66] Woon-Jo Jeong and Gye-Choon Park. Electrical and optical properties of zno thin film as a function of deposition parameters. *Solar Energy Materials and Solar Cells*, 65(1–4):37 – 45, 2001. {PVSEC} 11 Part I.

[67] Jeung Hun Park, Jong Moon Shin, S Cha, Jin Woo Park, S Jeong, Hyuk K Pak, and C Cho. Deposition-temperature effects on azo thin films prepared by rf magnetron sputtering and their physical properties. *JOURNAL-KOREAN PHYSICAL SOCIETY*, 49:S584, 2006.

[68] Hideki Tanaka, Kazuhiko Ihara, Toshihiro Miyata, Hirotoshi Sato, and Tadatsugu Minami. Low resistivity polycrystalline zno:al thin films prepared by pulsed laser deposition. *Journal of Vacuum Science & Technology A*, 22(4):1757–1762, 2004.

[69] B. K. Meyer, A. Polity, D. Reppin, M. Becker, P. Hering, P. J. Klar, Th. Sander, C. Reindl, J. Benz, M. Eickhoff, C. Heiliger, M. Heinemann, J. Blasing, A. Krost, S. Shokovets, C. Muller, and C. Ronning. Binary copper oxide semiconductors: From materials towards devices. *physica status solidi (b)*, 249(8):1487–1509, 2012.

[70] L. C. Olsen, R. C. Bohara, and M. W. Urie. Explanation for low efficiency cu2o schottky barrier solar cells. *Applied Physics Letters*, 34(1):47–49, 1979.

[71] Leonard J. Brillson and Yicheng Lu. Zno schottky barriers and ohmic contacts. *Journal of Applied Physics*, 109(12):–, 2011.

[72] Han-Ki Kim, Sang-Heon Han, Tae-Yeon Seong, and WK Choi. Electrical and structural properties of ti/au ohmic contacts to n-zno. *Journal of The Electrochemical Society*, 148(3):G114–G117, 2001.

[73] Toshihiro Kamohara, Morito Akiyama, and Noriyuki Kuwano. Influence of molybdenum bottom electrodes on crystal growth of aluminum nitride thin films. *Journal of Crystal Growth*, 310(2):345 – 350, 2008.

[74] Abd El-Hady B. Kashyout, Hesham M.A. Soliman, Hanaa Abou Gabal, Poussy Aly Ibrahim, and Marwa Fathy. Preparation and characterization of {DC} sputtered molybdenum thin films. *Alexandria Engineering Journal*, 50(1):57 – 63, 2011.

[75] Pushkar Ranade, Hideki Takeuchi, Tsu-Jae King, and Chenming Hu. Work function engineering of molybdenum gate electrodes by nitrogen implantation. *Electrochemical and Solid-State Letters*, 4(11):G85–G87, 2001.

[76] Hans-Ulrich Krebs, Martin Weisheit, Jorg Faupel, Erik Suske, Thorsten Scharf, Christian Fuhse, Michael Stormer, Kai Sturm, Michael Seibt, Harald Kijewski, Dorit Nelke, Elena Panchenko, and Michael Buback. Pulsed laser deposition (pld) – a versatile thin film technique. In Bernhard Kramer, editor, *Advances in Solid State Physics*, volume 43 of *Advances in Solid State Physics*, pages 505–518. Springer Berlin Heidelberg, 2003.

[77] Krishna Seshan, editor. *Handbook of Thin-Film Deposition Methods and Techniques: Principles, Methods, Equipment and Applications*. Noyes Publications, William Andrews Publishing, 13 Eaton Avenue 13 Eaton Avenue, Norwich, NY 13815, 2 edition, 2002.

[78] Jens Als-Nielsen and Des McMorrow. *Elements of Modern X-ray Physics*. WILEY, second edition edition, 2011.

[79] James Chan. *Four-Point Probe Manual*. EECS Microfabrication Technology, 2002.

[80] Brent Fultz and James M Howe. *Transmission Electron Microscopy and Diffractometry of Materials*. Springer, third edition edition, 2008.

[81] Rizwan Wahab, S. G. Ansari, Young-Soon Kim, Hyung-Kee Seo, and Hyung-Shik Shin. Room temperature synthesis of needle-shaped zno nanorods via sonochemical method. *Applied Surface Science*, 253(18):7622–7626, 7 2007.

[82] Ray Egerton. *Physical Principles of Electron Microscopy: An Introduction to TEM, SEM and AEM*. Springer, 2005.

[83] NIST. National institute of standards and technology xps database. http://srdata.nist.gov/xps/.

[84] Yoshitaka Nakano, Shu Saeki, and Takeshi Morikawa. Optical bandgap widening of p-type cu2o films by nitrogen doping. *Applied Physics Letters*, 94(2):–, 2009.

[85] Physics of solar cells, 2010.

[86] M.C. Biesinger. X-ray photoelectronic reference pages, 2015.

[87] M. A. Quevedo-Lopez, O. Mendoza-Gonzalez, R. F. Reidy, R. Ramirez-Bon, and R. A. Orozco-Teran. Effect of energetic treatments on the structure and resistivity of evaporated moo3 films on cadmium sulfide substrates. *Journal of Physics and Chemistry of Solids*, 61(5):727–734, 5 2000.